PRECAMBRIAN FELSIC AND MAFIC DIKES ALONG THE NORTHWESTERN MARGIN OF THE WYOMING PROVINCE: TECTONIC CONSTRAINTS FROM THE SOUTHERN HIGHLAND MOUNTAINS, MADISON COUNTY, MONTANA

A Thesis

by

BRANDON MCKEE GEDDIE

Submitted to the Office of Graduate and Professional Studies of
Texas A&M University
in partial fulfillment of the requirements for the degree of

MASTER OF SCIENCE

Chair of Committee,	Brent V. Miller
Committee Members,	Masako Tominaga
	William M. Lamb
Head of Department,	Michael C. Pope

May 2019

Major Subject: Geology

ABSTRACT

The Precambrian rocks of the southern Highland Mountains in Montana record the geologic history of the northwestern Wyoming craton. Multiple generations of mafic and felsic dikes cut the Archean gneissic fabric and are useful for constraining the Proterozoic tectonic evolution. This study provides mapping of the Nez Perce Hollow and Twin Bridges SW 7.5' quadrangles with a focus on dike characterization. Also presented here is U-Pb geochronology on two suites of granitic dikes and geochemical data on two suites of mafic dikes. Trace element data shows that amphibolite dikes in the mapping area intruded during a back-arc setting which is constrained in time between 2450 Ma and 1880 Ma. Analyses done here shows that no significant mobilization of elements occurred due to metamorphism, hydrothermal alteration, or chemical weathering and the geochemical signatures can be inferred to be the same for the protolith rock. Samples of diabase dikes have geochemistry similar to the Ramshorn Creek dikes recognized in the Tobacco Root Mountains nearby. This constrains this generation to the Moyie-Purcell large igneous province event ~1460 Ma.

Geochronology of the granitic dikes show there are two separate tectonic events separated by ~100 million years. The youngest granite has a best age of 1791±8.1 Ma which corresponds to the timing of the Big Sky Orogeny. The oldest granite has an age of ~1880 Ma which is interpreted to be a previously unrecognized event prior to the Big Sky Orogeny. This result suggests that a new model is needed for the amalgamation of the Wyoming Province and the Medicine Hat block.

DEDICATION

I would like to dedicate this thesis to my wife Kari and my parents for all their love and support throughout my education.

ACKNOWLEDGEMENTS

I would like to thank my committee chair, Dr. Brent Miller, for all his expertise and support throughout the past few years. He has been a wonderful mentor and friend for which I will never be able to thank enough. I would also like to thank my committee members, Dr. Will Lamb and Dr. Masako Tominaga, for their guidance throughout this thesis.

Thanks also to all of my friends and colleagues and the department faculty and staff for making this experience so great. I especially want to thank all of those who brought us meals after our car accident. The support from the department during the hardest time in our lives will never be forgotten.

Finally, thank you to Kari for working long hours to support us while I work on this degree. You make me want to be a better man.

CONTRIBUTORS AND FUNDING SOURCES

Contributors

This work was supervised by a thesis committee consisting of Professors Brent Miller and Will Lamb of the Department of Geology and Geophysics and Professor Masako Tominaga of the Department of Oceanography.

Mapping was completed with student's efforts from the 2011-2018 summer field camps as well as independent mapping trips by Noah Vento and the students of the 2018 Geol 450 class. Sample preparation and analysis were done with the assistance of Noah Vento, Jacob Tallon, Sophia Hibbeler, Allison Miller, Claire Stephenson, Colton Scott, Samantha Bowers, and Ryan Mutsune.

Funding Sources

Graduate study was supported by a scholarship from the Terry Foundation and a fellowship from BP Petroleum through the Department of Geology and Geophysics. This work was made possible by the United States Geological Survey under EDMAP grant # G17AS00005. Its contents are solely the responsibility of the authors and do not necessarily represent the official views of the USGS.

TABLE OF CONTENTS

Page

LIST OF FIGURES

Page

LIST OF TABLES

Page

1. INTRODUCTION

The Wyoming Province is a craton made up of Precambrian crust found throughout most of Wyoming and surrounding states (Fig. 1). It, along with at least seven other Archean cratonic blocks, make up the core of the North American continent (Whitmeyer and Karlstrom, 2007). Precambrian basement rocks of the Wyoming Province are sparsely exposed in the cores of Laramide uplifts (Mueller and Frost, 2006). One such uplift, which forms the focus of this study, is the Highland Mountains in SW Montana, located at the northwestern margin of the Wyoming province.

The cratonic core of North America was assembled through a series of Early Proterozoic collisional orogenies (Whitmeyer and Karlstrom, 2007). In the northern Wyoming province, the ca. 1780 to 1720 Ma Big Sky orogeny was the culminating cratonic collisional event (Harms et al., 2004). However, a paucity of structural, petrologic, geochemical and geochronologic studies on these rocks has prevented a detailed understanding of this major phase of continental accretion. The Highland Mountains are uniquely situated to further our understanding of this important tectonic era because these mountains are the northwestern-most major exposure of Precambrian basement (Fig. 1) and thus preserve a tectonic and thermal record from deep within the core of the Big Sky orogen.

The Highland Mountains contain multiply deformed and metamorphosed amphibolite and granulite-grade gneissic suites that were intruded and cross-cut by at

least two generations of felsic and mafic magmas, mostly in the form of dikes. The dikes are important structural and temporal marker units, without which it would be very difficult to distinguish Big Sky structural and metamorphic features from those resulting from earlier events. A detailed examination of field relations, geochemistry, and age data will allow for a more complete understanding of the tectonic events that led to the formation of the cratonic core of North America.

The main objective of this project is to define the temporal and tectonic relationship between mafic and felsic dikes and the metamorphic rocks they intrude. This will be conducted in three phases. First, it is necessary to produce a new, highly detailed map of the southern Highland Mountains to illustrate the field relations of felsic and mafic dikes more accurately than was available in previously published maps. Second, geochemical data will characterize and discriminate the mafic dikes in the Highland Mountains. Two distinct mafic units can be mapped in the field, an older slightly deformed amphibolite unit and a younger undeformed diabase unit. This study uses whole-rock and trace element geochemistry on the older mafic dikes to determine whether their geochemical characteristics are consistent with amphibolites from nearby mountain ranges (e.g. Brady et al., 2004b). This study seeks to define the geochemical characteristics of the diabase for the purpose of attempting to correlate them with the geochemical signatures of other dikes found throughout North American cratons (e.g. Brady et al., 2004b; Rogers et al., 2016). Third, as a result of the detailed mapping conducted here, two petrographically distinct generations of felsic dikes are now

recognized in the Highland Mountains. This study will define and distinguish these two sets of felsic dikes using petrography and U-Pb zircon geochronology.

2. GEOLOGIC BACKGROUND

2.1. The Wyoming Province

The Wyoming Province (Fig. 1), first named by Prucha et al. (1965), is exposed in basement-cored fault blocks uplifted during Laramide deformation. With an area of ~500,000 km^2, the province covers most of Wyoming, southwest Montana, and parts of Idaho, Utah, and the Dakotas (Mueller and Frost, 2006). The precise margins of the Wyoming Province are not well constrained, with the only well-exposed boundary located in the Medicine Bow Mountains and Sierra Madre Range in southeastern Wyoming. There, the Cheyenne Belt marks a suture of Archean rocks in the north and Proterozoic accreted island-arc terrain to the south (Duebendorfer and Houston, 1987; Karlstrom and Houston, 1984). To the west-southwest, the Farmington zone (Fig. 1) is interpreted as the Paleoproterozoic orogenic intersection of the Wyoming province and the Grouse Creek block (Mueller et al., 2011; Nelson et al., 2002). The northwestern margin of the Wyoming Province consists of the Selway terrane, a Paleoproterozoic arc-like terrane that is predominately covered by the Mesoproterozoic Belt supergroup (Foster et al., 2006). The Trans-Hudson orogeny represents the collision between the Wyoming province's eastern margin and the Superior craton (Whitmeyer and Karlstrom, 2007). The province's northern boundary is marked by the Great Falls Tectonic Zone (O'Neill and Lopez, 1985) where it was sutured to the Medicine Hat Block during the Big Sky Orogeny (Burger, 2004).

The Wyoming province is divided into three subprovinces, the Montana Metasedimentary province (MMP) in the northwest, the Beartooth-Bighorn magmatic

zone in the north-northeast, and the Southern accreted terranes to the south (Mueller and Frost, 2006). The oldest portion of the craton lies in the Montana Metasedimentary province and Beartooth-Bighorn magmatic zone. The oldest detrital zircon, Nd-Sm depleted mantle model ages and igneous crystallization ages ranging from 3300-3700 Ma (Mogk et al., 1992) and some cores of detrital zircons as old as 4000 Ma (Mueller et al., 1992). The Montana Metasedimentary province Precambrian rocks are metasupracrustal suites of pelitic schists, quartzites, and carbonate rocks intercalated with ca. 3300-3000 Ma quartzofeldspathic gneisses (Mogk et al., 1992; Mueller and Frost, 2006; Mueller et al., 1993; Mueller et al., 1996). Basement-cored uplifts there include the Highland, Tobacco Root, Greenhorn Mountains as well as the Ruby, Gravelly, and Madison ranges. The Beartooth-Bighorn magmatic zone is dominated by tonalite-trondhjemite-granodiorite metaplutonic rocks (Frost et al., 2006a; Mueller and Frost, 2006; Wooden and Mueller, 1988). The Beartooth Mountains, Bighorn Mountains, Wind River Range, Teton Range, and the Stillwater complex are major geologic features in this area. Recent studies of negative bulk rock initial ε_{Nd} with inherited zircons suggest this province might consist of older recycled Hadean crust (Frost et al., 2017). The youngest part of the Wyoming province is the Southern Accreted Terrains. Here, Neoarchean supracrustal sequences were accreted to the southern margin in pulses spanning ca. 2720-2630 Ma (Frost et al., 2006b).

2.2. Big Sky Orogeny

The Big Sky orogeny records a thermotectonic event that overprints Archean and Paleoproterozoic rocks in much of the northern Wyoming province (Harms et al., 2004). Prograde metamorphism through a clockwise PTt path reached peak pressures exceeded 1.0 GPa and temperatures >800 ^{o}C (Brady et al., 2004a; Cheney et al., 2004b; Harms et al., 2004). The core of the Big Sky orogen is the southern boundary of the Great Falls tectonic zone and the timing of peak metamorphism appears to become progressively younger to the southeast (Condit et al., 2015). High-grade tectonism is ca. 1810-1780 Ma in the Highland Mountains, ca. 1780-1750 Ma in the Ruby Range, Tobacco Root Mountains, and northwesternmost Northern Madison Range, and ca. 1750-1720 Ma in the central Northern Madison (Condit et al., 2015).

Although protolith ages in the Montana Metasedimentary province have been largely identified to be Archean, an Early Proterozoic age of metamorphism was first described by Giletti (1966), who found that K-Ar systems in rocks in the northwestern Wyoming province were reset ca. 1.6 Ga, and rocks to the southeast retained Archean K-Ar ages. The line that separates Archean and Proterozoic metamorphic domains is now referred to as “Giletti’s line” and is generally considered to mark the southeastern extent of rocks deformed and metamorphosed during the Big Sky orogeny (Erslev and Sutter, 1990; Harms et al., 2004; O’Neill and Berg, 1998).

The Big Sky orogeny marks the closure of an ocean basin north of the Wyoming province as it amalgamated with the Medicine Hat block and Hearne province (e.g. O'Neill and Lopez, 1985). Additionally, geophysical studies have suggested north-

dipping seismic refraction lines show a relict subducted slab below the Medicine Hat block which is projected to the surface along trend of the Big Sky orogeny (Gorman et al., 2002). The truncation of the Big Sky orogeny by the Trans-Hudson orogeny, and comparison of isotopic and paleomagnetic data in these zones, has led to complication in the models of tectonic buildup of Laurentia (e.g. Hrncir et al., 2017; Kilian et al., 2016). In one such model, Mueller et al. (2002) interpreted the possibility of the collision of the Hearne, Medicine Hat block, and the Wyoming province to be synchronous with the Trans-Hudson orogeny. Kilian et al. (2016) suggest that the Medicine Hat block and Wyoming province joined at the Great Falls tectonic zone while still separated from the Hearne and Superior cratons by a large ocean basin. Hrncir et al. (2017) argue that, while the interpretation of Medicine Hat and Wyoming coming together first is likely, their model does not agree with a large ocean basin separating them from the Superior and Hearn cratons. This dispute highlights the need for further investigation in the margins of the Wyoming province.

2.3. Paleoproterozoic Paleogeography

The timing of the Big Sky Orogeny and the amalgamation of the Wyoming Province with Laurentia is synchronous with the global buildup of the Paleo-Mesoproterozoic supercontinent Columbia (Zhao et al., 2002). The Northern margin of Laurentia began connecting with Siberia at 2000-1800 Ma (Zhao et al., 2002). At ~1800 Ma Australia and East Antarctica moved closer to the western margin of Laurentia as the ocean basin between them subducted under Australia (Gibson et al., 2018). Though an

ocean continued to separate Laurentia and the Australian cratons, accretion of smaller terranes impacted the southern margins of both between 1780 Ma and 1650 Ma (Betts et al., 2008). In the present-day northeast of Laurentia, Baltica and Greenland were amalgamated to Columbia through ~2100-1800 Ma orogenies (Zhao et al., 2002). Within a few hundred million years in the Paleoproterozoic, events similar to the Big Sky Orogeny brought together most of the world's land masses.

2.4. Highland Mountains

The Highland Mountains, located in Madison county Montana, are the northwestern-most exposure of Precambrian bedrock in the Montana Metasedimentary province segment of the Wyoming province. The Highland Mountains preserve a long and complex geologic history that extends to the Archean. The mountains lie at the intersection the thin-skinned folds and thrusts of the Montana thrust belt and the basement-cored uplifts of the Laramide foreland (Schmidt et al., 1988). Most of the ~400 km^2 is covered by Phanerozoic sediments, however, Cretaceous fault-bounded blocks have been uplifted to expose basement outcrops that provide an excellent laboratory for studying ancient crustal processes.

O'Neill et al. (1988) interpreted the Highland Mountains gneiss complex as a structural dome that exhumed Archean and Proterozoic rock along low-dip normal faults. A core of high-grade, migmatitic, metamorphosed quartzofeldspathic gneiss is structurally overlain by metamorphosed and migmatitic supracrustal rocks. Major faulting in the north and east of the Highland Mountains is younger than the gneiss dome

structure and brings the Precambrian rocks into juxtaposition with Mesoproterozoic and Phanerozoic rocks (O'Neill and Schmidt, 1989).

The core of the dome consists of quartzofeldspathic (granitic and tonalitic) leucocratic gneiss and a well-foliated quartz-feldspar-biotite±garnet±sillimanite gneiss cross cut by both granitoid dikes and metamorphosed mafic dikes (Miller and Geddie, 2018). The leucocratic gneiss is highly variable in composition but is most commonly massive with strongly lineated quartz and feldspar and contains little biotite in most areas. The gneiss commonly contains feldspar augen up to 3 centimeters in diameter and foliation is commonly folded and strongly lineated. Other localities are more biotite rich and are associated with leucogranite intruded in the gneiss which has well developed mylonitic texture. The quartz-feldspar-biotite±garnet±sillimanite gneiss is fine- to medium-grained with distinct platy foliation. This lithology grades into mylonite, which is cut by granitic dikes. The latter tends to weather easily while the former is more resistant and is often a cliff-former.

Biotite-rich, quartz-feldspar±garnet±sillimanite gneiss is the structurally highest Precambrian metamorphic rocks of the Highland Mountains (O'Neill et al., 1988). The western half of the field area is dominated by this metatexite migmatite that is lithologically highly variable but characterized by coarse-grained, biotite-rich gneiss (Miller and Geddie, 2018). Commonly highly foliated, this unit has numerous granitic melt segregations present at all scales from small disseminated patches, to vein networks, to meter-scale dikes. Centimeter-scale granitic dikes locally show progression

from brittle fracture and formation of polymineralic clasts to rotation of clasts into the gneissic foliation, to strongly foliated porphyroclastic mylonite textures.

Separating the biotite gneiss and the quartzofeldspathic gneisses at the core of the dome is a distinctive band of garnet-rich migmatitic biotite gneiss. Compositions of this rock can be 25%-60% garnet and also include amphibolite, quartzofeldspathic, and biotite-rich variations. Also present are small bands of garnet-sillimanite schist, marble, and calc-silicate. Accurate mapping of this unit plays a significant role in the interpretation of the Highland Mountains gneiss dome of O'Neill et al. (1988) because it structurally separates Archean gneisses with inferred largely igneous protoliths from metasedimentary gneisses.

2.5. Felsic Magmatism

Granitic aplite to pegmatite dikes are located in all the gneiss units, with high concentrations found within the biotite gneiss. Dikes have variable thickness from centimeters to a few meters and commonly cut across the country rock for tens of meters or more. A presumed earlier generation of medium-grained, internally deformed and recrystallized, biotite-rich, garnet-bearing granitoid dikes that cut across the gneissic fabric, are locally folded into the gneiss, pinch and swell, and show similar fabrics as the adjacent gneisses. Where less-deformed, these dikes form conduits that focus melt migration from surrounding migmatitic gneiss. Many silver and gold exploration pits are found within or near these dikes, but none were developed into full mining operations. In contrast, a presumed later generation of well preserved, course-grained,

graphic igneous texture, granitoid dikes that show no penetrative deformational fabrics and cut more sharply across the gneissic fabric of the country rocks. This generation, while sampled by numerous assay pits, has no associated mining activity. In the Tobacco Root Mountains, similar granitic dikes have been dated at 1772±8 Ma and attributed to a tectonothermal event affecting the Montana Metasedimentary province during that time (Mueller et al., 2004). This matches the timing and PTt model of the Big Sky orogeny of Harms et al. (2004).

2.6. Mafic Magmatism

Relatively rare mafic rocks form distinctive structural and metamorphic markers. Mapping has documented two associations of Proterozoic mafic dikes in the Highland Mountains (Figs. 2-3). The older generation of mafic dikes are medium- to coarse-grained, salt-and-pepper texture amphibolites that often contain garnet. Foliation and lineation are developed to varying degrees and the outcrops can occur as pods, lenses, or boudinaged bands transposed into the gneissic foliation (Fig.4). In areas that have been commercially quarried, the gneiss seems to fold around the dikes, though they cut the foliation at low angles. The center of the dikes tend to have coarser grains and the edges become finer at the margin, likely representing pre-metamorphic chilled margins as the dikes intruded into colder country rock.

Similar dikes are found in the nearby Tobacco Root Mountains, referred to as "metamorphic mafic dikes and sills (MMDS)", where they intrude both the Pony-Middle Mountain and Indian Creek Metamorphic Suites (Brady et al., 2004b). Recognizing the

importance of these units as tectonic markers, a number of researchers have sought to understand their geologic history. Mueller et al. (2004) found two zircon populations were contained in them, prismatic grains with an age of 2060±6 Ma, and smaller, rounded grains with an age of 1763±8 Ma. The older age was interpreted to be the age of intrusion and the younger related to the timing of metamorphism during the Big Sky orogeny. This matches $^{40}Ar/^{39}Ar$ isotopic ages of ca. 1800 Ma found in hornblende from dikes in the Highland Mountains which was interpreted to record a cooling from high-grade metamorphism throughout the area (Harlan et al., 1996).

Based on geochemical analysis, the MMDs of the Tobacco Root Mountains have subalkaline, tholeiitic basalt protoliths that possibly intruded during rifting that produced a passive continental margin on the western side of the Wyoming province (Brady et al., 2004b). Cheney et al. (2004b) suggested that MMDs in the Tobacco Root Mountains are correlative with the amphibolites in the Highland Mountains. Brady et al. (2004b) modeled fractional crystallization using TiO_2 as a normalizing component and found that orthopyroxene, clinopyroxene and plagioclase likely account for the majority of crystallization and fractional crystallization of olivine is likely minimal compared to the other three. If geochemical analysis in the Highland Mountain amphibolites has comparable results, it would provide further evidence for these units to be from a similar magma source and/or tectonic setting.

A younger east-west trending generation of mafic dikes is not deformed or metamorphosed and cuts all Precambrian rock units and fabrics (Figs. 2-3). Rogers et al. (2016) identified 17 geochemical signatures (GS) from Mesoproterozoic mafic dikes and

sills of the Belt-Purcell Basin and Wyoming province, 6 of which had sample locations within the southern Highland Mountains (GS 6, GS 7, GS 8, GS 9, GS 12, and GS 14) and showed similar lithology and trend to this younger generation. GS 6 was defined by whole-rock and REE chemistry of the Goat Flat dike of the Wind River Range of Wyoming (Chamberlain et al., 2000). It was correlated to the ca. 1460 Moyie-Purcell large igneous province magmatism and yielded a zircon U-Pb age of 1471±3 Ma (Chamberlain et al., 2000; Rogers et al., 2016). GS 7 and GS 8 were first recognized as group A and C in Wooden et al. (1978), who studied the dikes of the Tobacco Root mountains and split them using major oxides, Ni, and Zr versus Mg# or MgO. In that study, GS 7 had a Rb-Sr_{WR} age of 1455±125 Ma, and GS 8 was found to have a younger age of 1130±130 Ma from Rb-Sr_{WR}. GS 7 was later examined by Harlan et al. (2005) and showed a Sm-Nd_{WR} age of 1448±49 Ma. Rogers et al. (2016) interprets GS 7 and GS 8 as being geochemically distinct and not related to previously named events. GS 9 is localized to the Highland Mountains and the Beartooth Mountains of Wyoming (Rogers et al., 2016). Its geochemical signature is characterized by a much steeper heavy REE slope $(Gd\text{-}Yb)_{PM}$ and an anomalously large range of magnetic susceptibly compared to the other groupings (Rogers et al., 2016). GS 12 was attributed to the Moyie-Purcell large igneous province and was dated at 1469±2.5 Ma by Sears et al. (1998). The geochemical characteristics from the named sill used in that study is what defines the group (Rogers et al., 2016). The last geochemical grouping found in the Highland Mountains, GS 14, only includes two samples. They have a flat $(Gd/Yb)_{PM}$ slope and a slight enrichment in the REE slope $(La/Sm)_{PM}$ (Rogers et al., 2016).

3. METHODS

3.1. Field Mapping

Large-scale mapping was conducted during the summers of 2011-2018 as part of Texas A&M field camp. Under the USGS EDMAP grant # G17AS00005, mapping of the Nez Perce Hollow and Twin Bridges SW 7.5' quadrangles were conducted covering most of the Precambrian exposures in the area (Fig. 5). Detailed mapping occurred during both the 2017 and 2018 summers to finalize areas that had not been visited previously.

The location and character of the mafic and felsic dikes were a focus of mapping for this study. One goal was to map out each dike instead of presenting a schematic representation as in prior maps (e.g. McDonald et al., 2012; O'Neill et al., 1996). This method provided a way to examine location, concentration, and trend of each generation of dike at a higher resolution. Mapping individual felsic dikes enabled the removal of unit Xs (dense swarm of leucocratic quartz-feldspar sills intruded into crystalline metamorphic rocks) seen in O'Neill et al. (1996) and more clearly demonstrated the location and nature of the boundary between the two gneiss units. GPS tracks were used to map the edges of larger mafic and felsic dikes to show deformational trends.

Five-hundred-eighty-seven hand samples were collected of the mafic and felsic dikes, as well as the metamorphic rocks they intruded. Samples were cut into 27 x 46mm slabs on a table saw and sent to Spectrum Petrographics (www.petrography.com) for thin section mounting. These petrographic thin sections aided in defining igneous

and metamorphic units that were ambiguous in the field. Optical petrography and imaging were done using standard polarized-light optical microscopy.

3.2. Geochronology

Zircon grains were obtained from rock samples and analyzed by both isotope-dilution thermal ionization mass spectrometry (ID-TIMS) and laser-ablation inductively coupled plasma (LA-ICPMS) methods at the R. Ken Williams '45 Radiogenic Isotope Geosciences Laboratory at Texas A&M University. Samples for ID-TIMS analysis were annealed and abraded chemically following Mattinson (2005). Details of ID-TIMS methodology are given in Park et al. (2013) and the data are presented in Table 1. Zircon grains were analyzed for U-Pb isotopes and trace element concentrations by LA-ICPMS using a NWR/ESI 193nm ArF excimer laser-ablation system and a ThermoScientific iCAP RQ quadrupole mass spectrometer. Zircon 91500 (Wiedenbeck et al., 2004) was used as the primary standard for U-Pb down-hole and Pb isotope fractionation corrections and as a check on analytical reproducibility. Secondary zircon standards were Plešovice (Sláma et al., 2008) and FC-1 (Paces and Miller, 1993); both were analyzed and data reduced as unknowns as a check on age accuracy. Trace element concentrations were calculated relative to NIST612 using ^{29}Si as the internal standard. Data were reduced with Iolite v.3.6 (Paton et al., 2011; Paton et al., 2010) and data reduction scheme "U-Pb Geochron4" for U-Pb dates and "Trace Elements IS" for trace element concentrations.

3.3. Geochemistry

Thirty-three mafic dike samples were collected throughout the southern Highland Mountains mapping area from 2016-2018. Samples were collected from the center of the dikes in an attempt to avoid weathering and contamination. Each rock was reduced using a jaw-crusher and then pulverized using a Spex Certiprep shatterbox. A precontaminate aliquot of each sample was run prior to each sample being processed and the machines were scrubbed with ethyl alcohol after to reduce contamination. Geochemical analysis was conducted at Activation Laboratories (www.actlabs.com) for major- and trace-element concentrations using their "WRA+Trace – 4 Lithoresearch" package. Samples were prepared with a lithium metaborate/tetraborate fusion before being analyzed with inductively coupled plasma-optical emission spectroscopy (ICP-OES) and inductively coupled plasma-mass spectrometry (ICP-MS). The data was manipulated using the program GeoChemical Data toolkit (www.gcdkit.org). These new whole-rock data along with published data (Brady et al., 2004b; Rogers et al., 2016) will provide the framework necessary to define better geochemical discrimination and characterization diagrams.

4. RESULTS

4.1. Mapping

Detailed mapping of the felsic and mafic dikes in the field provided new insight into the relationship of the intrusions to each other and the host rocks. The oldest set of dikes intrude all of the gneissic units. Petrographically the major constituents are amphibole and plagioclase (>75%) with common garnet and minor quartz, opaque minerals, and clinopyroxene (Fig. 6). Reaction textures include clinopyroxene going to amphibole, amphibole pseudomorphs after garnet, or partly resorbed garnet with plagioclase retrograde rims.

Previously referred to as “mafic dikes and sills (Xm)”, these rocks are here renamed “amphibolite (Xam)” to better reflect their petrography. In addition, none can be demonstrated to have intruded parallel to sedimentary bedding and, therefore, the term “sills” is dropped and their presumed protoliths referred to only as “dikes”. Foliation of the gneisses are folded and deviate from regional orientations around these units within ten meters of their contact. Though previous mapping (e.g. McDonald et al., 2012; O'Neill et al., 1996) showed these dikes schematically as lines, mapping in this study provides accurate shape, size, and location to each outcrop (Figs. 2-3). More accurate mapping has demonstrated a spatial relationship between the quartzofeldspathic leucogneiss (Aql) and the trend of the amphibolites. To the south-southeast of the Aql boundary, the Xam forms moderately continuous bands that trend NE (Fig. 2). To the west of the Aql the Xam becomes more pod-like and generally trends N-S (Fig. 3). This

change in orientation follows the same pattern as the boundaries of the Aql and the quartzofeldspathic gneiss (Aqf), and is consistent with foliation and lithological contacts orientations controlled by an overall domal structure (O'Neill et al., 1988).

The younger mafic dikes (Yd) cut all metamorphic rocks in the mapping area. This suite of dikes is fine- to medium-grained diabase rocks. In thin section, the major constituents are plagioclase, clinopyroxene, and amphibole. Although through-going replacement of igneous minerals by metamorphic amphibole and epidote is common, clear relict ophitic texture is retained and relict pyroxene is preserved in the centers of amphibole and plagioclase (Fig. 7).

Unit Yd is less common than other mafic and metamafic rock types throughout the Highland Mountains. Often found as rubble on the ground, mapping of this unit proved to be more challenging than the other dikes. Many of the dikes were mapped from satellite images where they could be followed for up to seven kilometers. They intruded all other Precambrian units and cut across the boundaries of the gneissic units. The general trend is northwest-southeast, though a few are oriented east-west to southeast-northwest. Average width of these dikes is 1-3 m wide and continuous for tens to hundreds of meters. One anomalous example is 40 m wide and 7 km long in the northeastern section of the map area.

Two petrographically distinct granitoid dikes were mapped throughout the Highland Mountains. The more abundant Xgr1 dikes are fine- to medium-grained equigranular granite or monzogranite. This suite contains biotite (~10%) and in some locations a distinct deformational fabric. They range in size from a few mm to tens of

meters in width and appear to be melt generated from the Xbg metatexite. The rare Xgr2 dikes are leucocratic coarse-grained to pegmatitic granite with a graphic texture. These dikes show no deformation and cut through the gneissic foliation showing no obvious relationship to migmatitic melts in the biotite gneiss (Xbg). Both sets of felsic dikes are more abundant in the Xbg and the western margin of the Aqf. This is likely the reason that O'Neill et al. (1996) mapped parts of the boundary between the Aqf and Xbg as "undivided igneous and metamorphic rocks (Xs)". Mapping of the individual dikes in this location allows for the removal of Xs and more accurately reflects the distribution of the host gneissic units.

4.2. Geochronology

Two samples of Xgr were dated as part of this work. FC15-005 is a fine- to medium-grained granite and is petrographically part of the Xgr1 suite (Fig. 8). In thin section quartz commonly shows undulose extinction, suggesting some amount of deformation occurred after crystallization. Some of the larger K-feldspar grains show quartz exsolution textures and contain numerous muscovite inclusions (Fig. 8). FC15-005 is located south of the Cenozoic South Rochester Creek fault within the eastern boundary of the Xbg and its contact with the Xbg gneiss has been the focus of a small precious metal mining operation. FC13-014 is a medium- to coarse-grained granite that is part of the Xgr2 suite. Major constituents consist of quartz, K-feldspar, and plagioclase (Fig. 9). Quartz shows recrystallization textures and K-feldspar shows seritization with replacement mica and graphic texture.

A total of 150 U-Pb analyses were conducted on both monazite and zircons from sample FC15-005 and eighty zircon and monazite from sample FC13-014, including both thermal ionization mass spectrometry (TIMS) and laser ablation inductively coupled plasma mass spectrometry (LA-ICP-MS) analyses (Table 1). Nearly all analyses by both ID-TIMS and LA-ICPMS methods show the effects of at least one, and in many cases, multiple Pb-loss events. As a result, data points fall into a triangular array on Concordia diagrams (Figs. 10 and 11). Despite the extreme discordance of many data points, reliable age information can still be discerned. Figure 12 represents schematically the effects of multiple Pb-loss events on a rock with a combination of igneous and older xenocrystic zircons. Point A represents the Concordia position of the oldest xenocrystic zircon analyses without Pb-loss. One or more Paleoproterozoic metamorphic events would then pull concordant points variable amounts toward the Paleoproterozoic age and they would form an array between the two ages, as represented by point B. Another Pb-loss event in, for example the Cretaceous, would pull these already discordant down a line toward the Cretaceous age, as represented by point C. The result is an area containing all data with each of the apeces being geologically significant ages.

When plotted on a concordia diagram, monazite analyses from sample FC15-005 show a comparatively small degree of discordance (<10%) with an apparent single-stage Pb-loss array and have an upper-intercept regression age of 1766.5±5.9 Ma (Fig. 9). The ID-TIMS analysis of zircons were done with a step-leaching procedure similar to that of Mattinson (2005), but in this case, and each step solution was analyzed (Fig. 9). The initial leaching solution plotted away from the general trend of the final dissolution and

was not considered in the calculated age. The regression age of the ID-TIMS analyses is 1762.5±6.1 Ma. A significantly larger number of grains were analyzed by LA-ICP-MS. This allowed for discordant trends on concordia diagrams to be better represent. Data points form highly discordant arrays with lower intercept of approximately ~75 Ma – the known age of nearby Cretaceous plutonism (Tilling et al., 1968). The upper intercept regression age of these zircons is 1791.0±8.1 Ma. A number of spot analyses showed older discordant arrays, likely caused by xenocrystic zircon grains that experienced lead loss at ~1760-1780 Ma and again at ~75 Ma.

Monazite grains from sample FC13-014 show a linear trend with little discordance (<10%) and a reference line pinned at 75 Ma gives an upper intercept of 1777 Ma on a Concordia diagram (Fig. 11). Combined TIMS and LA-ICP-MS zircon analyses show a trend of varying discordance from 75 Ma to ~1880 Ma (Fig. 11). Spot analyses range from much older to slightly younger. These are interpreted to be xenocrystic, if older, or partially reset at both ~1760-1780 Ma and ~75 Ma. Initial crystallization of this suite of granites is interpreted to be ~1880 Ma. Concordant data points at ~1880 Ma in figure 11 likely represent new zircon crystallization and is represented as point D in figure 12. If these zircons experienced some degree of age resetting during the Big Sky Orogeny 100 m.y. later, their datum would fall on a tie line between ~1880 Ma and ~1780 Ma, shown by point E. Zircons that completely reset, new zircon growth, and monazite growth (representing the time of cooling) during the Big Sky Orogeny would plot at point F. Each of these scenarios (D, E, and F) would have been pulled on a tie line that intercepts the Cretaceous thermal event (represented

by D', E', and F' respectively). Because of this process, the data from FC13-014 that represents Paleoproterozoic zircons fall within a triangular zone between the Cretaceous and the two interpreted metamorphic events at ~1780 Ma and ~1880 Ma.

4.3. Geochemistry

Twenty-nine samples of amphibolite (Xam) and 4 samples of diabase (Yd) were analyzed for major- and trace-element geochemistry; no felsic dike samples were analyzed. The results of the geochemical analysis are reported in table 2 (appendix B). The present-day major-element chemistry of the metamorphic dikes can be altered from their protoliths due to hydrothermal alteration, weathering, and metamorphism. However, an MFW plot from Ohta and Arai (2007) indicates the degree of weathering seen in igneous rocks. The Xam were plotted in figure 13 and all samples plot near the mafic end-member of the ternary diagram where the unweathered basalt marker is. Therefore, major-element igneous geochemical discrimination diagrams can be used, with some caution, on these metamorphosed rocks as guides to the petrogenetic evolution, protoliths, and tectonic settings. Trace-elements are less susceptible to low-to-moderate grade alteration and metamorphism (Ross and Bédard, 2009) and are also used here to determine igneous characteristics. For example, light REE can be mobile during hydrothermal alteration or metamorphism (MacLean and Barrett, 1993), thus, it is essential to demonstrate immobility of the REE. To do this La, Ce, Nd, and Sm are plotted against a common immobile element like Zr (Fig. 14). The light REE from each geochemical group of Xam plot linearly against Zr and fit on a line through the standard

BCR-2. This suggests that all REE have been immobile through any hydrothermal alteration and metamorphism that affects these rocks.

The protoliths of the metamorphosed samples were sub-alkaline, tholeiitic basalts based on the alkali iron magnesium (AFM) diagram (Fig. 15). On a total alkali silica (TAS) diagram, samples plot within the sub-alkaline basalt field with SiO_2 ranging from 48-52 weight-percent (Fig. 16). Amphibolites (Xam) are plotted on a Zr vs. Y plot after Ross and Bédard (2009) and show that most samples are tholeiitic with some plotting in the transitional field (Fig. 17).

Four groups of mafic rocks are defined based on their geochemical characteristics. Following the discriminants used in Rogers et al. (2016), the MORB-OIB array of Pearce (2008) separates three clusters of Xam samples (Fig. 18). Two smaller groups plot above the E-MORB, and a larger group is shifted toward N-MORB. The larger group has been designated as group A, the group above the E-MORB with the highest Th/Yb ratio is group B, and the group just above the E-MORB is group C. The four analyzed Yd samples have been designated as group D for this study.

Rare earth element (REE) plots show that all samples, with the exception of one from group C, plot at ten times chondritic values (Fig. 19). Group A REE patterns are flatter than the other groups. Group B shows a steep slope in light REE and a flat slope for the heavies. Most samples in group B have a negative Eu anomaly. Group C REE patterns have little change in slope between the light and heavy elements. The REE slopes normalized to chondritic values are 0.97-1.72 for group A, 2.71-3.60 for group B, and 1.45-3.09 for group C.

Geochemical patterns of the Xam closely match those of back-arc basin basalts described in Pearce and Stern (2006) (Fig. 20). Using $Yb_N = 1$ (Fig. 20), the Nb/Yb ratio gives a proxy for mantle enrichment or depletion in this plot. Geochemical group A shows some depletion, particularly those with the lowest Nb. Groups B and C show enrichment of the mantle in all samples. This result parallel the use of figure 18 to discriminate groups due to the Nb/Yb ratio being one of the distinguishing factors.

The geochemistry of the Yd (group D) is defined by four samples. When plotted with Rogers et al. (2016) Highland Mountain samples on a MORB-OIB array, the Yd samples split into two of the groupings defined by Rogers et al. (2016) (Fig. 21). One sample that show more enrichment of REE on the spider plot than the other three. Only one sample in this group has a slight Eu anomaly.

5. DISCUSSION

5.1. Field Relationships

Dikes of the southern Highland Mountains provide important tectonic constraints on the Precambrian history of the Wyoming Province. Detailed mapping of exposed Precambrian rocks in the Highland Mountains provided a basis for understanding the field relationships of these units with the host gneisses. This area is located at the northwestern-most margin of the Wyoming Province and gives a natural laboratory to study tectonic during the Paleoproterozoic building of Laurentia. With a majority of studies focusing on the Tobacco Root Mountains and Ruby Range, the additional data presented here focusing on the Highlands Mountains pushes detailed tectonothermal understanding of this region farther north into the Great Falls tectonic zone.

I was able to refine map patterns and cross-cutting relationships of the two generations of mafic dikes and identify U-Pb dating targets for laboratory study. The Xam now show boudinage and folding within the gneissic foliation, commonly defining fold hinges in gneisses that did not show obvious folding patterns. The generally tabular nature of the amphibolites and the low-angle cutting of the gneissic foliation suggest their protolith intruded as dikes and not as basaltic flows. One particular question that arises from mapping this unit is its relationship with the Aql that makes up the core of the proposed gneiss dome of O'Neill et al. (1988). If the relationship between the gneisses are indeed a product of a gneiss dome, the trend of the Xam on the south-east and south-west of the Aql-Aqf boundary would suggest that the dikes were smeared into

the plane of the rising dome margins as seen in figures 2 and 3. However, the Xam continues its northeast-southwest trend through the Aqf and into the Aql as seen in figure 2. This would only be the case if the boundary between the two gneisses was in place during the time of dike intrusion. Because of this, the southeastern Aql-Aqf boundary was likely not a sheared zone during the time of dome formation. The western boundary, however, has dense granitic dikes that have been associated with a top-down-to-the-west shear zone and allowed for the development of the dome (Boyer, 2013). This could explain the change in trend of the Xam nearby (Fig. 3).

Detailed mapping of the felsic dikes allowed for the boundary between the Aqf and Xbg to be realized where previously mapped as Xs. Though, as previously mentioned, the areas of dense Xgr shows possible locations for shearing to accommodate the gneiss dome of O'Neill et al. (1988). The parallels of lithology between the Aql and the Xgr2 dikes led us to attempt to map the two granitic suites separately. I found this task too challenging to be accomplished within this study. Both suites of Xgr were found cutting all the gneissic units, though mostly occurring within the Xbg. Because of this, I cannot definitively say which unit each suite is derived from. Hopefully future geochemical studies of minerals within the dikes and gneisses will provide further insight into this question.

Another question sought in this study was if the younger diabase dikes showed any mappable trends between the six geochemical groupings of Rogers et al. (2016). I found no obvious correlation in the field or in petrographic associations. This could suggest that low-grade metamorphism or metasomatism play a role in the observed

geochemical signatures. One finding of interest is that many of the sample locations reported in Rogers et al. (2016) did not match up with what I found in the field. Many of the provided coordinates did not have mafic outcrops within 10-20 meters of them with some in particular being in the Cretaceous granite shown in figure 3.

5.2. Pre-Big Sky Orogeny Mafic Dikes

Geochemical analysis of amphibolites shows that three geochemical groupings are recognized in the Highland Mountains. There is one published date of 2060 Ma for similar metamorphic mafic dikes and sills of Tobacco Root Mountains (Mueller et al., 2004). Brady et al. (2004b) interpreted the intrusion of metamorphosed mafic dikes and sills to occur during a continental rift setting, similar to the East African Rift, based on the REE. Considering figure 14, there has likely been mobility of the light REE, possibly caused by the emplacement of the Tobacco Root batholith. Because of this, I cannot verify the relationship between the geochemistry of the Tobacco Root metamorphosed mafic dikes and sills and the Xam of the Highland Mountains.

The Th-Nb-Yb diagram in figure 18 was determined to be the best distinguisher of geochemical groupings. All three Xam groups plot above the MORB-OIB array which is consistent with selective enrichment of Th relative to Nb in a subduction component (Pearce, 2008). The Th-Nb proxy is effective in highlighting crustal input, particularly in the Precambrian where magma temperatures and crustal geotherms were likely higher and the crust had higher Th/Nb ratios (Pearce, 2008). Th is strongly mobilized by melts and weakly mobilized by high temperature fluids and Nb is

mobilized weakly by melting and not significantly by fluids. Because of this, it should be noted that amphibolite facies metamorphism and metasomatic fluids rich in Th could cause the fractionation seen in figure 18 (Pearce, 2008). Even with this consideration, all three groups likely underwent a similar degree of metamorphism and metasomatic processes, suggesting that the distinct groupings are not from a secondary process.

The geochemical pattern presented in figure 20 provides evidence that the Xam protolith intruded in a back-arc setting on the western edge of the Wyoming Province and not as an intra-plate extensional setting as suggested by Brady et al. (2004b). The Nb/Yb ratio is particularly important in tracing mantle flow in a number of back-arc regions around the world, assuming flow is accompanied by melt extraction or mixing (Pearce and Stern, 2006). The chemical gradient in trace elements could be the result of loss of melt fractions from the flowing mantle over time and the change seen between groups A, B and C could represent a temporal or spatial change throughout the basin.

5.3. Post-Big Sky Dikes

As shown in figure 21, the four samples of diabase dikes (Yd) analyzed in this study fall close to geochemical groups 6 and 7 of Rogers et al. (2016). The REE of group 6 are much lower than those of the Yd in this study. All of the Yd values are over 10 times chondritic values which matches group 7. This shows that if there are indeed multiple geochemical groupings, the Highland Mountains samples fit into the Ramshorn Creek group of Rogers et al. (2016). This group is related to the ca. 1460 Ma Moyie-Purcell large igneous province. This matches other continental tholeiitic dikes that

intruded the Belt-Purcell Supergroup (Rogers et al., 2016). These samples would differ from the dikes and sills that intruded into the wet unconsolidated sediments in the northern part of the Belt Basin and experienced more interaction with their host rocks. The Yd of the Highland Mountains intruded Archean crystalline basement and minimal crustal contamination occurred, as seen by the samples from this study plotting near the MORB-OIB array and having little Th enrichment.

Due to the lack of a robust sample size, this study cannot reliably test if there is indeed a field correlation to the multiple geochemical signatures reported in Rogers et al. (2016). As stated above, consideration should be given to where the reported sample locations are from that study. There are discrepancies in coordinates published and my mapping in the field. Future work should focus on resolving this as well as building a more robust collection of diabase samples for geochemical analyses.

5.4. Granitic Dike Analysis

Granitic dike emplacement in the Highland Mountains have previously been attributed to the Big Sky Orogeny (Mueller et al., 2004). Petrographic analyses of these dikes suggest that at least two suites of dikes were generated in the area. Geochronology work on Precambrian rocks prove challenging when thermal events during the Phanerozoic allow for lead diffusion of the grains and move the analyses away from concordance. LA-ICP-MS is a powerful tool to examine zircons in this situation because a large population of grains with varying levels of discordance can be examined and a regression can be made between the time of crystallization and the youngest lead

loss event. Discordant zircons of >2000 Ma exist in both suites and are interpreted to be xenocrystic from the parent rock that generated the melt. These zircons likely experience lead loss both at the Paleoproterozoic Big Sky Orogeny and the Cretaceous Laramide Orogeny.

The dominate array of zircons in FC15-005 have an upper intercept ~1760-1790 Ma. The lower intercept for all three regressed ages in this sample is ~75 Ma which I interpret as lead loss during the Cretaceous when large granitic bodies, like the Hells Canyon Pluton, were emplaced causing thermal flux throughout the area. Zircons have a much higher closure temperature than monazites, for this reason zircons are commonly interpreted as the initial crystallization of igneous bodies and monazites are interpreted as the cooling of igneous and metamorphic events. The youngest age for monazites is 1760.6 Ma (Fig. 9) which is older than the youngest age for TIMS zircons. The youngest age on the Monazites likely represents the youngest boundary of metamorphic and igneous zircon growth, therefore I interpret crystallization of the Xgr1 granites to occur between 1760.6 Ma and 1799.1 Ma (the oldest possible LA-ICP-MS zircon age). The age of 1791±8.1 Ma is likely the best representation of the crystallization age of these granites due to the robustness of the analyses incorporated into that regression.

The error ellipses on each data point from LA-ICP-MS zircon analyses for FC13-014 (Fig. 11) are larger than the red triangular area shown in figure 12 and the TIMS data has error ellipses that are smaller than the symbol that represents them. Because of this, a reference line was pinned at 75 Ma and drawn through the TIMS and concordant LA-ICP-MS data points. This resulted in the upper intercept of the reference line to be

at ~1880 Ma. I interpret this to signify a metamorphic event prior to the Big Sky Orogeny and after the 2450 Ma event described in Cheney et al. (2004a) and Mueller et al. (2004). This provides a record of a previously unidentified tectonic event that impacted the Highland Mountains.

Further evidence for the unidentified tectonic associate with Xgr2 is seen in figure 22. Two Xgr1 samples and one Xgr2 sample were analyzed prior to this study and their data was combined with the LA-ICP-MS data in this study and plotted on a relative probability diagram. Two distinct peaks are shown between the plots, one at the Big Sky and one at ~1880 Ma. The smaller peak at ~2000 Ma is interpreted to be the effect of xenocrystic zircons experiencing lead loss as shown in figure 11. This confirms the findings from this study that the two granitic dike suites are different and distinct and that two granite-generating tectonothermal events affected the Highland Mountains at ca. 1760 and ca. 1880 Ma.

5.5. Tectonic evolution

The results of this study provide new constraints on the tectonic evolution of the northern margin of the Wyoming Province. Both the felsic and mafic dikes cut the gneissic foliation which likely formed at 2450 Ma or earlier based on correlations with very similar gneissic units in the Tobacco Root Mountains (e.g. Harms et al., 2004). Metamorphic mineral ages (monazite and titanite) in both the felsic and mafic rocks were reset during the Big Sky Orogeny. Thus, the intrusion of both mafic and felsic dike

suites is constrained to between about 1760-2450 Ma. Figure 23 shows a timeline of the Paleoproterozoic tectonic events as recognized in the Highland Mountains.

In the Tobacco Root Mountains, the metamorphic mafic dikes (MMD) have yielded zircon U-Pb dates, inferred to be igneous crystallization ages, of ca. 2060 Ma (Mueller et al., 2004). The Highland Mountains Xam are similar in lithology and field relations, but cannot be definitively correlated geochemically to those in the Tobacco Root Mountains because of the mobility of the rare earth elements found there (Fig. 14). As a result, the age from the Tobacco Root Mountains MMD cannot be confidently applied to Xam in the Highlands. In rare strain shadows, Xam dikes clearly cut the foliation in the gneissic units (Fig. 4), and both suites of granite dikes cut Xam, Thus, both are constrained only between 1760-2450 Ma (Fig. 23).

The zircon U-Pb age of the Xgr2 suite suggest a collisional event occurred ~1880 Ma; 100 million years prior to the Big Sky Orogeny. Vervoort et al. (2016) found zircon ages of 1860 Ma in orthogneisses located in the Clearwater and Priest River complexes in northern Idaho and interpreted those ages as collision with an arc along the western margin of the Wyoming Province distinctly separate from Big Sky events. The ca. 1880 Ma granite dikes in the Highland Mountains may result from a similar collisional event along the northern margin of the Wyoming Province. This would suggest that either the Medicine Hat block amalgamated with the Wyoming Province in multiple pulses starting 100 million years prior to the Big Sky Orogeny or an unrecognized crustal block docked to the northern edge of the craton and the Medicine Hat block collided later. The later interpretation is represented by two collisional events in figure 23.

Zircon U-Pb analyses of the Xgr1 suite demonstrate that these granites were produced during the Big Sky Orogeny. This coincides with the interpreted age of leucocratic dikes in the Tobacco Root Mountains (Mueller et al., 2004). Evidence present here from the Highland Mountains similarly suggests that the Big Sky Orogeny along the northern margin of the Wyoming Province resulted in the closure of a north-facing ocean basin during collision of the Medicine Hat Block. Because the Big Sky Orogeny followed the ca. 1880 Ma event by about 100 m.y., I interpret the Big Sky Orogeny as a completely distinct thermotectonic event that has largely overprinted the older, probably arc-continent, collisional event.

6. CONCLUSIONS

Detailed mapping, geochemistry, and geochronology of mafic and felsic dikes in the southern Highland Mountains of Montana have provided new constraints on the tectonic history of the Wyoming Province. This study provides a detailed examination of tectonothermal events leading up to the Paleoproterozoic Big Sky Orogeny.

Mapping of the Precambrian rocks in the Highland Mountains provided increased understanding in the relationship between at least three generations of dikes and the gneisses they intrude, and provides for clearer identification of unit boundaries that were previously unmapped or represented schematically. The field relations of the amphibolite dikes are now better represented and their spatial relationship with the core of the proposed Highland Mountains gneiss dome has been mapped. A clear change in the trend of these dikes is seen on the western side of the Aql-Aqf boundary. Future work should focus on mapping the trend of their foliation to better represent the impact of the Big Sky Orogeny as well as the rise of the dome itself.

The field relationship between two suites of granitic dikes is still only vaguely understood and need to be mapped in more detail. With the petrographic foundation presented here, future work might be able to map these units separately to provide answers about location and melting source as well as additional relative timing constraints.

Geochemical analyses of amphibolite dikes within the map area show there are three chemical associations in the Highland Mountains. The trace element geochemistry cannot confidently correlate these samples to similar MMD found in the Tobacco Root

Mountains. In contrast to the geochemical interpretation of the MMD in the Tobacco Root Mountains, the amphibolites in the Highland Mountains show chemical characteristics consistent with formation in a back-arc setting. The largest chemical group resembles NMORB composition while the two smaller groups are more closely related to EMORB. All samples show component of crustal contamination in their chemistry. The amphibolites are temporally pinned between the 2450 Ma gneissic foliation they cut and the 1880 Ma granite dikes that cut them.

Geochronology done in this study shows that the two granitic dikes suites also have crystallization ages that are separated by ~100 Ma. The Xgr2 granites have an age of ~1880 Ma which is interpreted to be from a collisional tectonic previously unrecognized in the northern Wyoming Province. This suggests that a new or refined tectonic model is needed for how the Wyoming Province and the Medicine Hat block amalgamated.

REFERENCES

Betts, P., Giles, D., and Schaefer, B., 2008, Comparing 1800–1600 Ma accretionary and basin processes in Australia and Laurentia: Possible geographic connections in Columbia: Precambrian Research, v. 166, no. 1-4, p. 81-92.

Boyer, L. M., 2013, Insights into the Timing, Origin, and Deformation of the Highland Mountains Gneiss Dome in Southwestern Montana, USA: Theses and Dissertations. 827.

Brady, J. B., Kovaric, D. N., Cheney, J. T., Jacob, L. J., and King, J. T., 2004a, 40Ar/39Ar ages of metamorphic rocks from the Tobacco Root Mountains region, Montana, *in* Brady, J. B., Burger, H. R., Cheney, J. T., and Harms, T. A., eds., Precambrian Geology of the Tobacco Root Mountains, Montana, Geological Society of America.

Brady, J. B., Mohlman, H. K., Harris, C., Carmichael, S. K., Jacob, L. J., Chaparro, W. R., Burger, H., Cheney, J., and Harms, T., 2004b, General geology and geochemistry of metamorphosed Proterozoic mafic dikes and sills, Tobacco Root Mountains, Montana: SPECIAL PAPERS-GEOLOGICAL SOCIETY OF AMERICA, p. 89-104.

Burger, H. R., 2004, General geology and tectonic setting of the Tobacco Root Mountains: Geological Society of America Special Papers, v. 377, p. 1-14.

Chamberlain, K., Sears, J., Frost, B., and Doughty, P., Ages of Belt Supergroup deposition and intrusion of mafic dikes in the central Wyoming Province: Evidence for extension at ca. 1.5 Ga and 1.37 Ga and potential piercing points for Rodinia reconstructions, *in* Proceedings Geological Society of America, Abstracts with Programs2000, Volume 32, p. A-319.

Cheney, J. T., Alexander, A., Webb, G., Coath, C., McKeegan, K., Brady, J., Burger, H., and Harms, T., 2004a, In situ ion microprobe^ 2^ 0^ 7Pb/^ 2^ 0^ 6Pb dating of monazite from Precambrian metamorphic suites, Tobacco Root Mountains, Montana: SPECIAL PAPERS-GEOLOGICAL SOCIETY OF AMERICA, p. 151-180.

Cheney, J. T., Brady, J. B., Tierney, K. A., DeGraff, K. A., Mohlman, H. K., Frisch, J. D., Hatch, C. E., Steiner, M. L., Carmichael, S. K., and Fisher, R. G., 2004b, Proterozoic metamorphism of the Tobacco Root Mountains, Montana: SPECIAL PAPERS-GEOLOGICAL SOCIETY OF AMERICA, p. 105-130.

Condit, C. B., Mahan, K. H., Ault, A. K., and Flowers, R. M., 2015, Foreland-directed propagation of high-grade tectonism in the deep roots of a Paleoproterozoic collisional orogen, SW Montana, USA: Lithosphere.

Cox, K. G., Bell, J., and Pankhurst, R., 1979, The interpretation of igneous rocks, 004552016X.

Duebendorfer, E., and Houston, R., 1987, Proterozoic accretionary tectonics at the southern margin of the Archean Wyoming craton: Geological Society of America Bulletin, v. 98, no. 5, p. 554-568.

Erslev, E. A., and Sutter, J. F., 1990, Evidence for Proterozoic mylonitization in the northwestern Wyoming province: Geological Society of America Bulletin, v. 102, no. 12, p. 1681-1694.

Foster, D. A., Grice Jr, W. C., and Kalakay, T. J., 2010, Extension of the Anaconda metamorphic core complex: 40Ar/39Ar thermochronology and implications for Eocene tectonics of the northern Rocky Mountains and the Boulder batholith: Lithosphere, v. 2, no. 4, p. 232-246.

Foster, D. A., Mueller, P. A., Mogk, D. W., Wooden, J. L., and Vogl, J. J., 2006, Proterozoic evolution of the western margin of the Wyoming craton: Implications for the tectonic and magmatic evolution of the northern Rocky Mountains: Canadian Journal of Earth Sciences, v. 43, no. 10, p. 1601-1619.

Frost, C. D., Frost, B. R., Kirkwood, R., and Chamberlain, K. R., 2006a, The tonalite–trondhjemite–granodiorite (TTG) to granodiorite–granite (GG) transition in the late Archean plutonic rocks of the central Wyoming Province: Canadian Journal of Earth Sciences, v. 43, no. 10, p. 1419-1444.

Frost, C. D., Fruchey, B. L., Chamberlain, K. R., and Frost, B. R., 2006b, Archean crustal growth by lateral accretion of juvenile supracrustal belts in the south-central Wyoming Province: Canadian Journal of Earth Sciences, v. 43, no. 10, p. 1533-1555.

Frost, C. D., McLaughlin, J. F., Frost, B. R., Fanning, C. M., Swapp, S. M., Kruckenberg, S. C., and Gonzalez, J., 2017, Hadean origins of Paleoarchean continental crust in the central Wyoming Province: GSA Bulletin, v. 129, no. 3-4, p. 259-280.

Gibson, G., Champion, D., Withnall, I., Neumann, N., and Hutton, L., 2018, Assembly and breakup of the Nuna supercontinent: Geodynamic constraints from 1800 to 1600 Ma sedimentary basins and basaltic magmatism in northern Australia: Precambrian Research, v. 313, p. 148-169.

Giletti, B. J., 1966, Isotopic ages from southwestern Montana: Journal of Geophysical Research, v. 71, no. 16, p. 4029-4036.

Gorman, A. R., Clowes, R. M., Ellis, R. M., Henstock, T. J., Levander, A., Spence, G. D., Keller, G. R., Miller, K. C., Snelson, C. M., and Burianyk, M. J., 2002, Deep Probe: imaging the roots of western North America: Canadian Journal of Earth Sciences, v. 39, no. 3, p. 375-398.

Harlan, S. S., Geissman, J. W., Snee, L. W., and Reynolds, R. L., 1996, Late Cretaceous remagnetization of Proterozoic mafic dikes, southern Highland Mountains, southwestern Montana: A paleomagnetic and 40Ar/39Ar study: Geological Society of America Bulletin, v. 108, no. 6, p. 653-668.

Harlan, S. S., Premo, W. R., Unruh, D., and Geissman, J. W., 2005, Isotopic dating of Meso-and Neoproterozoic mafic magmatism in the southern Tobacco Root Mountains, southwestern Montana: Precambrian Research, v. 136, no. 3-4, p. 269-281.

Harms, T. A., Brady, J. B., Burger, H. R., and Cheney, J. T., 2004, Advances in the geology of the Tobacco Root Mountains, Montana, and their implications for the history of the northern Wyoming province, *in* Brady, J. B., Burger, H. R., Cheney, J. T., and Harms, T. A., eds., Precambrian Geology of the Tobacco Root Mountains, Montana, Geological Society of America.

Hrncir, J., Karlstrom, K., and Dahl, P., 2017, Wyoming on the run—Toward final Paleoproterozoic assembly of Laurentia: COMMENT: Geology, v. 45, no. 4, p. e411-e411.

Irvine, T., and Baragar, W., 1971, A guide to the chemical classification of the common volcanic rocks: Canadian journal of earth sciences, v. 8, no. 5, p. 523-548.

Karlstrom, K. E., and Houston, R. S., 1984, The cheyenne belt: analysis of a proterozoic suture in Southern Wyoming: Precambrian Research, v. 25, no. 4, p. 415-446.

Kilian, T. M., Chamberlain, K. R., Evans, D. A. D., Bleeker, W., and Cousens, B. L., 2016, Wyoming on the run—Toward final Paleoproterozoic assembly of Laurentia: Geology.

MacLean, W., and Barrett, T., 1993, Lithogeochemical techniques using immobile elements: Journal of geochemical exploration, v. 48, no. 2, p. 109-133.

Mattinson, J. M., 2005, Zircon U–Pb chemical abrasion ("CA-TIMS") method: Combined annealing and multi-step partial dissolution analysis for improved precision and accuracy of zircon ages: Chemical Geology, v. 220, no. 1–2, p. 47-66.

McDonald, C., Elliott, C. G., Vuke, S. M., Lonn, J. D., and Berg, R. B., 2012, Geologic Map of the Butte South 30'X 60'Quadrangle, Southwestern, Montana, Montana Bureau of Mines and Geology.

McDonough, W. F., and Sun, S. s., 1995, The composition of the Earth: Chemical Geology, v. 120, no. 3, p. 223-253.

Miller, B. V., and Geddie, B. M., 2018, Precambrian bedrock map of the southern Highland Mountains, Madison County Montana: Twin Bridges SW and Nez Perce Hollow quadrangles: scale 1:14,500, personal communication.

Mogk, D. W., Mueller, P. A., and Wooden, J. L., 1992, The nature of Archean terrane boundaries: an example from the northern Wyoming Province: Precambrian Research, v. 55, no. 1-4, p. 155-168.

Mueller, P., Wooden, J., and Nutman, A., 1992, 3.96 Ga zircons from an Archean quartzite, Beartooth Mountains, Montana: Geology, v. 20, no. 4, p. 327-330.

Mueller, P. A., Burger, H. R., Wooden, J. L., Heatherington, A. L., Mogk, D. W., D Arcy, K., Brady, J., Cheney, J., and Harms, T., 2004, Age and evolution of the Precambrian crust of the Tobacco Root Mountains, Montana: SPECIAL PAPERS-GEOLOGICAL SOCIETY OF AMERICA, p. 181-202.

Mueller, P. A., and Frost, C. D., 2006, The Wyoming Province: a distinctive Archean craton in Laurentian North America: Canadian Journal of Earth Sciences, v. 43, no. 10, p. 1391-1397.

Mueller, P. A., Heatherington, A. L., Kelly, D. M., Wooden, J. L., and Mogk, D. W., 2002, Paleoproterozoic crust within the Great Falls tectonic zone: Implications for the assembly of southern Laurentia: Geology, v. 30, no. 2, p. 127-130.

Mueller, P. A., Shuster, R. D., Wooden, J. L., Erslev, E. A., and Bowes, D. R., 1993, Age and composition of Archean crystalline rocks from the southern Madison Range, Montana: Implications for crustal evolution in the Wyoming craton: Geological Society of America Bulletin, v. 105, no. 4, p. 437-446.

Mueller, P. A., Wooden, J. L., Mogk, D. W., and Foster, D. A., 2011, Paleoproterozoic evolution of the Farmington zone: Implications for terrane accretion in southwestern Laurentia: Lithosphere, v. 3, no. 6, p. 401-408.

Mueller, P. A., Wooden, J. L., Mogk, D. W., Nutman, A. P., and Williams, I., 1996, Extended history of a 3.5 Ga trondhjemitic gneiss, Wyoming Province, USA: evidence from U□ Pb systematics in zircon: Precambrian Research, v. 78, no. 1-3, p. 41-52.

Nelson, S. T., Harris, R. A., Dorais, M. J., Heizler, M., Constenius, K. N., and Barnett, D. E., 2002, Basement complexes in the Wasatch fault, Utah, provide new limits on crustal accretion: Geology, v. 30, no. 9, p. 831-834.

O'Neill, J., Klepper, M., Smedes, H., Hanneman, D., Fraser, G., and Mehnert, H., 1996, Geologic map and cross sections of the central and southern Highland Mountains, southwestern Montana.

O'Neill, J. M., and Lopez, D. A., 1985, Character and regional significance of Great Falls tectonic zone, east-central Idaho and west-central Montana: AAPG Bulletin, v. 69, no. 3, p. 437-447.

O'Neill, J. M., and Schmidt, C. J., 1989, Tectonic setting and structural control of gold deposits in cratonic rocks of the Rochester and Silver Star mining districts, Highland Mountains, southwestern Montana.

O'Neill, J., and Berg, R., The Great Falls tectonic zone, Montana–Idaho: an early Proterozoic collisional orogen beneath and south of the Belt Basin, *in* Proceedings Belt Symposium III—1993: Montana Bureau of Mines and Geology Special Publication1998, Volume 112, p. 222-228.

O'Neill, J. M., Duncan, M. S., Zartman, R. E., Lewis, S., and Berg, R., 1988, An early Proterozoic gneiss dome in the Highland Mountains, southwestern Montana: Precambrian and Mesozoic plate margins, p. 81-88.

Ohta, T., and Arai, H., 2007, Statistical empirical index of chemical weathering in igneous rocks: A new tool for evaluating the degree of weathering: Chemical Geology, v. 240, no. 3-4, p. 280-297.

Park, A. F., Treat, R. L., Barr, S. M., White, C. E., Miller, B. V., Reynolds, P. H., and Hamilton, M. A., 2013, Structural setting and age of the Partridge Island block, southern New Brunswick, Canada: a link to the Cobequid Highlands of northern mainland Nova Scotia: Canadian Journal of Earth Sciences, v. 51, no. 1, p. 1-24.

Paton, C., Hellstrom, J., Paul, B., Woodhead, J., and Hergt, J., 2011, Iolite: Freeware for the visualisation and processing of mass spectrometric data: Journal of Analytical Atomic Spectrometry, v. 26, no. 12, p. 2508-2518.

Paton, C., Woodhead, J. D., Hellstrom, J. C., Hergt, J. M., Greig, A., and Maas, R., 2010, Improved laser ablation U-Pb zircon geochronology through robust downhole fractionation correction: Geochemistry, Geophysics, Geosystems, v. 11, no. 3.

Pearce, J. A., 2008, Geochemical fingerprinting of oceanic basalts with applications to ophiolite classification and the search for Archean oceanic crust: Lithos, v. 100, no. 1-4, p. 14-48.

Pearce, J. A., and Stern, R. J., 2006, Origin of back-arc basin magmas: trace element and isotope perspectives: Geophysical Monograph-American Geophysical Union, v. 166, p. 63.

Prucha, J. J., Graham, J. A., and Nickelsen, R. P., 1965, Basement-controlled deformation in Wyoming Province of Rocky Mountains foreland: AAPG Bulletin, v. 49, no. 7, p. 966-992.

Rogers, C., Mackinder, A., Ernst, R., and Cousens, B., 2016, Mafic magmatism in the Belt-Purcell Basin and Wyoming Province of western Laurentia: Geological Society of America Special Papers, v. 522, p. SPE522-510.

Ross, P.-S., and Bédard, J. H., 2009, Magmatic affinity of modern and ancient subalkaline volcanic rocks determined from trace-element discriminant diagrams: Canadian Journal of Earth Sciences, v. 46, no. 11, p. 823-839.

Schmidt, C. J., O'Neill, J. M., and Brandon, W. C., 1988, Influence of Rocky Mountain foreland uplifts on the development of the frontal fold and thrust belt, southwestern Montana: Interaction of the Rocky Mountain Foreland and the Cordilleran Thrust Belt, v. 171, p. 171.

Sears, J., Chamberlain, K., and Buckley, S., 1998, Structural and U-Pb geochronological evidence for 1.47 Ga rifting in the Belt basin, western Montana: Canadian Journal of Earth Sciences, v. 35, no. 4, p. 467-475.

Sláma, J., Košler, J., Condon, D. J., Crowley, J. L., Gerdes, A., Hanchar, J. M., Horstwood, M. S., Morris, G. A., Nasdala, L., and Norberg, N., 2008, Plešovice zircon—a new natural reference material for U–Pb and Hf isotopic microanalysis: Chemical Geology, v. 249, no. 1-2, p. 1-35.

Tilling, R. I., Klepper, M. R., and Obradovich, J. D., 1968, K-Ar ages and time span of emplacement of the Boulder Batholith, Montana: American Journal of Science, v. 266, no. 8, p. 671-689.

Vervoort, J. D., Lewis, R. S., Fisher, C., Gaschnig, R. M., Jansen, A. C., and Brewer, R., 2016, Neoarchean and Paleoproterozoic crystalline basement rocks of north-central Idaho: Constraints on the formation of western Laurentia: Bulletin, v. 128, no. 1-2, p. 94-109.

Whitmeyer, S., and Karlstrom, K., 2007, Tectonic model for the Proterozoic growth of North America, 220 p.:

Wiedenbeck, M., Hanchar, J. M., Peck, W. H., Sylvester, P., Valley, J., Whitehouse, M., Kronz, A., Morishita, Y., Nasdala, L., Fiebig, J., Franchi, I., Girard, J.-P., Greenwood, R. C., Hinton, R., Kita, N., Mason, P. R. D., Norman, M., Ogasawara, M., Piccoli, P. M., Rhede, D., Satoh, H., Schulz-Dobrick, B., Skår, O., Spicuzza, M., Terada, K., Tindle, A., Togashi, S., Vennemann, T., Xie, Q., and Zheng, Y.-F., 2004, Further Characterisation of the 91500 Zircon Crystal: Geostandards and Geoanalytical Research, v. 28, no. 1, p. 9-39.

Wooden, J., and Mueller, P., 1988, Pb, Sr, and Nd isotopic compositions of a suite of Late Archean, igneous rocks, eastern Beartooth Mountains: implications for crust-mantle evolution: Earth and Planetary Science Letters, v. 87, no. 1-2, p. 59-72.

Wooden, J. L., Vitaliano, C. J., Koehler, S. W., and Ragland, P. C., 1978, The late Precambrian mafic dikes of the southern Tobacco Root Mountains, Montana: geochemistry, Rb–Sr geochronology and relationship to Belt tectonics: Canadian Journal of Earth Sciences, v. 15, no. 4, p. 467-479.

Worthington, L. L., Miller, K. C., Erslev, E. A., Anderson, M. L., Chamberlain, K. R., Sheehan, A. F., Yeck, W. L., Harder, S. H., and Siddoway, C. S., 2016, Crustal structure of the Bighorn Mountains region: Precambrian influence on Laramide shortening and uplift in north-central Wyoming: Tectonics, v. 35, no. 1, p. 208-236.

Zhao, G., Cawood, P. A., Wilde, S. A., and Sun, M., 2002, Review of global 2.1–1.8 Ga orogens: implications for a pre-Rodinia supercontinent: Earth-Science Reviews, v. 59, no. 1-4, p. 125-162.

APPENDIX A

FIGURES

Figure 1. Location map of the Wyoming province showing major geologic features of the area. Interpreted area of the craton is shaded. The eastern boundary is based on geophysical evidence from Worthington et al. (2016). Western margin and features from Mueller et al. (2011) and Foster et al. (2006). Northern and southern boundaries, sub-province locations, and Precambrian outcrop locations modified from Harms et al. (2004). Batholith locations from Foster et al. (2010) and Harms et al. (2004).

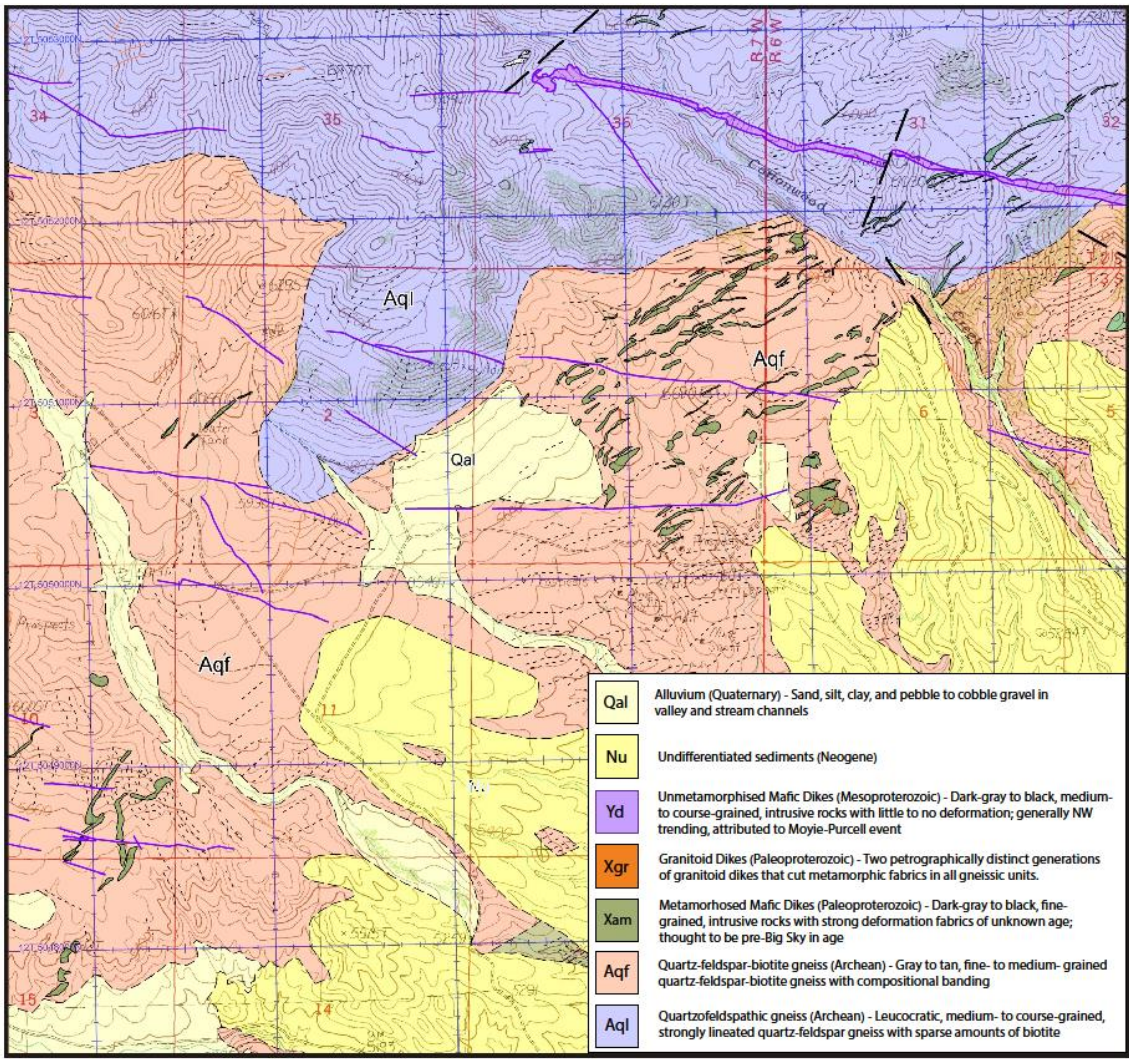

Figure 2. Geologic map of part of the southern Highland Mountains. Two generations of mafic intrusions are shown, (1) deformed, NE-trending group (green) intruded pre-Big Sky and (2) undeformed, NW-trending group (purple). Geology modified from (O'Neill et al., 1996).

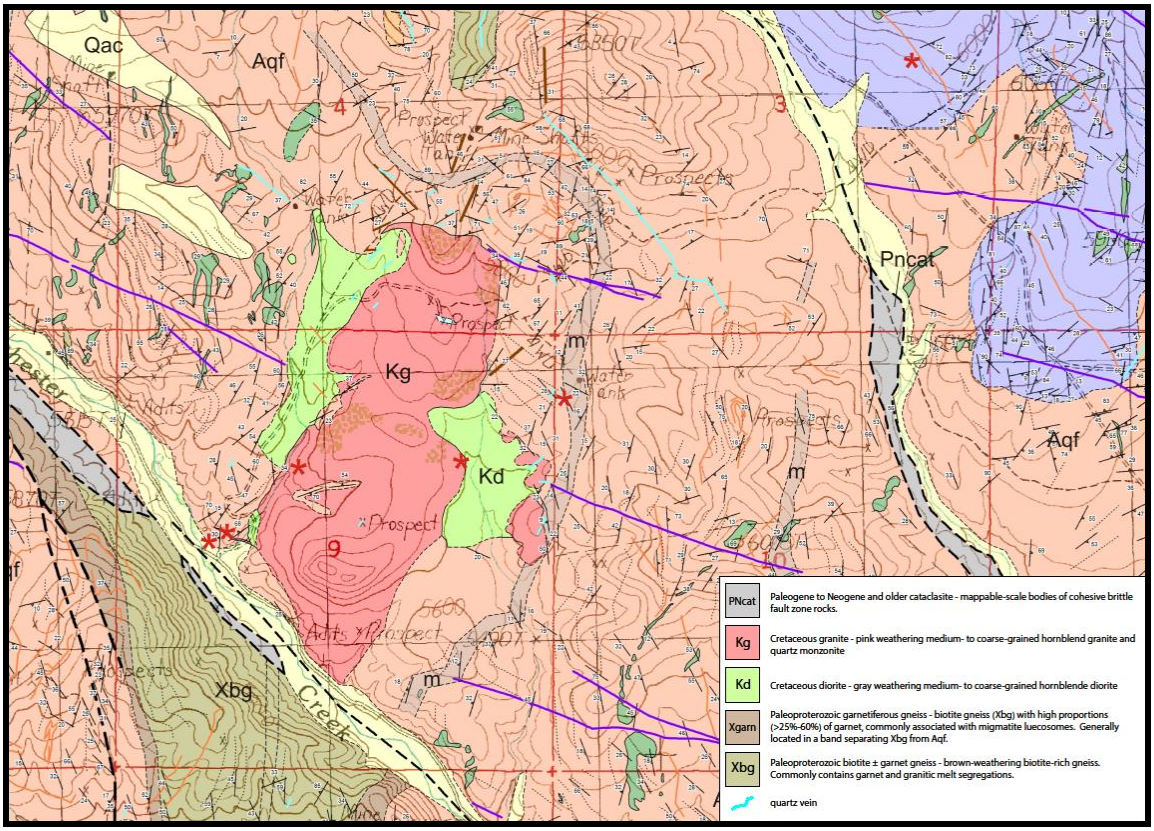

Figure 3. Geologic map of part of the southern Highland Mountains where the Xam unit trends N-S. Units not shown in legend are described in figure 3.

Figure 4. Images showing the amphibolite (Xam) in the field. Foliation can often be seen in hand sample (top). In many areas, the dikes can be seen cutting the gneissic foliation (bottom).

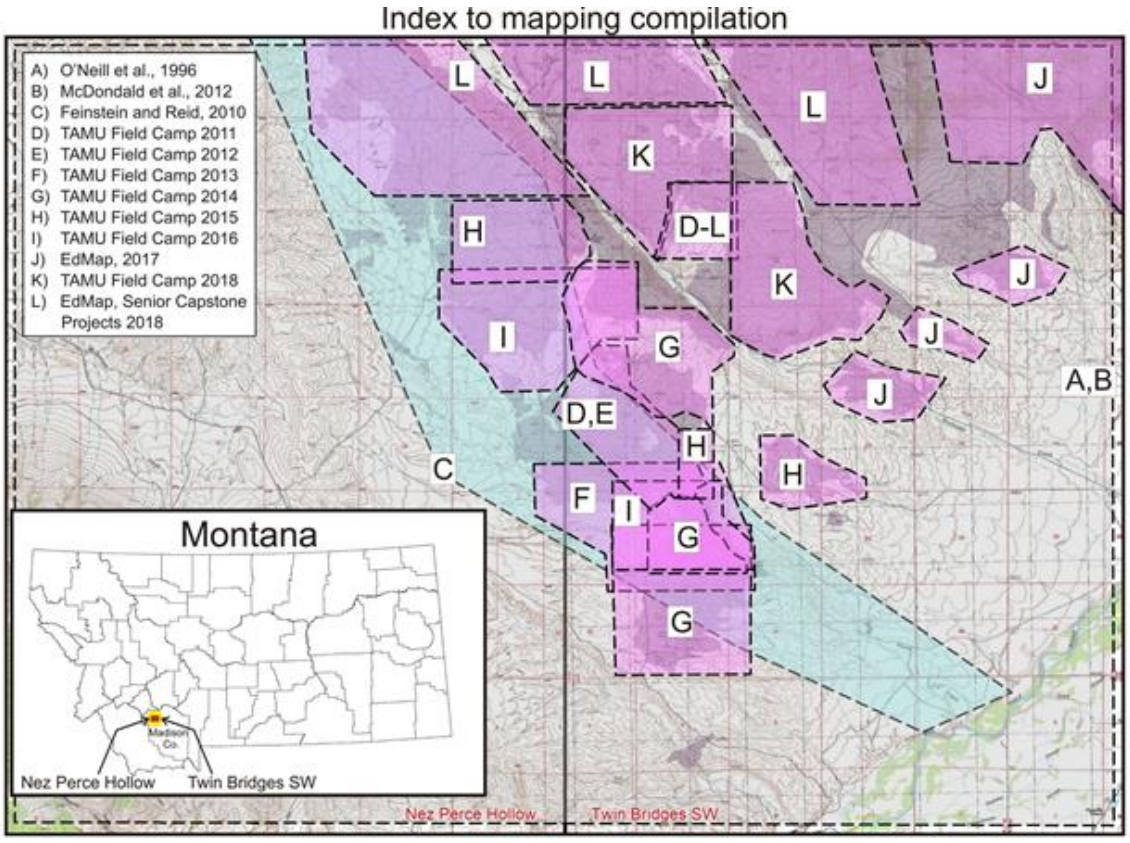

Figure 5. Compilation of bedrock mapping efforts in the Nez Perce Hollow and Twin Bridges SW 7.5' quadrangles.

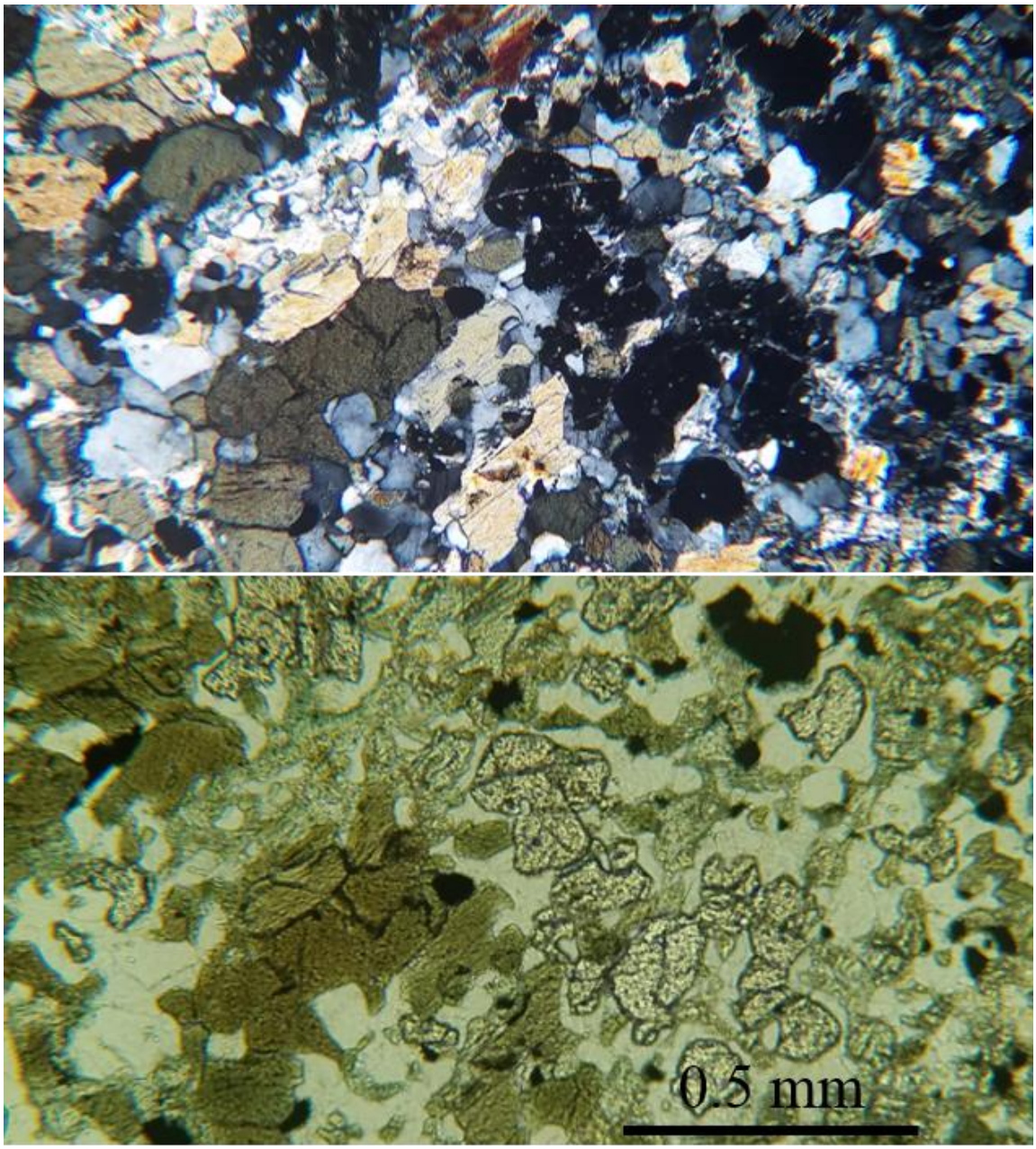

Figure 6. Petrographic images of sample BG17-035, an amphibolite (Xam), taken in crossed-polarized light (top) and plane-polarized light (bottom).

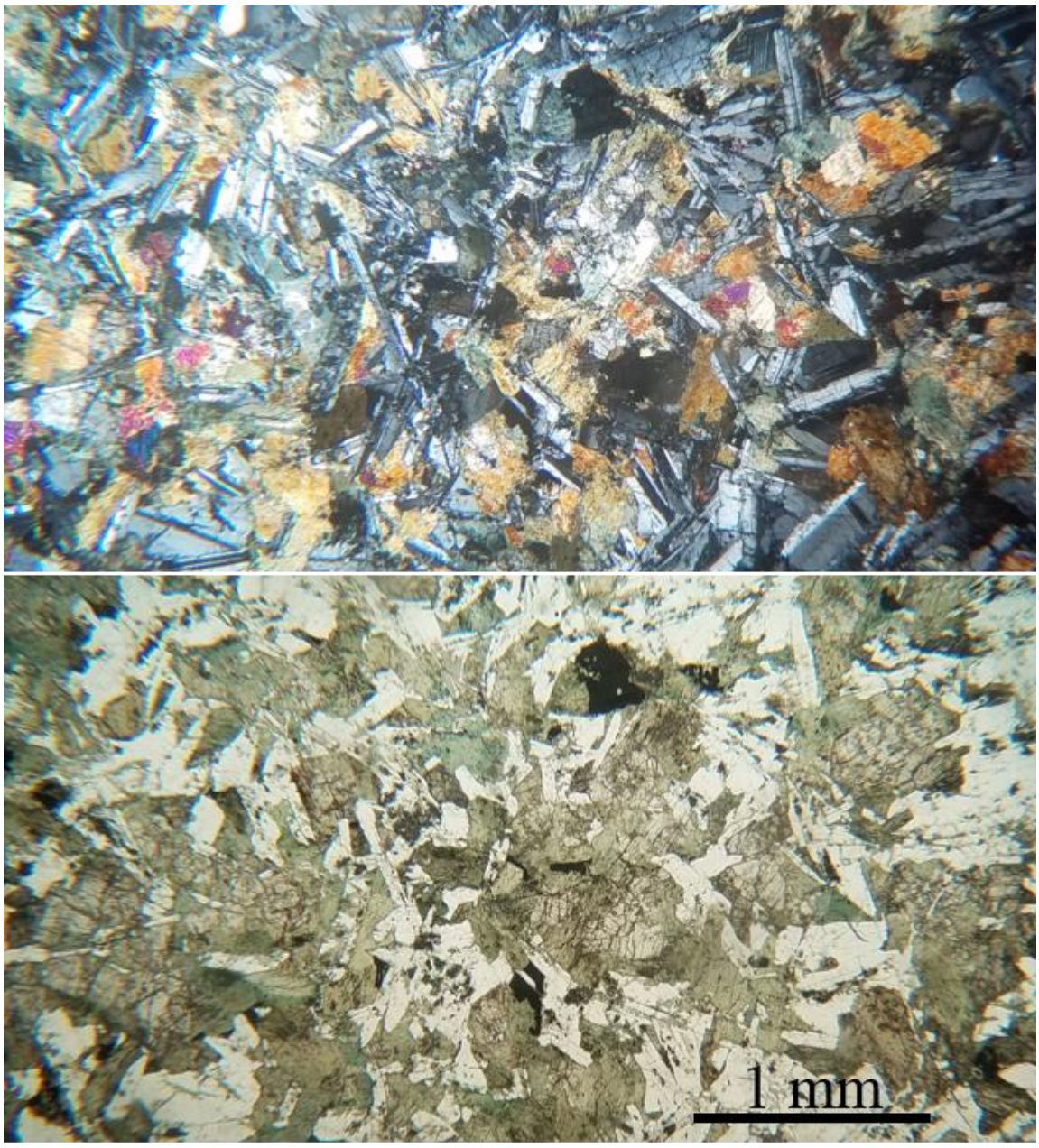

Figure 7. Petrographic image of sample BG17-010, a diabase (Yd) dike, taken in crossed-polarized light (top) and plane-polarized light (bottom).

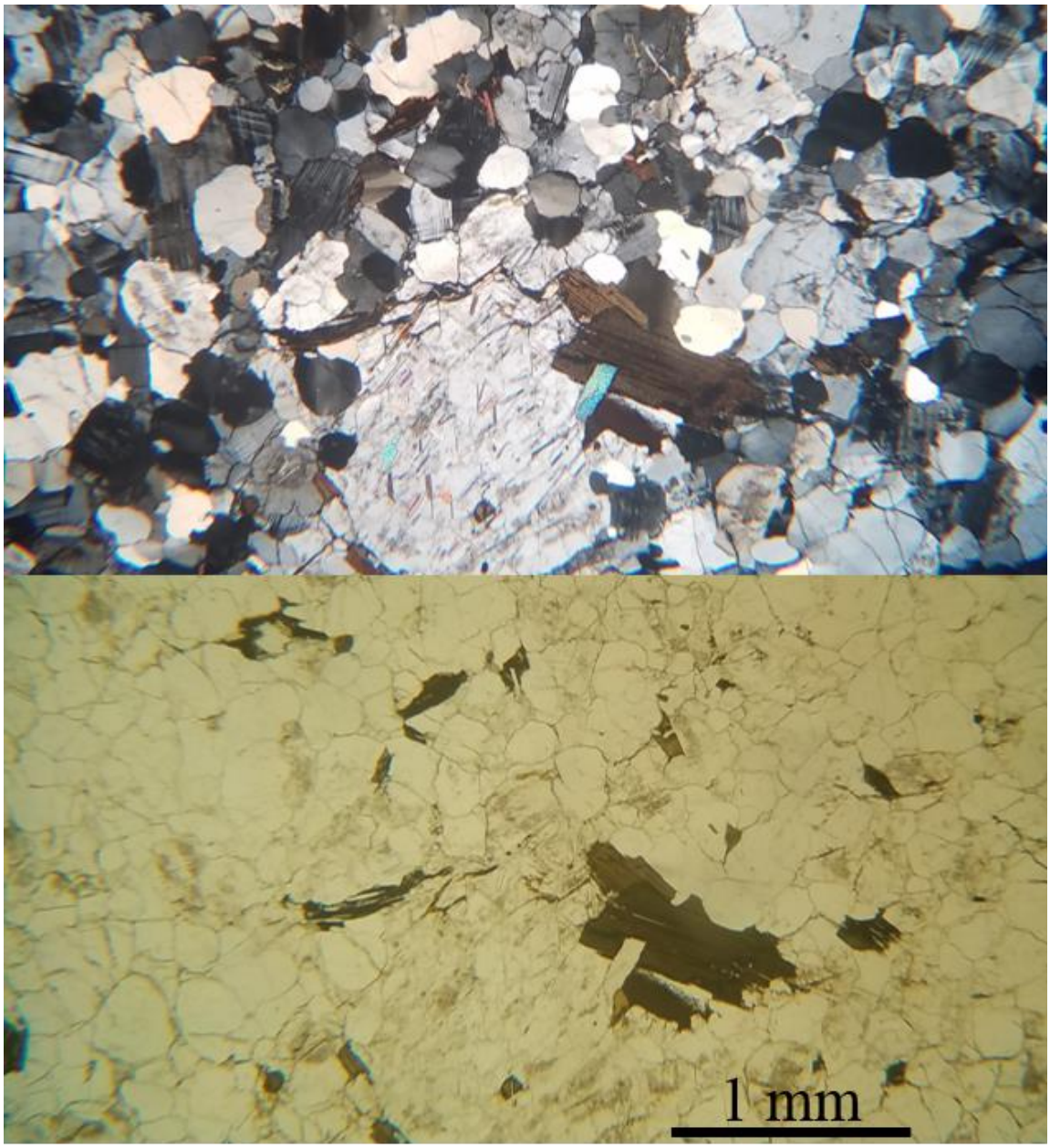

Figure 8. Petrographic image of sample FC15-005, a granitic dike (Xgr1), taken in crossed-polarized light (top) and plane-polarized light (bottom).

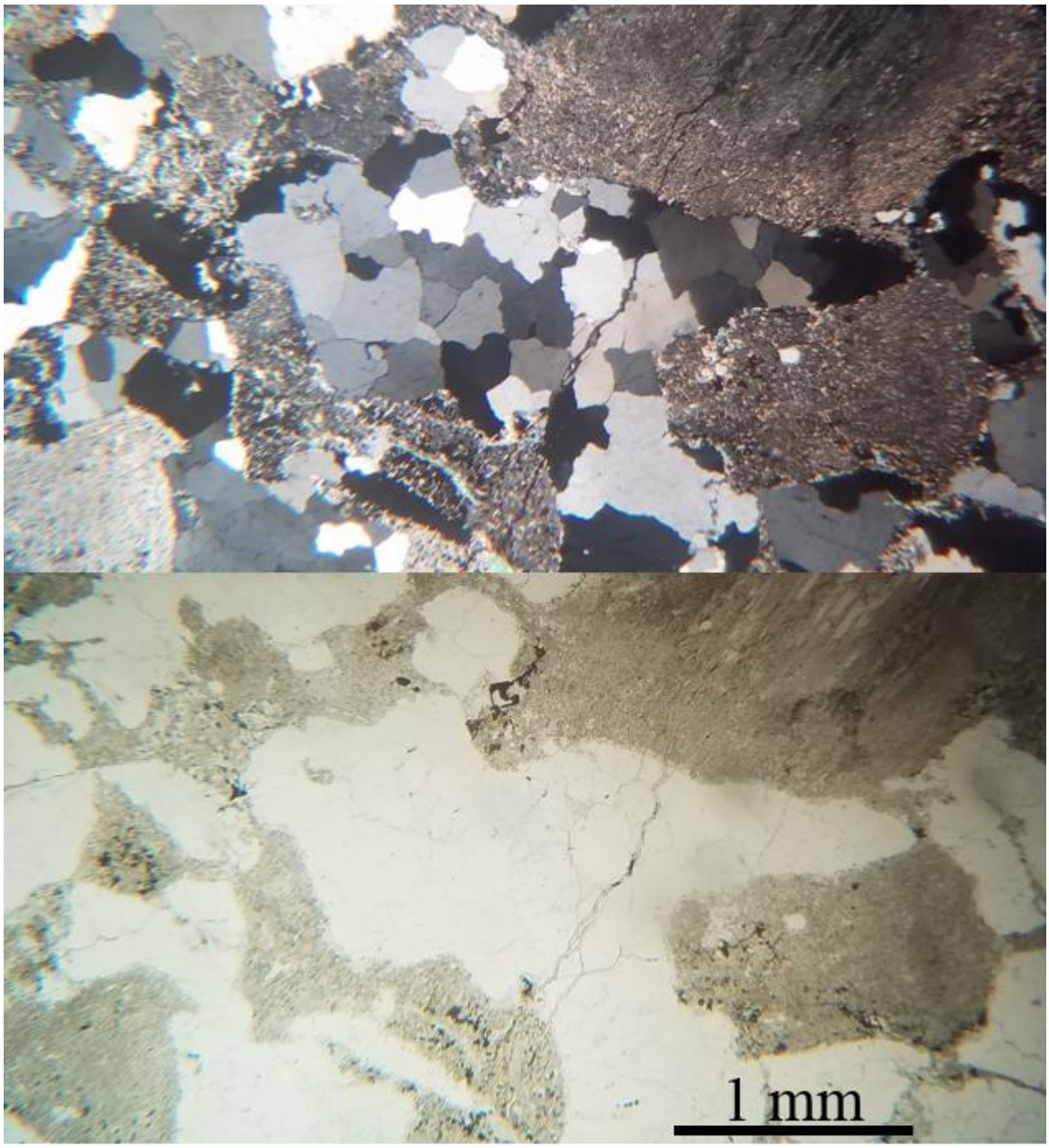

Figure 9. Petrographic image of sample FC14-013, a granitic dike (Xgr2), taken in crossed-polarized light (top) and plane-polarized light (bottom).

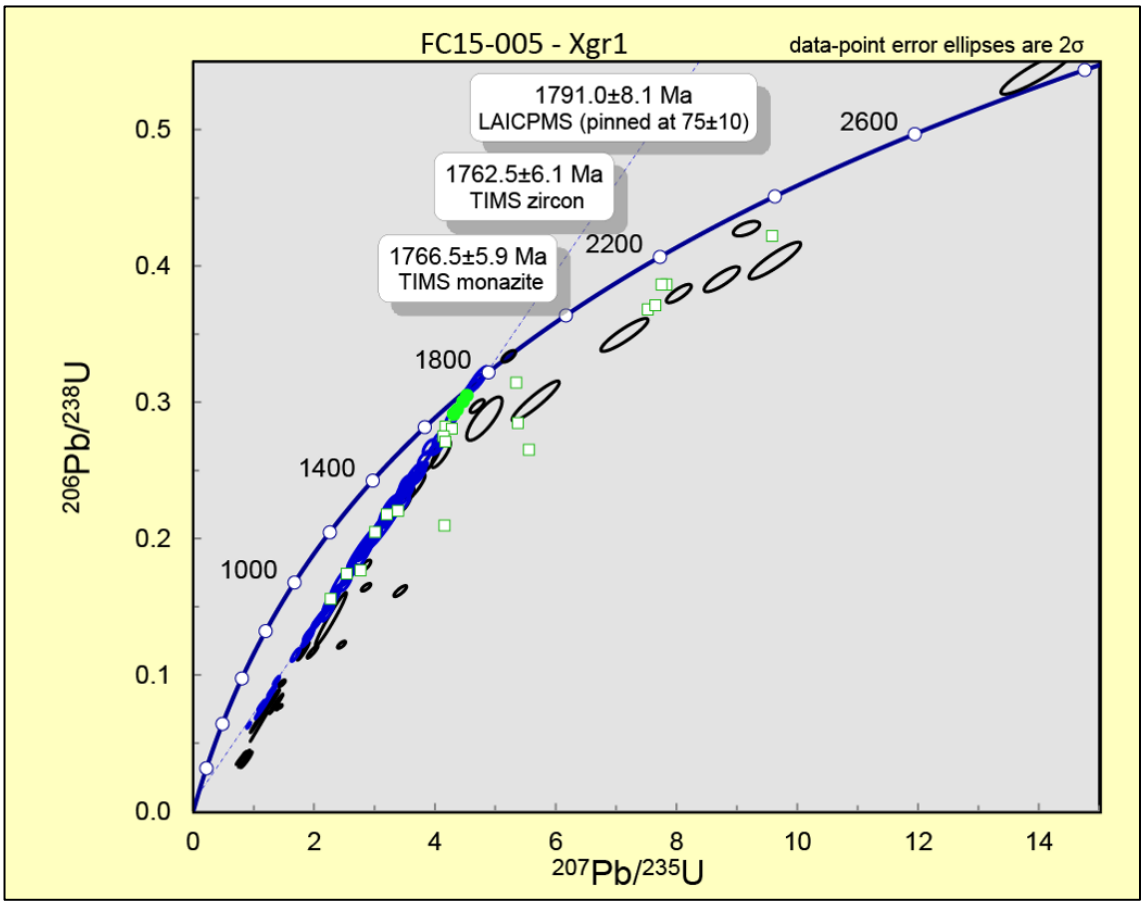

Figure 10. Concordia diagram for zircons and monazites from sample FC15-005. Black ovals represent error ellipses for LA-ICP-MS analyses. Green squares represent TIMS zircons and green circles represent TIMS monazites. The error ellipses from the TIM

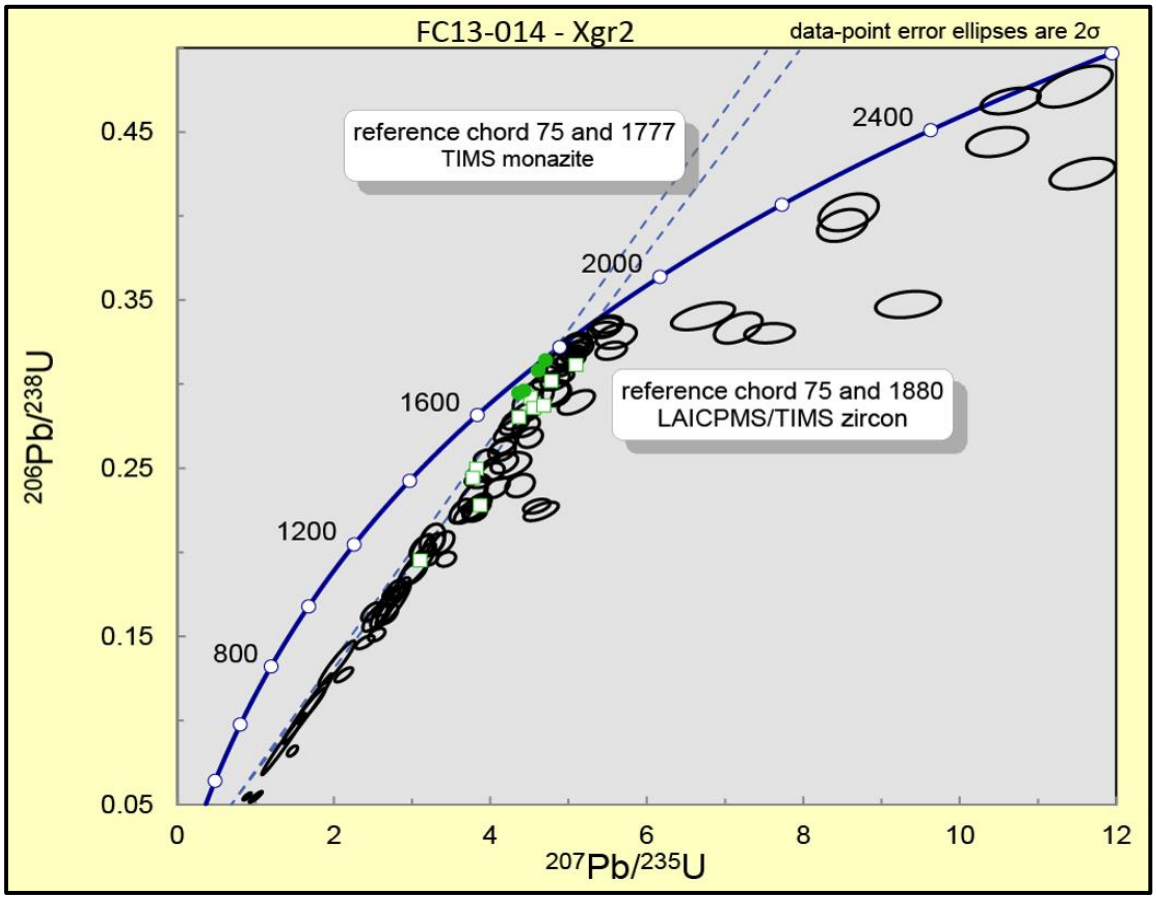

Figure 11. Concordia diagram for zircons and monazites from sample FC13-014. Black ovals represent error ellipses for LA-ICP-MS analyses. Green squares represent TIMS zircons and green circles represent TIMS monazites. The error ellipses from the TIMS data is smaller than the symbol that represents them. See text for description of age calculation.

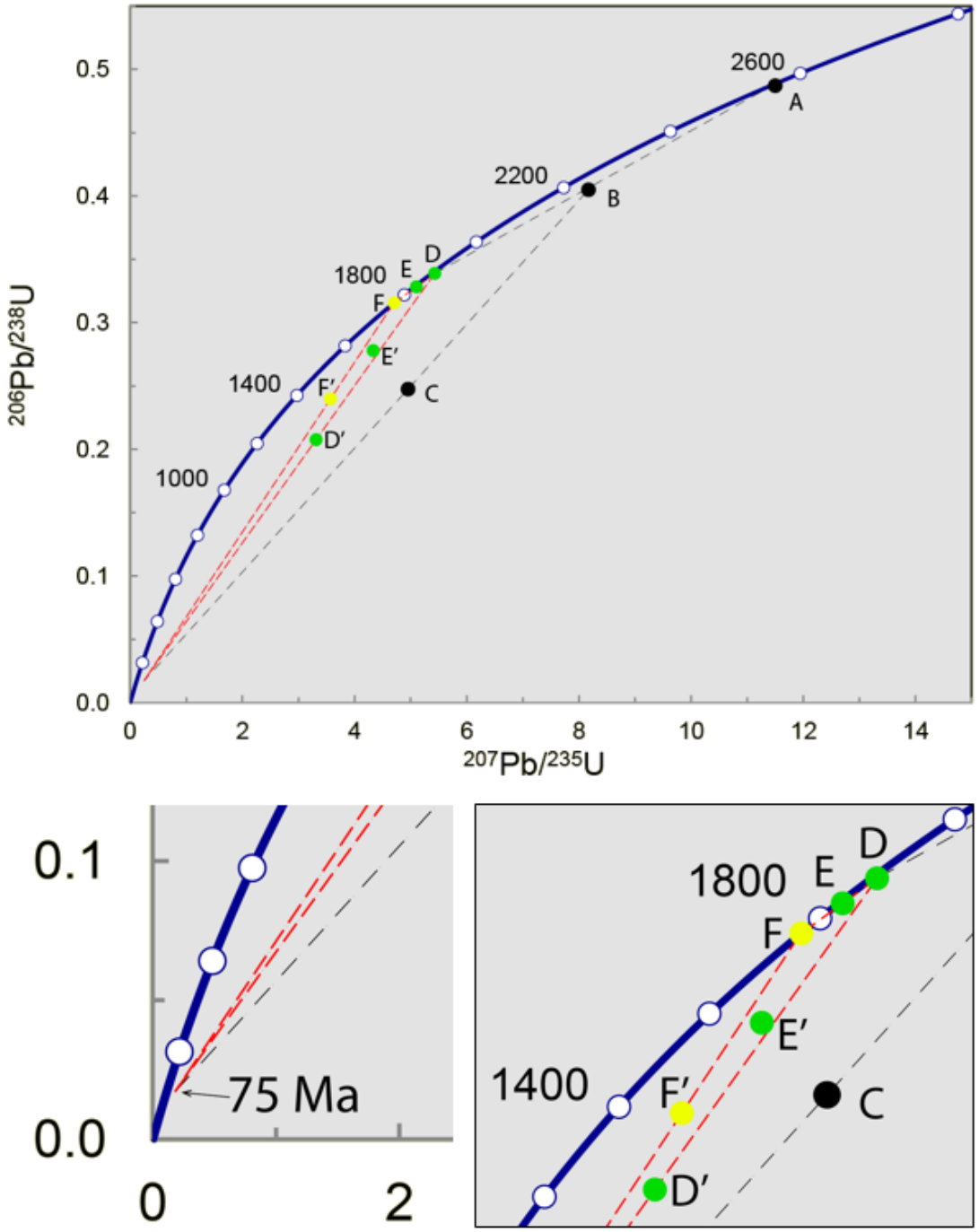

Figure 12. Schematic concordia diagram showing the effect of lead loss and age resetting on zircon analyses. See text for explanation.

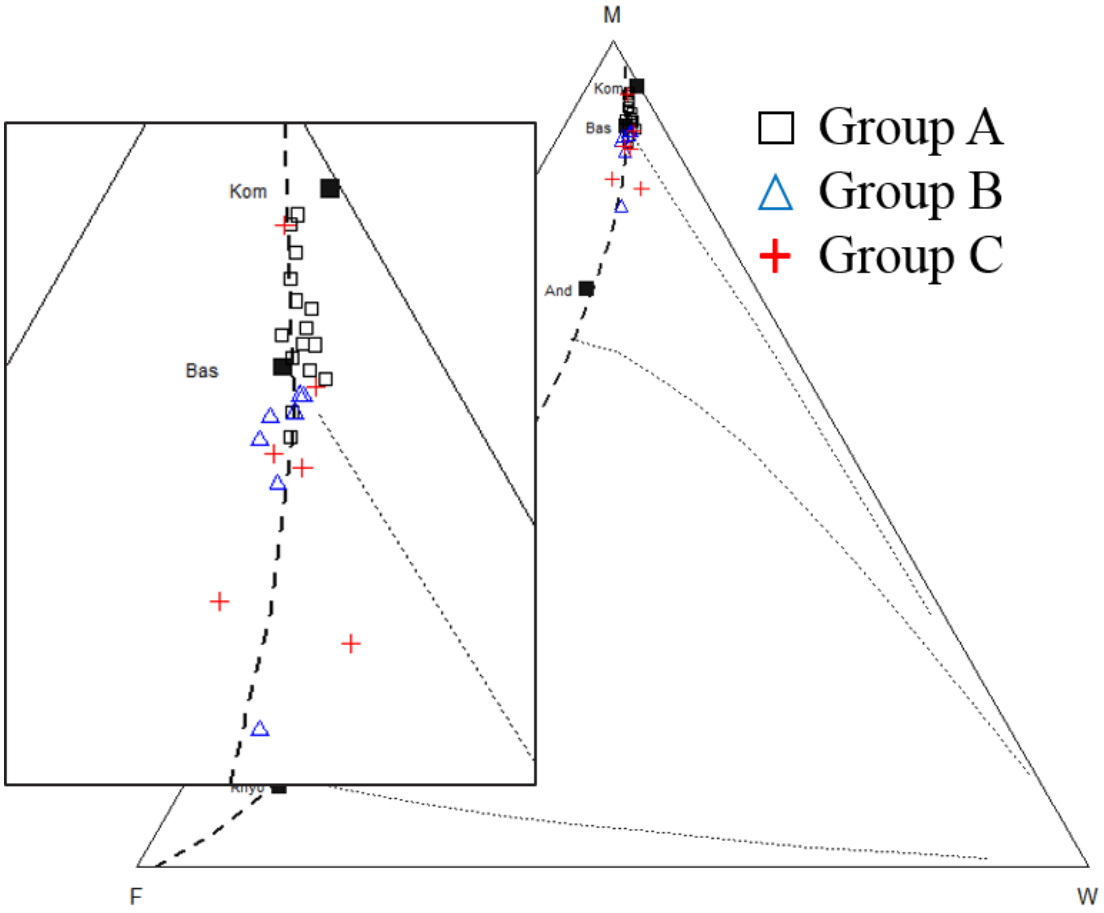

Figure 13. MFW plot from Ohta and Arai (2007) showing the chemical weathering profile of the Xam. All samples plot near the fresh basalt marker (Bas) which indicates little to no chemical weathering of the sample occurred in the portion of the rock that was analyzed. M = mafic parent, F = felsic parent, W = weathered material.

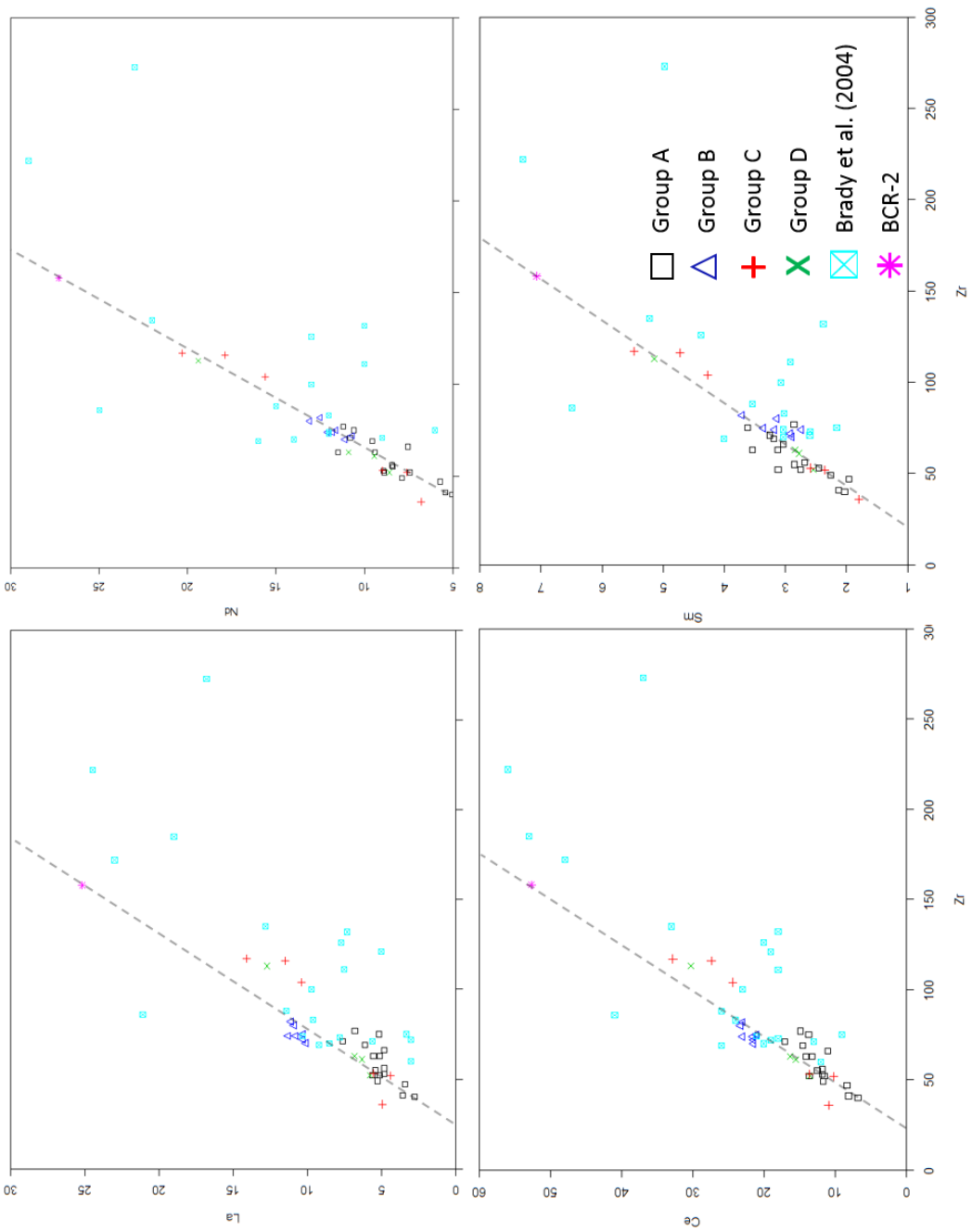

Figure 14. Light rare earth elements plotted against Zr to test mobility as described in MacLean and Barrett (1993). Light elements that were omitted were not available in Brady et al. (2004b). Xam LREE plot linearly through the standard BCR-2. Elements from Brady et al. (2004b) show scatter suggesting mobility of LREE in those rocks.

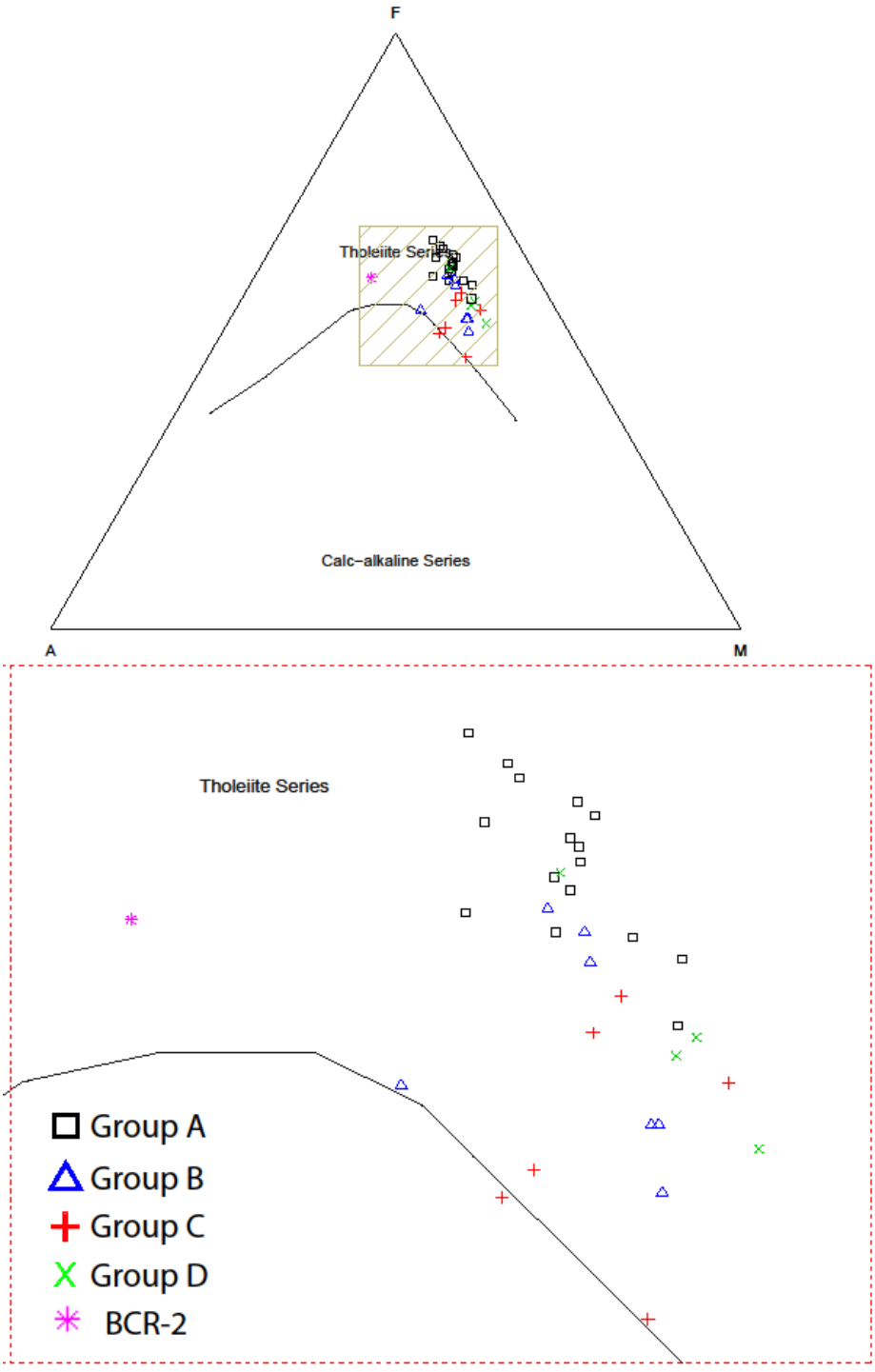

Figure 15. Amphibolites and diabase dike analyses in weight percent oxides are shown on the AFM diagram of Irvine and Baragar (1971). F represents FeO(t). The box (bottom) is a zoomed in view of the yellow inset area of the diagram (top).

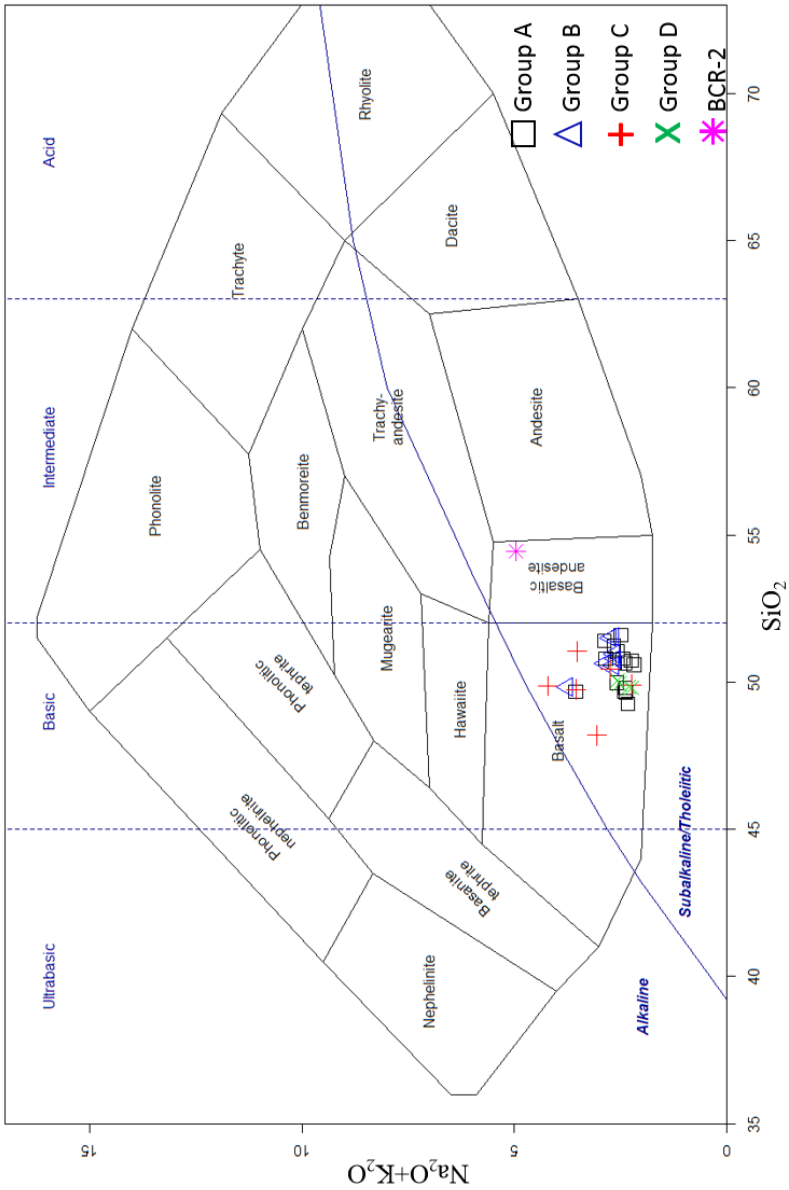

Figure 16. Total Alkali Silica after Cox et al. (1979). All amphibolite and diabase samples are plotted in the tholeiitic basalt field.

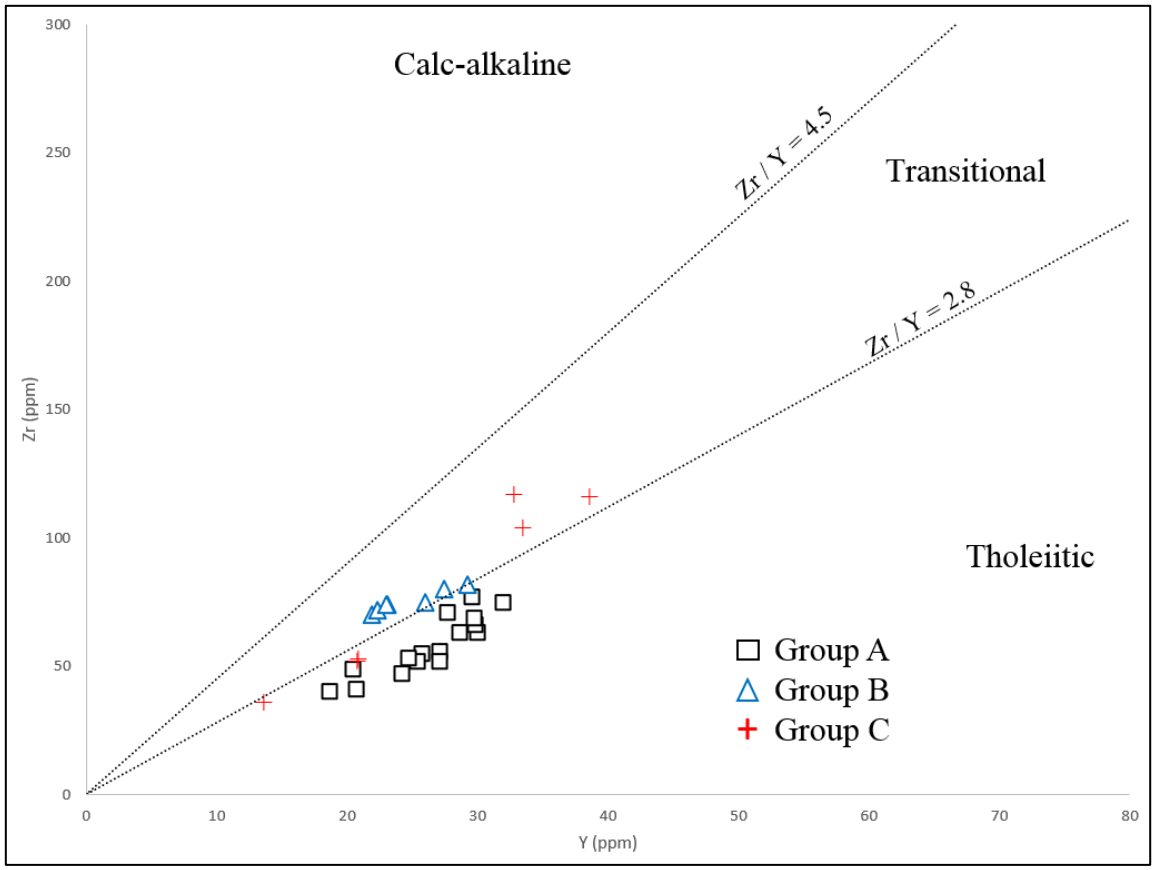

Figure 17. Zr vs. Y plot after Ross and Bédard (2009) showing the magmatic affinity of the amphibolite dikes (Xam). Most of the dikes plot in the tholeiitic field and some plot in the transitional field.

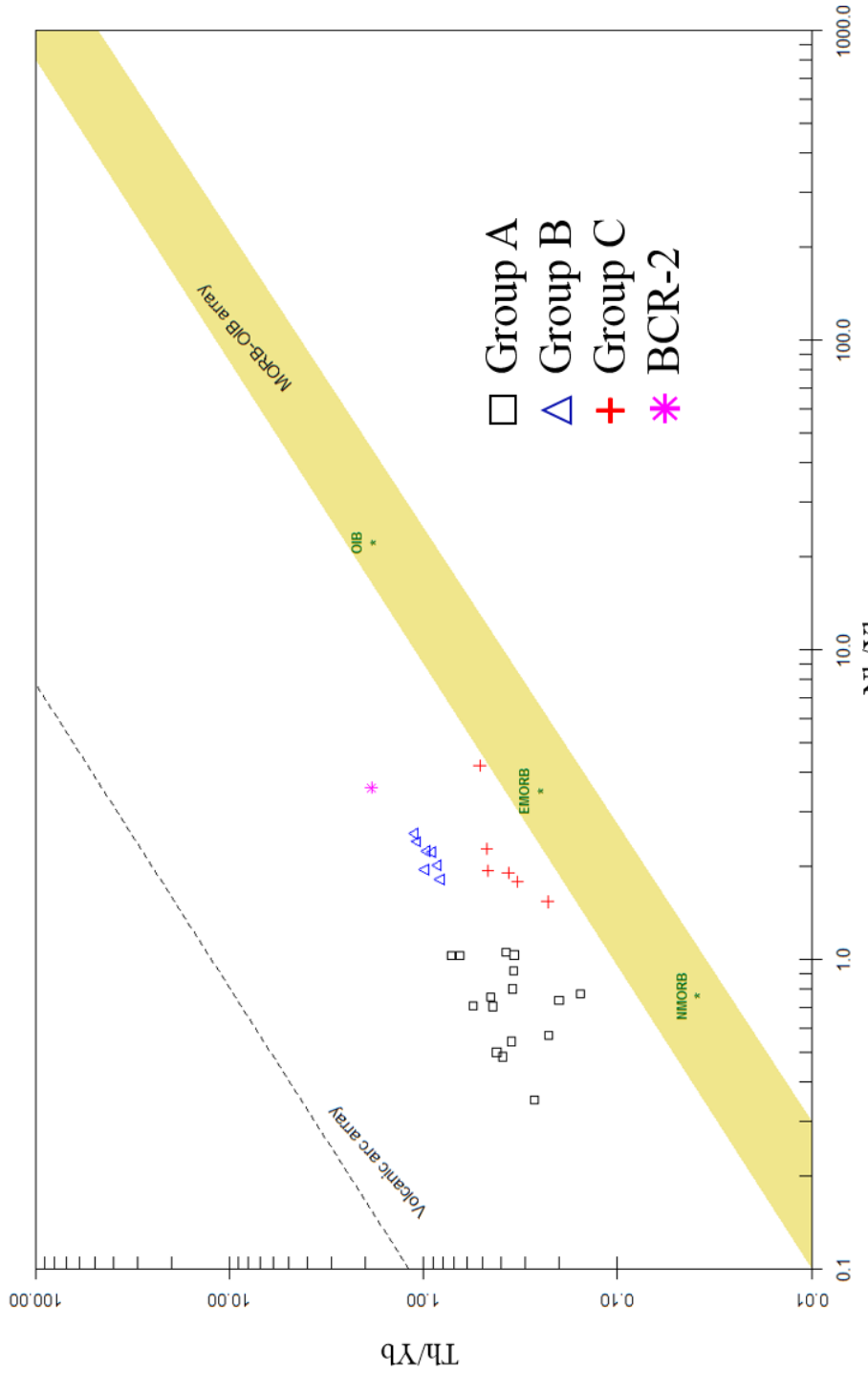

Figure 18. Amphibolite dikes plotted on a Th-Nb-Yb diagram after Pearce (2008). All samples plot above the MORB-OIB highlighted in yellow.

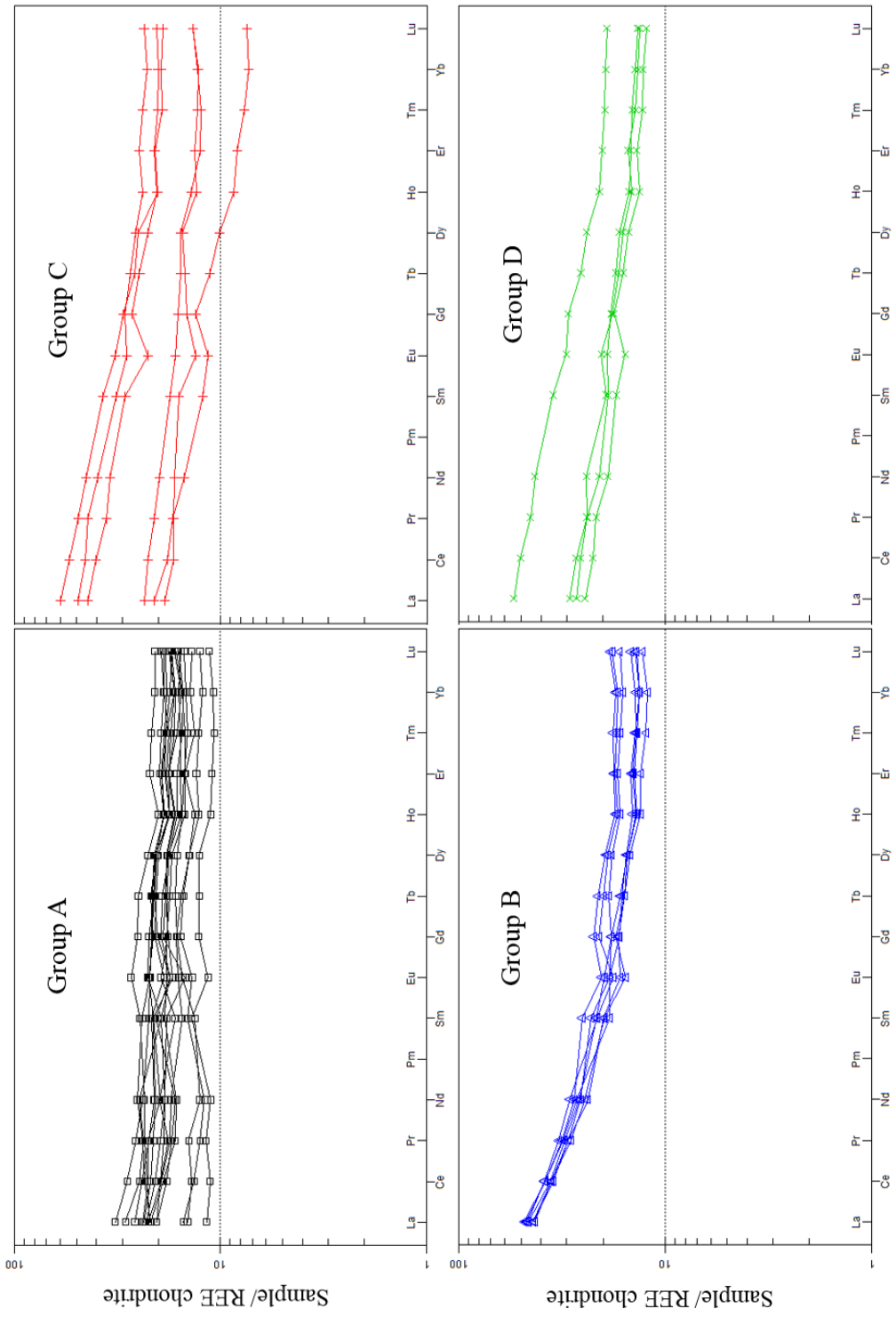

Figure 19. Rare earth elements normalized to chondritic values from McDonough and Sun (1995) for each geochemical grouping of Xam and Yd.

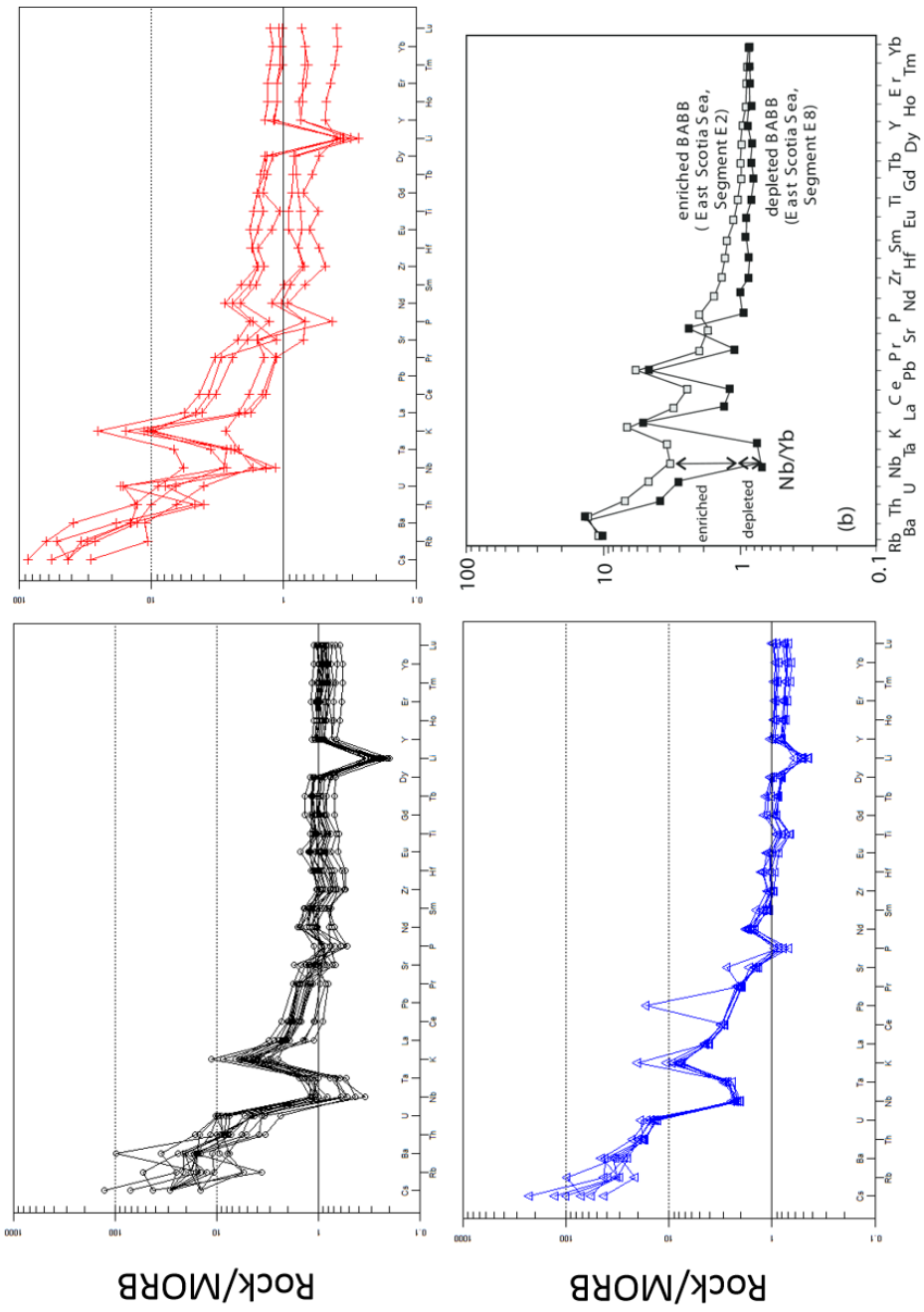

Figure 20. Geochemical patterns from the Xam geochemical groupings compared to back-arc basin basalts (BABB) described in Pearce and Stern (2006). Group A (top left) is depleted in Nb and group B (bottom left) and C (top right) are slightly enriched compared to the BABB baseline described in Pearce and Stern (2006) (bottom right).

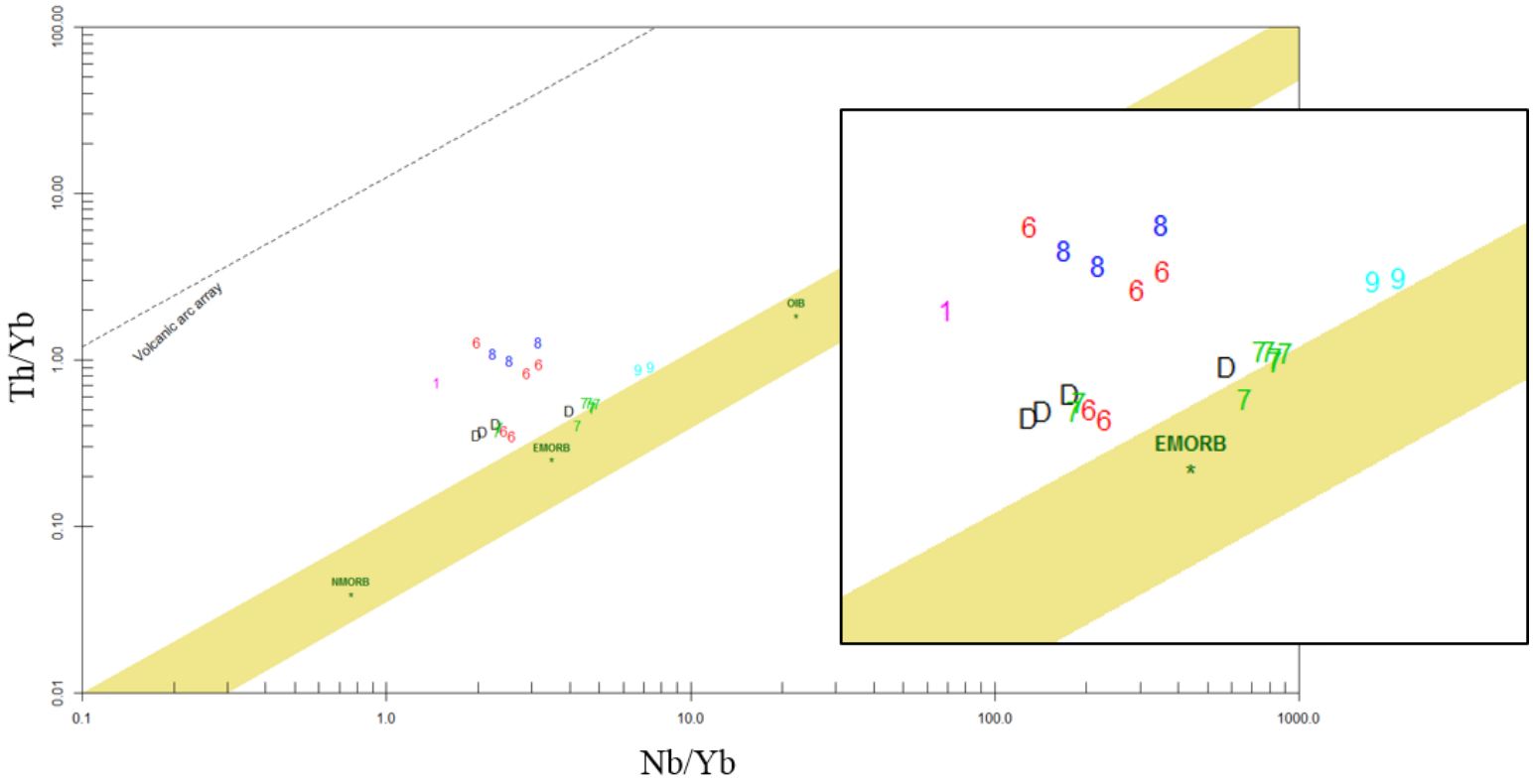

Figure 21. Yd dikes from this study and Rogers et al. (2016) plotted on a Th-Nb-Yb diagram after Pearce (2008). Samples from this study are labeled D and those from Rogers et al. are labeled by their geochemical group number.

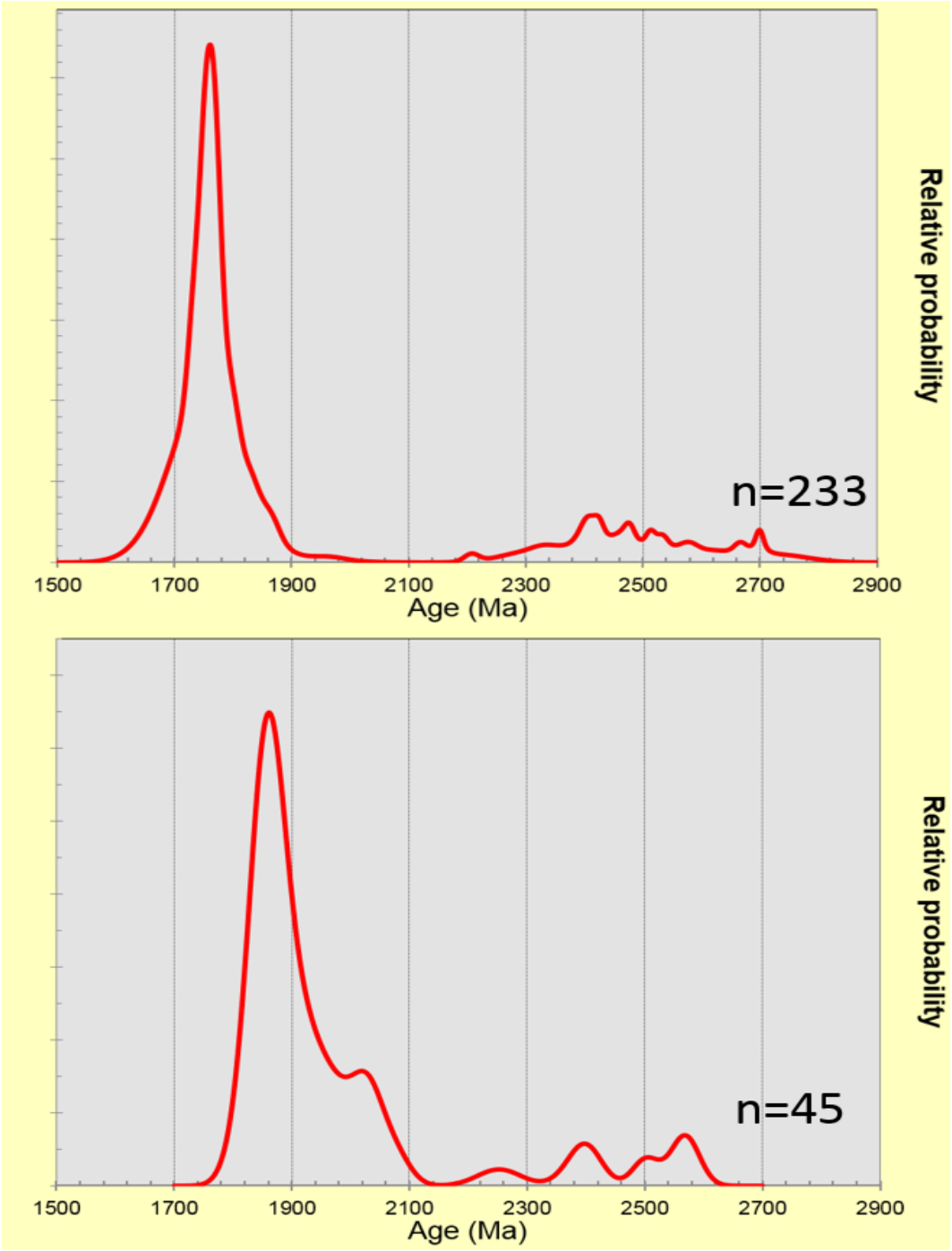

Figure 22. Probability density plots of analyses from three Xgr1 and two Xgr2 samples. Peaks at ~1880 Ma show evidence for a previously unrecognized tectonic event.

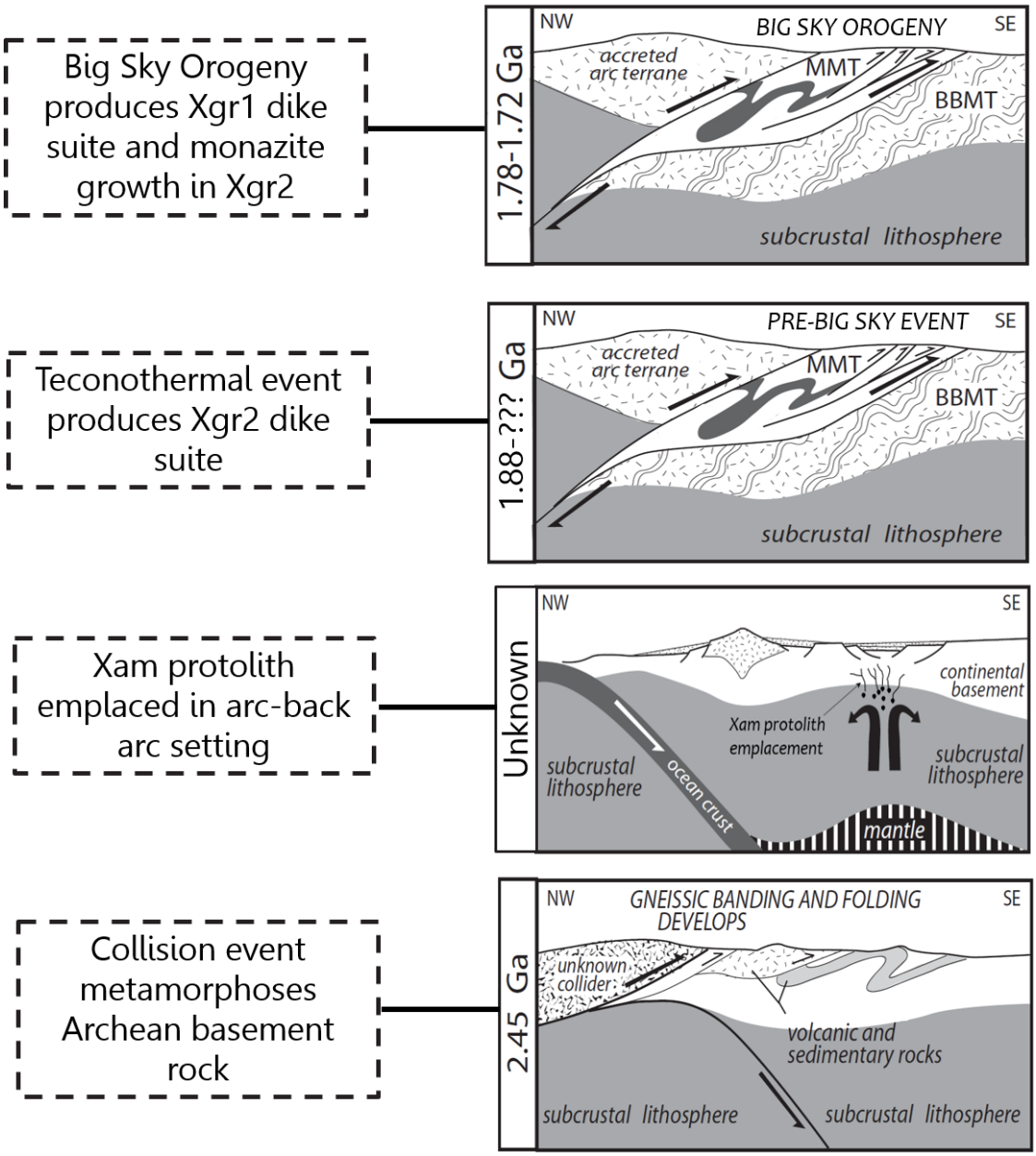

Figure 23. Timeline of tectonic events constrained in this study. 2450 Ma event described by authors in GSA special paper 377 (e.g. Harms et al., 2004). Images modified from the tectonic timeline of Harms et al. (2004).

APPENDIX B

TABLES

Table 1. LA-ICP-MS geochronology analyses

Analysis Identifier	Pb[1] (ppm)	U[1] (ppm)	Th[1] (ppm)	206Pb/204Pb	206Pb/208Pb	± 2SE[2]	208Pb/232Th	± 2SE[2]	207Pb/206Pb	± 2SE[2]	207Pb/235U	± 2SE[2]	206Pb/238U	± 2SE[2]	Rho[3]	208Pb/232Th	± 2SE[2]	207Pb/206Pb	± 2SE[2]	207Pb/235U	± 2SE[2]	206Pb/238U	± 2SE[2]
FC15005_001	368	4040	2640	18500	2.63	0.25	0.016	0.001	0.177	0.0067	0.638	0.023	0.027	0.002	0.75202	315.2	24	2611	64	501	14	168.7	3.2
FC15005_002	136.3	772	198	270000	13.67	1.1	0.08	0.007	0.106	0.0009	4	0.15	0.273	0.01	0.97158	1569	120	1728	16	1630	33	1553	51
FC15005_003	217	1203	505	700000	8.53	0.6	0.048	0.004	0.107	0.0012	2.519	0.1	0.17	0.007	0.96212	953	77	1749	22	1273	30	1011	39
FC15005_004	58.4	674	71	250000	36.4	3.1	0.035	0.008	0.15	0.0029	7.15	0.36	0.344	0.012	0.96112	1825	150	2334	33	2118	44	1902	58
FC15005_005	184	1250	540	600000	8.15	0.72	0.042	0.005	0.109	0.0012	2.09	0.2	0.139	0.012	0.93736	839	96	1779	21	1125	64	834	69
FC15005_006	132	593	154	52000	13.15	1.1	0.037	0.007	0.108	0.0015	4.602	0.12	0.309	0.006	0.85272	1864	140	1759	25	1749	22	1737	30
FC15005_007	264	1358	553	700000	8.38	0.6	0.055	0.005	0.107	0.0016	2.755	0.11	0.184	0.007	0.92779	1090	90	1753	27	1340	28	1090	37
FC15005_008	85.2	278.7	126.2	30000	8.81	0.65	0.077	0.006	0.11	0.0016	4.486	0.11	0.295	0.006	0.8076	1489	110	1800	27	1727	21	1665	27
FC15005_009	47	260	56.7	47000	13.9	1.4	0.093	0.009	0.108	0.0025	3.97	0.16	0.268	0.012	0.8568	1793	160	1758	41	1625	35	1530	60
FC15005_010	811	6530	5630	6630	1.743	0.13	0.016	0.001	0.222	0.0050	0.72	0.023	0.023	5E-04	0.70838	321.4	24	2985	36	550	14	148.9	3.2
FC15005_011	178	1086	418	120000	10.46	0.74	0.049	0.004	0.108	0.0012	2.886	0.092	0.192	0.005	0.94351	961	76	1760	20	1376	23	1132	27
FC15005_012	160.6	898	261	160000	11.97	0.92	0.072	0.006	0.107	0.0010	3.58	0.15	0.243	0.009	0.98081	1411	120	1738	17	1539	33	1399	46
FC15005_013	100.9	538	198	19000	10.13	0.77	0.054	0.004	0.108	0.0014	2.916	0.084	0.196	0.005	0.8935	1068	80	1767	23	1385	22	1154	27
FC15005_014	147	765	229	10000	12.2	0.99	0.073	0.006	0.109	0.0014	3.744	0.11	0.249	0.006	0.8989	1429	110	1774	23	1579	24	1432	33
FC15005_015	93.7	960	353	20300	6.6	0.66	0.032	0.003	0.118	0.0022	1.23	0.13	0.076	0.008	0.9843	630	59	1921	34	797	58	468	48
FC15005_016	111.8	428	135.1	64000	10.98	0.79	0.089	0.007	0.108	0.0013	4.482	0.11	0.302	0.007	0.87336	1716	130	1757	22	1727	21	1700	35
FC15005_017	36.4	356	119	15000	10.68	0.79	0.086	0.007	0.108	0.0013	4.434	0.13	0.298	0.008	0.91224	1670	130	1763	23	1717	24	1678	38
FC15005_018	246	1310	520	10000	9.64	0.85	0.051	0.004	0.175	0.0018	4.4	0.25	0.183	0.01	0.98587	1003	82	2600	18	1704	47	1079	52
FC15005_019	70.9	213	77	30000	8.77	0.73	0.108	0.012	0.161	0.0049	7.54	0.5	0.338	0.027	0.92351	2080	220	2458	52	2171	61	1870	130
FC15005_020	156.1	999	488	34000	7.08	0.51	0.035	0.003	0.11	0.0012	1.82	0.079	0.12	0.005	0.96872	699	57	1789	20	1047	30	729	28
FC15005_021	109.9	495	150	101000	11.46	0.82	0.079	0.006	0.106	0.0012	3.966	0.13	0.271	0.008	0.93906	1544	110	1735	20	1624	26	1543	42
FC15005_022	80.6	466	154.7	19000	10.96	0.89	0.056	0.004	0.108	0.0015	2.942	0.11	0.198	0.006	0.93445	1092	85	1756	26	1390	27	1164	33
FC15005_023	28.7	536	41.4	40000	53	6.7	0.071	0.008	0.159	0.0031	6.05	0.47	0.274	0.017	0.9859	1390	150	2441	32	1970	67	1559	86
FC15005_024	54.1	130	63.2	90000	11.01	1	0.095	0.009	0.109	0.0020	4.91	0.16	0.325	0.008	0.82643	1830	160	1775	34	1803	28	1813	40
FC15005_024	50.7	370	51.8	89000	23.3	4.3	0.105	0.011	0.176	0.0035	9.39	0.36	0.386	0.012	0.85683	2010	200	2615	33	2373	35	2102	54
FC15005_025	104.9	412	131	55000	11.22	0.87	0.085	0.007	0.106	0.0015	4.289	0.12	0.291	0.007	0.86476	1655	120	1736	25	1630	23	1645	34
FC15005_026	34.8	252	51.3	17000	21.7	2.2	0.074	0.007	0.109	0.0016	4.128	0.13	0.275	0.008	0.88385	1438	130	1773	27	1662	27	1567	38
FC15005_027	110.7	469	147.6	63000	11.41	0.82	0.08	0.006	0.107	0.0012	4.087	0.11	0.276	0.006	0.91545	1549	110	1748	20	1650	22	1569	30
FC15005_028	43.1	218.4	48.4	39000	16.15	1.2	0.092	0.008	0.109	0.0014	4.835	0.13	0.319	0.007	0.88177	1779	140	1777	24	1784	30	1786	34
FC15005_029	58.8	345	91	71000	14.5	1.9	0.069	0.007	0.109	0.0026	3.63	0.17	0.243	0.013	0.83532	1340	140	1778	45	1553	40	1398	68
FC15005_030	113.5	493	178	44000	10.1	0.75	0.074	0.007	0.106	0.0012	3.67	0.22	0.251	0.015	0.98215	1433	140	1731	21	1552	52	1438	77
FC15005_031	328.9	1097	527	95000	7.35	0.52	0.067	0.005	0.108	0.0012	3.41	0.13	0.228	0.008	0.9567	1307	100	1764	21	1503	31	1324	43
FC15005_032	103.1	1090	373	51000	9.38	0.7	0.03	0.003	0.107	0.0017	1.338	0.071	0.085	0.005	0.94988	597	54	1738	30	885	31	582	28
FC15005_01	237	1240	337	240000	12.51	1.3	0.076	0.002	0.107	0.0014	3.592	0.071	0.243	0.003	0.75523	1487	46	1755	24	1547	16	1403	17
FC15-005_02	933	9230	5660	910	3.097	0.32	0.019	0.001	0.17	0.0031	0.784	0.028	0.034	0.001	0.86071	374	21	2551	30	586	16	214.5	8.3
FC15-005_02	510	5210	2330	1411	4.41	0.47	0.023	9E-04	0.147	0.0024	0.849	0.018	0.042	8E-04	0.68376	466	18	2308	28	624.1	9.7	265.4	5.1
FC15-005_03	234.9	1574	353	600000	13.89	1.4	0.073	0.003	0.109	0.0018	3.241	0.096	0.219	0.006	0.83209	1417	56	1771	31	1465	23	1275	31
FC15-005_03	98.8	2573	181	25900	21.1	2.3	0.06	0.003	0.126	0.0021	1.373	0.093	0.079	0.006	0.97768	1181	57	2042	29	870	40	488	35
FC15-005_04	207.2	1313	579	60000	11.03	1.1	0.04	0.002	0.109	0.0013	1.857	0.052	0.124	0.003	0.90487	782	33	1773	22	1063	18	754	17
FC15-005_05	243	1138	324	29700	10.14	1.1	0.084	0.004	0.113	0.0016	3.68	0.13	0.238	0.008	0.91531	1621	68	1843	26	1563	29	1373	40
FC15-005_05	211.3	821	245.1	750000	10.72	1.1	0.092	0.003	0.109	0.0014	4.091	0.082	0.271	0.003	0.79232	1780	51	1774	24	1652	16	1548	16
FC15-005_06	303	2460	832	17300	5.86	0.74	0.043	0.003	0.117	0.0023	1.26	0.14	0.079	0.009	0.98543	840	59	1913	34	804	62	484	53
FC15-005_07	132	870	256	2700000	10.67	1.1	0.08	0.003	0.109	0.0015	3.684	0.11	0.245	0.006	0.889	1556	58	1772	26	1565	25	1411	31
FC15-005_07	352	1710	700	5600000	8.34	0.86	0.054	0.002	0.107	0.0015	2.585	0.076	0.176	0.005	0.87953	1070	44	1751	26	1295	21	1044	25
FC15-005_08	208.1	1803	509	1100000	9.99	1	0.045	0.002	0.107	0.0018	1.891	0.054	0.129	0.003	0.81236	895	30	1746	31	1077	19	782	19
FC15-005_08	183.8	1115	322.9	8300000	10.36	1.1	0.061	0.002	0.107	0.0015	2.643	0.051	0.178	0.002	0.71433	1194	38	1754	25	1314	14	1058	9.8
FC15-005_09	116.9	459	131.6	1310000	11.63	1.2	0.095	0.003	0.108	0.0013	4.619	0.09	0.312	0.004	0.80006	1833	54	1756	23	1751	17	1749	19
FC15-005_10	234.2	769	270.9	2600000	8.72	0.9	0.095	0.003	0.109	0.0017	4.293	0.092	0.289	0.005	0.68611	1826	59	1777	25	1631	18	1636	24
FC15-005_10	295	448	219.2	3300000	8.45	1.1	0.144	0.005	0.185	0.0030	13.96	0.48	0.542	0.013	0.90647	2709	79	2638	26	2743	34	2788	55
FC15-005_11	102.2	800	137	1600000	15.86	1.7	0.057	0.003	0.107	0.0016	3.356	0.095	0.227	0.006	0.85003	1124	55	1752	27	1493	22	1318	29
FC15-005_11	288	1683	654	770000	10.02	1.1	0.047	0.002	0.109	0.0016	2.502	0.054	0.168	0.002	0.73448	926	47	1774	27	1272	16	1002	13
FC15-005_11	379	1622	637	3400000	8.75	0.9	0.065	0.003	0.108	0.0015	2.394	0.1	0.2	0.006	0.91026	1265	61	1755	26	1404	26	1173	31
FC15-005_12	325	1430	576	1030000	9.63	1.1	0.062	0.002	0.107	0.0015	3.029	0.069	0.204	0.003	0.79089	1210	40	1747	26	1414	17	1196	18
FC15-005_12	345	1870	781	430000	8.64	0.92	0.049	0.002	0.108	0.0017	2.368	0.053	0.16	0.003	0.7148	967	43	1766	28	1232	16	956	15
FC15-005_13	67.8	1162	69.4	7600000	45.8	5.2	0.108	0.005	0.137	0.0033	5.67	0.32	0.301	0.012	0.93113	2066	91	2179	42	1918	48	1694	60
FC15-005_13	88.8	693	80.9	9200000	32.5	4	0.118	0.005	0.161	0.0025	8.75	0.24	0.39	0.008	0.83638	2251	81	2468	26	2309	25	2123	35
FC15-005_14	156.5	1084	262.4	1.2E+07	13.92	1.4	0.065	0.003	0.108	0.0018	3.25	0.08	0.219	0.005	0.74393	1273	55	1764	31	1468	19	1277	25
FC15-005_14	143.7	855	218.8	1E+07	14.1	1.5	0.073	0.003	0.108	0.0015	3.65	0.073	0.244	0.003	0.72366	1431	50	1760	26	1560	16	1406	16
FC15-005_15	327.7	1803	737	19300	8.45	0.86	0.049	0.002	0.106	0.0014	2.393	0.047	0.164	0.002	0.75415	958	33	1737	24	1240	14	978	11
FC15-005_15	222	1164	454	14700	9.43	0.99	0.053	0.002	0.107	0.0017	2.632	0.084	0.176	0.004	0.87686	1038	35	1749	29	1308	23	1043	23
FC15-005_16	179.3	737	225	1000000	11.34	1.2	0.087	0.003	0.108	0.0015	4.061	0.078	0.273	0.004	0.70261	1691	52	1763	25	1646	16	1557	22
FC15-005_16	37.2	386	114	1030000	13.01	1.4	0.093	0.004	0.107	0.0016	4.72	0.13	0.317	0.008	0.84063	1734	69	1748	28	1763	24	1774	38
FC15-005_17	445.6	1676	737	14100	8.59	0.88	0.067	0.002	0.11	0.0015	3.783	0.078	0.252	0.003	0.77544	1300	42	1796	25	1592	19	1450	15

(Continued)

Table 1. LA-ICP-MS geochronology analyses (continued)

Analysis	Pb[1]	U[1]	Th[1]	206Pb	206Pb	± 2SE[2]	208Pb	± 2SE[2]	207Pb	± 2SE[2]	207Pb	± 2SE[2]	206Pb	± 2SE[2]	Rho[3]	208Pb	± 2SE[2]	207Pb	± 2SE[2]	207Pb	± 2SE[2]	206Pb	± 2SE[2]
Identifier	(ppm)	(ppm)	(ppm)	204Pb	208Pb		232Th		206Pb		235U		238U			232Th		206Pb		235U		238U	
FC15-005_17	317	1196	487	260000	8.32	0.31	0.07	0.002	0.108	0.0014	3.544	0.06	0.235	0.002	0.67693	1365	39	1771	23	1537	13	1363	9.7
FC15-005_18	220	1116	315	890000	11.83	1.3	0.078	0.003	0.107	0.0014	3.674	0.1	0.25	0.005	0.88423	1521	64	1746	27	1564	23	1436	27
FC15-005_18	237.3	1102	454	550000	9.48	0.38	0.056	0.002	0.107	0.0016	2.936	0.064	0.201	0.003	0.71636	1104	36	1745	27	1406	16	1180	15
FC15-005_19	231.8	1481	371	640000	12.1	1.3	0.07	0.003	0.108	0.0014	3.045	0.072	0.206	0.005	0.84005	1362	65	1761	24	1418	18	1204	24
FC15-005_19	287	1208	732	640000	9.18	0.34	0.045	0.004	0.107	0.0015	3.233	0.074	0.216	0.004	0.79744	885	83	1754	25	1464	18	1260	18
FC15-005_20	115.4	581	153.4	300000	13.73	1.4	0.081	0.003	0.108	0.0014	4.182	0.094	0.279	0.005	0.82113	1579	47	1768	23	1668	18	1587	24
FC15-005_21	137.9	2081	333.2	8300	17.05	1.8	0.045	0.002	0.146	0.0022	2.455	0.055	0.122	0.002	0.74008	896	35	2296	26	1258	16	743	12
FC15-005_21	179.3	1216	222.5	3720	11.09	1.2	0.087	0.004	0.153	0.0022	3.427	0.087	0.162	0.003	0.82384	1677	82	2375	25	1509	20	965	18
FC15-005_22	895	1840	836	6080	5.51	0.59	0.116	0.004	0.11	0.0015	4.036	0.085	0.266	0.004	0.76285	2220	66	1790	24	1640	17	1521	20
FC15-005_22	475	1206	518	4800	5.9	0.61	0.098	0.004	0.103	0.0022	3.461	0.1	0.226	0.005	0.71645	1894	68	1782	38	1518	23	1312	25
FC15-005_23	173.6	811	222	137000	12.32	1.3	0.086	0.003	0.108	0.0013	4	0.078	0.267	0.004	0.79293	1674	56	1763	22	1633	16	1526	19
FC15-005_24	316	6100	2322	637	4.71	0.49	0.043	0.002	0.133	0.0024	1.399	0.03	0.076	0.002	0.66151	854	30	2139	31	888	13	474	10
FC15-005_24	645	3800	1101	1188	6.35	0.72	0.066	0.005	0.121	0.0019	1.975	0.075	0.117	0.004	0.91162	1296	95	1962	28	1104	26	713	22
FC15-005_25	244.8	1329	444	5500	8.99	0.95	0.062	0.004	0.108	0.0031	2.8	0.18	0.189	0.013	0.90825	1219	79	1751	53	1349	49	1114	69
FC15-005_25	306	1176	426.6	2890	6.77	0.72	0.078	0.003	0.115	0.0019	2.853	0.071	0.18	0.003	0.74635	1511	56	1871	30	1368	19	1068	18
FC15-005_26	243	1301	373	42000	10.22	1	0.071	0.002	0.108	0.0013	3.005	0.057	0.201	0.002	0.78324	1385	42	1764	23	1408	14	1180	13
FC15-005_26	132	845	253	6000	10.28	1.1	0.082	0.004	0.108	0.0032	3.51	0.12	0.236	0.008	0.64027	1588	68	1761	53	1529	27	1363	43
FC15-005_27	555	4200	1510	730	4.14	0.69	0.044	0.003	0.133	0.0046	1.09	0.12	0.062	0.009	0.93987	866	59	2121	63	730	57	387	54
FC15-005_28	185	2016	631	12000	7.96	0.83	0.03	0.001	0.105	0.0015	1.125	0.048	0.078	0.003	0.94516	587	27	1717	27	762	22	481	17
FC15-005_28	210.5	1487	443	80000	9.93	1	0.051	0.002	0.106	0.0017	2.041	0.059	0.138	0.004	0.83614	1004	34	1725	29	1128	20	834	21
FC15-005_29	153.5	1865	505	4300	11.04	1.5	0.034	0.002	0.114	0.0025	1.465	0.049	0.094	0.002	0.76485	676	35	1857	40	915	20	579	12
FC15-005_29	110.2	977	298	11000	13.18	1.6	0.04	0.002	0.11	0.0016	2.23	0.077	0.145	0.005	0.90761	792	29	1800	27	1188	24	874	26
FC15-005_30	100.3	456	111.5	107000	13.6	1.4	0.098	0.003	0.108	0.0014	4.675	0.1	0.315	0.005	0.79387	1891	55	1755	23	1761	18	1764	23
FC15-005_31	208.6	948	268	132000	11.21	1.2	0.086	0.003	0.108	0.0015	3.826	0.08	0.259	0.004	0.74585	1658	53	1757	25	1537	17	1486	20
FC15-005_31	161.3	689	213.5	61000	10.85	1.1	0.073	0.003	0.108	0.0019	3.727	0.1	0.247	0.006	0.76333	1537	47	1764	33	1576	21	1422	30
FC15-005_32	635	5190	2350	466	3.099	0.32	0.024	0.001	0.154	0.0027	0.893	0.036	0.042	0.002	0.93143	481	22	2387	30	647	19	268	12
FC15-005_32	472	2765	1077	750	4.546	0.47	0.048	0.002	0.135	0.0022	1.436	0.03	0.077	0.001	0.62634	941	30	2159	28	903.6	13	477.5	6.4
FC15-005_33	208.2	1154	364	10800	9.9	1	0.063	0.003	0.108	0.0016	2.9	0.069	0.196	0.004	0.78877	1242	49	1767	27	1381	18	1152	22
FC15-005_33	156.7	809	238.2	11500	11.8	1.2	0.071	0.003	0.108	0.0020	3.453	0.11	0.233	0.006	0.81441	1393	51	1764	33	1515	25	1350	33
FC15-005_33	188.2	1351	571	3830	8.58	0.91	0.036	0.002	0.112	0.0016	1.823	0.081	0.118	0.005	0.95015	712	36	1822	27	1051	29	716	31
FC15-005_34	243	2110	1074	4100	6.54	0.72	0.025	0.002	0.112	0.0025	1.23	0.068	0.08	0.003	0.92955	495	31	1830	40	812	30	498	20
FC15-005_34	152.6	604	340	1680	6.59	0.68	0.049	0.003	0.125	0.0019	2.861	0.064	0.164	0.002	0.74475	973	61	2030	27	1371	17	981	13
FC15-005_35	217.5	2488	870	11700	9.09	0.95	0.028	0.001	0.108	0.0020	1.305	0.057	0.088	0.003	0.90655	554	22	1759	33	846	25	545	20
FC15-005_35	160.9	1468	387	9700	11.88	1.2	0.046	0.002	0.108	0.0013	1.936	0.057	0.13	0.003	0.91875	899	41	1759	22	1092	20	789	18
FC15-005_35	168.6	1233	348	9300	11.42	1.2	0.052	0.002	0.107	0.0017	2.28	0.12	0.153	0.008	0.9532	1028	46	1744	29	1204	38	915	43
FC15-005_36	151.7	322.4	171.3	44000	6.78	0.7	0.097	0.003	0.114	0.0015	5.222	0.093	0.334	0.004	0.68103	1868	55	1864	24	1856	15	1856	17
FC15-005_37	155.4	364	173.1	31000	6.95	0.72	0.097	0.003	0.115	0.0016	4.699	0.096	0.297	0.004	0.73731	1872	56	1874	26	1766	17	1677	19
FC15-005_38	276.8	1364	463	110000	9.31	0.97	0.067	0.003	0.107	0.0016	3.088	0.098	0.21	0.006	0.88283	1313	61	1752	27	1428	24	1229	32
FC15-005_38	205.2	933	278	152000	10.82	1.1	0.08	0.003	0.108	0.0017	3.555	0.093	0.241	0.006	0.81386	1559	51	1765	29	1539	20	1391	32
FC15-005_38	188.2	919	271	77000	10.59	1.1	0.075	0.003	0.108	0.0016	3.192	0.072	0.213	0.004	0.75286	1465	55	1767	32	1455	17	1244	19
FC15-005_39	249	1137	374	139000	9.83	1.1	0.075	0.003	0.109	0.0016	3.54	0.12	0.238	0.008	0.90216	1455	62	1779	26	1533	28	1373	40
FC15-005_39	186.1	825	242	47000	11.45	1.2	0.084	0.003	0.108	0.0016	3.898	0.076	0.267	0.004	0.66938	1637	58	1756	27	1613	16	1526	22
FC15-005_39	223.5	930	353	185000	9.24	0.98	0.069	0.002	0.108	0.0017	3.247	0.071	0.218	0.004	0.71255	1339	45	1759	29	1468	17	1269	22
FC15-005_40	367	1533	523	113000	8.94	0.91	0.075	0.002	0.108	0.0014	3.276	0.06	0.22	0.002	0.72467	1470	46	1769	23	1475	14	1280	12
FC15-005_40	361	1497	481	200000	9.27	0.96	0.083	0.003	0.108	0.0018	3.52	0.079	0.241	0.004	0.67698	1604	52	1763	30	1531	18	1393	22
FC15-005_41	171.5	1762	648	16700	11.52	1.2	0.03	0.002	0.112	0.0017	1.787	0.055	0.117	0.003	0.87153	594	34	1834	27	1039	20	713	17
FC15-005_41	155.1	934	263	17900	12.36	1.3	0.069	0.006	0.11	0.0017	3.16	0.2	0.208	0.012	0.97141	1340	120	1793	29	1441	50	1215	64
FC15-005_42	225.3	1778	537	13400	9.16	0.94	0.046	0.002	0.109	0.0016	1.864	0.04	0.125	0.002	0.73223	912	37	1788	26	1068	14	761	11
FC15-005_42	171	1641	780	5220	6.31	0.74	0.026	0.003	0.118	0.0022	1.08	0.11	0.067	0.008	0.89223	512	51	1921	34	729	52	417	46
FC15-005_43	534	2212	780	136000	9.23	0.94	0.077	0.003	0.108	0.0013	3.423	0.064	0.231	0.003	0.79755	1495	53	1770	23	1509	15	1339	13
FC15-005_44	176.6	2671	822	12900	8.68	0.9	0.024	0.001	0.107	0.0018	0.317	0.027	0.063	0.002	0.83172	476	20	1745	31	660	14	394	11
FC15-005_44	142.3	1573	504	3200	8.68	0.9	0.03	0.001	0.108	0.0018	1.141	0.029	0.077	0.002	0.75542	606	21	1756	30	773	14	478.3	9.5
FC15-005_45	105	790	93.7	330000	27	2.8	0.123	0.004	0.156	0.0020	8.04	0.17	0.38	0.006	0.80237	2346	76	2405	22	2234	19	2074	26
FC15-005_45	82.9	495	70.5	240000	26.66	2.8	0.127	0.006	0.155	0.0025	9.16	0.18	0.427	0.004	0.57171	2411	110	2398	27	2354	18	2294	20
FC15-005_46	243.5	1289	353	25000	10.25	1.1	0.077	0.003	0.109	0.0024	3.232	0.098	0.218	0.007	0.75321	1500	56	1773	42	1471	18	1273	38
FC15-005_46	280	1630	673	20000	9.48	1	0.046	0.004	0.107	0.0020	2.4	0.11	0.167	0.008	0.92621	916	74	1741	34	1241	33	994	46
FC15-005_46	212.1	973	312	146000	9.89	1	0.074	0.002	0.108	0.0014	3.173	0.066	0.214	0.003	0.78508	1445	45	1769	26	1450	16	1247	17
FC15-005_47	147	1079	229	330000	12.44	1.5	0.074	0.003	0.106	0.0022	2.81	0.21	0.194	0.013	0.9627	1430	160	1725	38	1354	57	1140	71
FC15-005_47	213.9	1630	456	28700	10.36	1.1	0.052	0.002	0.109	0.0018	2.08	0.085	0.141	0.006	0.91622	1017	39	1787	30	1141	28	849	31
FC15-005_47	188	1185	322	230000	11.77	1.2	0.064	0.002	0.109	0.0016	2.787	0.066	0.188	0.003	0.78268	1257	41	1772	26	1351	18	1110	18
FC15-005_48	200.1	1075	277.9	150000	10.28	1.1	0.081	0.004	0.108	0.0037	3.26	0.15	0.22	0.01	0.72052	1571	80	1766	63	1471	38	1261	53
FC15-005_48	256	1654	556	52000	9.07	0.96	0.052	0.005	0.109	0.0027	2.277	0.1	0.154	0.006	0.8309	1014	89	1784	44	1204	32	923	35
FC15-005_48	240.1	1136	396	43000	9.71	1	0.066	0.002	0.109	0.0017	2.992	0.074	0.203	0.003	0.79615	1298	43	1780	28	1405	19	1189	16

(Continued)

Table 1. LA-ICP-MS geochronology analyses (continued)

Analysis	Pb[1]	U[1]	Th[1]	206Pb	206Pb	± 2SE[2]	208Pb	± 2SE[2]	207Pb	± 2SE[2]	207Pb	± 2SE[2]	206Pb	± 2SE[2]	Rho[3]	208Pb	± 2SE[2]	207Pb	± 2SE[2]	207Pb	± 2SE[2]	206Pb	± 2SE[2]
Identifier	(ppm)	(ppm)	(ppm)	204Pb	208Pb		232Th		206Pb		235U		238U			232Th		206Pb		235U		238U	
FC15-005_48	183.4	810	258	290000	10.37	1.1	0.081	0.004	0.108	0.0015	3.566	0.1	0.239	0.006	0.87013	1564	69	1771	26	1540	22	1381	31
FC15-005_49	1007	2030	977	34100	4.92	0.53	0.116	0.005	0.112	0.0017	3.92	0.13	0.257	0.008	0.88382	2208	82	1835	28	1616	27	1475	40
FC15-005_49	574	1383	518	33700	5.77	0.6	0.122	0.004	0.111	0.0015	3.563	0.075	0.233	0.003	0.77768	2323	76	1816	24	1540	17	1352	17
FC15-005_50	217.6	1027	302	127000	10.61	1.1	0.081	0.003	0.109	0.0014	3.463	0.067	0.233	0.003	0.74341	1567	50	1785	24	1518	15	1350	17
FC15-005_50	172	472	166	10100	8.1	0.97	0.113	0.008	0.121	0.0036	4.82	0.24	0.288	0.013	0.80757	2170	150	1965	54	1786	43	1631	64
FC15-005_51	219	2034	834	32000	8.2	0.84	0.03	0.002	0.106	0.0015	1.378	0.043	0.096	0.003	0.89133	587	29	1729	26	878	18	590	15
FC15-005_51	198.8	1372	505	260000	9.05	0.94	0.044	0.003	0.107	0.0014	1.933	0.09	0.132	0.006	0.95987	872	48	1741	24	1088	32	796	32
FC15-005_52	273.9	1278	361.3	340000	10.52	1.1	0.083	0.003	0.108	0.0013	3.454	0.061	0.234	0.002	0.76845	1612	47	1763	22	1516	14	1355	11
FC15-005_53	410.2	1536	546	420000	7.305	0.74	0.083	0.003	0.107	0.0013	2.854	0.051	0.194	0.002	0.76773	1608	51	1753	21	1370	14	1145	10
FC15-005_54	243.1	1893	584	37700	8.74	0.9	0.048	0.002	0.11	0.0018	1.911	0.063	0.128	0.004	0.87219	940	43	1800	30	1083	22	774	23
FC15-005_54	130.1	1274	331	180000	10.05	1	0.053	0.002	0.107	0.0014	2.139	0.039	0.143	0.002	0.6795	1038	32	1755	23	1180	12	835.9	9.5
FC15-005_55	88.6	877	62.9	310000	32.3	3.6	0.117	0.005	0.149	0.0034	7.14	0.32	0.35	0.01	0.90287	2242	88	2330	41	2117	43	1929	48
FC15-005_55	183.3	652	145.7	340000	14.89	1.8	0.136	0.004	0.172	0.0029	9.63	0.35	0.404	0.011	0.89903	2572	79	2579	28	2396	33	2186	51
FC15-005_56	207.7	1701	583	48000	11.33	1.2	0.041	0.002	0.11	0.0016	2.273	0.066	0.153	0.004	0.86436	808	37	1789	27	1203	21	916	23
FC15-005_56	192.4	2085	905	22300	8.08	0.96	0.025	0.002	0.111	0.0017	1.17	0.12	0.078	0.008	0.36944	489	41	1809	27	768	54	481	49
FC15-005_57	107.6	834	287	116000	10.4	1.1	0.041	0.002	0.108	0.0017	2.029	0.054	0.138	0.003	0.80951	814	35	1767	28	1124	18	833	18
FC15-005_58	929	6880	2880	2350	2.49	0.27	0.037	0.004	0.151	0.0033	0.8	0.072	0.039	0.004	0.36238	742	79	2356	37	538	42	247	25
FC15-005_58	286	1130	640	3200	5.24	0.7	0.064	0.009	0.12	0.0039	2.28	0.21	0.141	0.016	0.37165	1250	180	1957	57	1196	67	847	89
FC15-005_58	153	495	294	21100	7.39	0.77	0.063	0.007	0.112	0.0021	3.481	0.1	0.226	0.006	0.76634	1220	140	1822	34	1521	24	1312	30
FC15-005_59	1320	8700	4110	1720	2.12	0.29	0.041	0.004	0.177	0.0088	0.879	0.079	0.038	0.005	0.35253	808	81	2607	84	633	41	238	30
FC15-005_59	152.6	433	317	15000	7.43	0.81	0.053	0.003	0.114	0.0021	4.1	0.13	0.262	0.008	0.82397	1036	62	1853	33	1651	26	1499	41
FC15-005_60	222	2019	755	150000	9.31	1	0.033	0.001	0.108	0.0020	1.694	0.061	0.115	0.004	0.86212	656	25	1766	35	1005	23	700	23
FC15-005_60	158.2	1174	354	240000	13.81	1.4	0.049	0.002	0.108	0.0016	2.816	0.074	0.191	0.004	0.83188	965	35	1767	27	1359	20	1125	20
FC15-005_60	143.1	1133	373	63000	13.42	1.4	0.042	0.002	0.109	0.0019	2.529	0.071	0.167	0.005	0.80047	828	40	1784	31	1280	21	997	25
FC1314_001	143.5	394	175.6	80000	8.65	0.3	0.087	0.003	0.115	0.0031	5.083	0.14	0.321	0.003	0.24528	1685	50	1878	43	1832	23	1734	16
FC1314_002	193	450	217	27000	6.36	0.2	0.036	0.002	0.126	0.0035	5.546	0.16	0.32	0.004	0.23953	1854	34	2032	43	1906	24	1783	20
FC1314_003	668	609	545	71000	4.093	0.09	0.131	0.002	0.165	0.0044	10.65	0.31	0.468	0.006	0.40162	2431	34	2502	45	2491	27	2476	28
FC1314_004	2010	1092	1680	29000	2.273	0.07	0.129	0.002	0.199	0.0053	11.57	0.34	0.425	0.008	0.44889	2444	37	2815	43	2573	30	2283	34
FC1314_005	214	525	256	41000	8.05	0.21	0.087	0.003	0.12	0.0035	5.483	0.16	0.334	0.005	0.23366	1691	50	1955	51	1897	24	1858	22
FC1314_006	293.5	668	338.8	44000	7.05	0.17	0.092	0.002	0.113	0.0032	5.062	0.15	0.324	0.004	0.31429	1785	32	1841	52	1828	25	1807	20
FC1314_007	607	750	684	51000	3.745	0.07	0.095	0.002	0.115	0.0031	5.035	0.14	0.319	0.003	0.25224	1833	30	1868	48	1824	23	1785	15
FC1314_008	408	626	560	30000	4.063	0.1	0.078	0.002	0.113	0.0033	4.29	0.14	0.276	0.005	0.45638	1508	35	1846	53	1689	27	1571	25
FC1314_009	186	1913	201	13400	15.6	1.6	0.104	0.011	0.118	0.0046	2.684	0.11	0.164	0.005	0.43588	2000	200	1936	79	1331	37	976	28
FC1314_010	153	1494	233.5	12000	22.4	2.2	0.075	0.008	0.13	0.0046	4.38	0.15	0.24	0.006	0.28703	1450	150	2035	62	1708	28	1385	29
FC1314_012	218.2	448	224	55000	6.56	0.26	0.102	0.004	0.124	0.0045	5.61	0.21	0.328	0.006	0.3089	1957	63	2014	63	1916	33	1830	29
FC1314_013	155	169.9	163	44000	3.29	0.14	0.107	0.003	0.163	0.0057	7.57	0.26	0.33	0.005	0.16755	2053	52	2484	58	2180	31	1839	23
FC1314_014	145.5	273.7	161.6	52000	6.07	0.18	0.097	0.003	0.118	0.0034	5.5	0.16	0.336	0.004	0.23059	1874	45	1920	52	1899	26	1865	20
FC1314_015	187.2	313	208.6	36000	5.2	0.13	0.097	0.003	0.118	0.0034	5.44	0.16	0.332	0.004	0.23782	1877	47	1916	51	1883	25	1843	18
FC1314_020	495	2412	2730	63000	4.96	0.32	0.021	0.002	0.112	0.0031	1.71	0.15	0.109	0.009	0.95062	422	31	1826	50	992	54	663	49
FC1314_021	335	1345	1080	1000000	6.51	0.24	0.039	0.003	0.115	0.0032	2.83	0.12	0.177	0.007	0.77057	779	55	1884	53	1359	35	1046	38
FC1314_022	41.9	1076	201	350000	62.5	5.4	0.025	0.004	0.115	0.0038	4.15	0.14	0.261	0.005	0.31424	495	83	1870	60	1664	29	1492	26
FC1314_022	33.8	354	217.5	300000	67.8	6.6	0.017	0.002	0.115	0.0041	3.837	0.13	0.243	0.003	0.0819	339	37	1879	64	1600	27	1399	18
FC1314_023	351	815	420	2300000	7.73	0.43	0.088	0.003	0.143	0.0060	6.72	0.33	0.34	0.007	0.5328	1703	48	2252	74	2073	44	1888	32
FC1314_024	293.7	2740	2230	200000	7.01	0.18	0.023	0.005	0.112	0.0033	1.67	0.26	0.107	0.017	0.98278	464	99	1833	55	941	89	644	94
FC1314_025	409	546	368	25000	5.56	0.24	0.128	0.004	0.172	0.0048	11.47	0.39	0.477	0.01	0.5704	2434	66	2571	47	2560	31	2513	44
FC1314_026	76.3	964	81.7	170000	48.1	2.5	0.102	0.008	0.155	0.0047	8.5	0.26	0.394	0.008	0.33958	1950	150	2402	52	2285	28	2142	36
FC1314_027	237	824	532	61000	6.46	0.29	0.051	0.002	0.115	0.0051	3.26	0.13	0.207	0.008	0.33486	1001	31	1867	83	1471	31	1215	41
FC1314_028	164	1522	538	900000	13.9	1	0.037	0.004	0.112	0.0034	2.71	0.11	0.171	0.007	0.71951	728	76	1830	54	1330	29	1016	38
FC1314_029	265	1673	916	17000	11.09	0.85	0.033	0.002	0.115	0.0040	3.06	0.2	0.192	0.011	0.84826	650	40	1882	61	1417	53	1134	58
FC1314_030	321	881	344	160000	7.28	0.27	0.101	0.005	0.114	0.0033	4.467	0.14	0.283	0.005	0.40196	1949	98	1856	53	1724	26	1608	24
FC1314_031	1350	2010	338	30700	2.87	0.22	0.47	0.11	0.117	0.0038	3.204	0.099	0.196	0.003	0.17931	7500	1400	1910	58	1457	24	1155	18
FC1314_032	332	901	490	50000	5.3	0.14	0.078	0.002	0.122	0.0036	3.803	0.12	0.223	0.003	0.3761	1509	35	1985	51	1592	25	1295	18
FC1314_033	434	754	574	111000	3.28	0.15	0.09	0.003	0.117	0.0040	3.77	0.19	0.226	0.007	0.74361	1745	59	1906	61	1583	41	1311	36
FC1314_033	360	392	438	12000	2.95	0.11	0.089	0.003	0.117	0.0038	4.8	0.17	0.294	0.006	0.41604	1718	55	1910	59	1783	30	1661	27
FC1314_034	231	1532	348	400000	13.94	0.73	0.074	0.003	0.15	0.0046	4.65	0.18	0.224	0.005	0.61677	1433	49	2340	52	1756	33	1304	24
FC1314_035	134	1438	230	180000	25.9	7.6	0.101	0.006	0.111	0.0031	4.313	0.13	0.279	0.005	0.39705	1940	110	1809	51	1695	24	1584	23
FC1314_036	1089	726	1396	41000	1.513	0.03	0.089	0.002	0.12	0.0036	4.508	0.13	0.268	0.005	0.24695	1729	28	1953	54	1731	24	1531	24
FC1314_037	208	1826	879	60000	11.01	0.55	0.029	0.001	0.119	0.0036	2.548	0.088	0.151	0.003	0.48759	568	28	1931	54	1285	25	906	18
FC1314_038	165.9	434	204.4	62000	7.06	0.21	0.094	0.003	0.114	0.0033	5.028	0.15	0.315	0.004	0.29824	1809	56	1865	52	1823	25	1763	21
FC1314_039	170.2	1327	552	17000	13.03	0.48	0.037	0.003	0.126	0.0037	3.437	0.099	0.196	0.004	0.28109	734	55	2041	51	1512	23	1153	19
FC1314_040	393	1278	725	45000	5.96	0.23	0.066	0.002	0.118	0.0035	3.83	0.14	0.225	0.005	0.58577	1284	36	1925	54	1598	29	1310	26

(Continued)

Table 1. LA-ICP-MS geochronology analyses (continued)

Analysis	Pb[1]	U[1]	Th[1]	206Pb	206Pb	± 2SE[2]	208Pb	± 2SE[2]	207Pb	± 2SE[2]	207Pb	± 2SE[2]	206Pb	± 2SE[2]	Rho[3]	208Pb	± 2SE[2]	207Pb	± 2SE[2]	207Pb	± 2SE[2]	206Pb	± 2SE[2]
Identifier	(ppm)	(ppm)	(ppm)	204Pb	208Pb		232Th		206Pb		235U		238U			232Th		206Pb		235U		238U	
FC1314_041	220.6	827	487	105000	6.26	0.34	0.054	0.002	0.114	0.0035	3.278	0.11	0.205	0.005	0.50055	1062	43	1866	56	1474	27	1199	29
FC1314_042	430	631	643	93600	3.43	0.14	0.088	0.002	0.115	0.0031	4.309	0.13	0.305	0.004	0.17068	1700	32	1874	49	1803	23	1716	17
FC1314_043	271.6	1436	924	130000	3.66	0.33	0.034	0.002	0.114	0.0039	3.14	0.12	0.202	0.007	0.54777	677	43	1860	62	1450	37	1188	36
FC1314_044	114.8	1880	283.2	30000	22	1.5	0.043	0.003	0.113	0.0040	2.62	0.12	0.165	0.009	0.75145	864	54	1847	63	1305	34	983	48
FC1314_045	505	454	657	62000	2.507	0.08	0.089	0.002	0.114	0.0032	5.11	0.17	0.32	0.006	0.5382	1724	38	1863	50	1835	28	1788	27
FC1314_046	497	4168	2690	4540	3.96	0.11	0.021	0.001	0.13	0.0040	1.002	0.069	0.055	0.003	0.3168	428	21	2098	53	698	34	342	16
FC1314_047	355	4170	2830	9300	5.81	0.36	0.014	4E-04	0.116	0.0033	0.892	0.044	0.055	0.002	0.83493	288.7	7.3	1894	52	645	23	344	11
FC1314_048	152	693	335	12000	7.95	0.3	0.053	0.002	0.111	0.0033	3.109	0.11	0.203	0.006	0.57835	1046	46	1813	53	1434	28	1191	30
FC1314_049	326.2	282.3	285.8	30000	3.49	0.09	0.128	0.004	0.171	0.0051	10.48	0.32	0.444	0.007	0.30785	2441	70	2565	49	2476	28	2368	32
FC1314_050	434	1067	407	260000	9.6	0.32	0.125	0.003	0.213	0.0059	13.34	0.46	0.445	0.007	0.61852	2377	50	2926	46	2702	33	2372	31
FC1314_051	224.7	1008	380.8	88000	10.41	0.47	0.065	0.002	0.118	0.0035	4.031	0.12	0.248	0.004	0.30573	1278	35	1923	53	1639	24	1427	22
FC1314_052	262	1182	416	77000	8.82	0.41	0.075	0.002	0.114	0.0034	3.628	0.12	0.225	0.006	0.50838	1457	43	1858	54	1555	27	1305	31
FC1314_053	427	1292	869	6800	5.44	0.18	0.057	0.002	0.117	0.0037	3.402	0.11	0.206	0.005	0.42737	1129	42	1911	57	1504	25	1207	28
FC1314_055	577	3140	4120	2320	3.36	0.12	0.02	0.003	0.117	0.0033	1.36	0.23	0.086	0.015	0.38701	395	63	1909	50	839	86	525	87
FC1314_056	175.4	2221	739	56000	16.32	0.53	0.026	0.001	0.115	0.0035	2.399	0.097	0.147	0.003	0.67309	513	28	1879	55	1240	29	881	18
FC1314_057	89.7	1230	107	60000	28.2	1.5	0.102	0.003	0.115	0.0037	3.78	0.15	0.233	0.008	0.6195	1950	160	1883	56	1586	32	1350	39
FC1314_058	341.5	757	413.9	80000	6.22	0.2	0.092	0.002	0.113	0.0033	4.708	0.14	0.301	0.004	0.23465	1769	35	1836	52	1767	25	1696	18
FC1314_059	281	1169	703	32000	8.96	0.34	0.047	0.003	0.122	0.0035	4.086	0.13	0.239	0.005	0.47333	920	60	1986	51	1650	26	1379	26
FC1314_060	384	2221	1341	3020	7.09	0.48	0.032	0.002	0.12	0.0036	2.128	0.094	0.127	0.004	0.74443	629	34	1952	54	1153	31	771	20
FC1314_061	626	1095	944	1140000	4.3	0.17	0.071	0.002	0.121	0.0037	4.18	0.14	0.253	0.005	0.42415	1390	40	1959	55	1669	27	1453	25
FC1314_062	145.8	294	171.5	340000	6.09	0.15	0.094	0.002	0.114	0.0034	5.11	0.15	0.324	0.005	0.227	1806	40	1854	53	1836	25	1810	24
FC1314_063	333	1599	687	1140000	12.29	0.34	0.055	0.003	0.117	0.0034	4.458	0.14	0.275	0.005	0.413	1073	53	1909	52	1722	25	1564	25
FC1314_064	346	699	386	390000	6.5	0.27	0.094	0.003	0.12	0.0042	5.44	0.17	0.329	0.004	-0.112	1806	59	1949	62	1891	27	1834	21
FC1314_065	516	666	614	390000	3.842	0.1	0.089	0.002	0.113	0.0036	4.9	0.19	0.314	0.007	0.575	1729	44	1851	57	1800	33	1758	33
FC1314_066	151	394	182	310000	7.09	0.37	0.091	0.003	0.129	0.0040	5.1	0.19	0.289	0.006	0.553	1782	74	2078	55	1834	32	1637	29
FC1314_067	342	710	396	7300000	6.09	0.13	0.094	0.002	0.113	0.0031	4.965	0.15	0.317	0.005	0.426	1806	39	1847	49	1812	25	1776	23
FC1314_068	520	1305	799	1040000	5.26	0.18	0.072	0.003	0.146	0.0040	4.594	0.14	0.227	0.003	0.440	1409	51	2295	47	1747	25	1321	18
FC1314_069	190.5	376	197	780000	16.23	0.62	0.103	0.004	0.157	0.0049	7.17	0.25	0.333	0.007	0.474	1982	78	2419	53	2131	31	1854	36
FC1314_070	484	1699	1190	12600	5.61	0.28	0.045	0.002	0.115	0.0038	2.792	0.1	0.178	0.005	0.490	892	41	1879	58	1352	28	1053	27
FC1314_071	1415	1410	2270	10000	1.678	0.09	0.069	0.003	0.118	0.0044	3.02	0.14	0.188	0.006	0.602	1343	65	1925	66	1411	34	1110	33
FC1314_072	312	1081	555	93000	5.11	0.23	0.06	0.003	0.115	0.0039	2.53	0.13	0.161	0.007	0.754	1173	51	1875	62	1277	38	963	38
FC1314_073	236.5	452	269	81000	5.35	0.22	0.095	0.002	0.114	0.0033	5.09	0.15	0.324	0.005	0.314	1833	39	1864	52	1833	25	1806	26
FC1314_074	627	3140	2720	3000	3.57	0.12	0.025	6E-04	0.131	0.0039	1.472	0.054	0.082	0.003	0.620	500	12	2103	53	917	22	507	15
FC1314_075	221.1	609	261	71000	7.33	0.33	0.088	0.003	0.115	0.0049	4.55	0.21	0.291	0.009	0.432	1703	57	1867	75	1738	38	1648	43
FC1314_076	426	801	745	134000	4.37	0.1	0.063	0.003	0.115	0.0031	4.17	0.13	0.263	0.004	0.502	1225	54	1876	49	1666	25	1507	22
FC1314_077	198.7	1230	479	32000	8.01	0.4	0.048	0.003	0.119	0.0037	2.76	0.18	0.169	0.011	0.886	945	58	1936	55	1331	49	1003	59
FC1314_078	215	747	267	106000	9.6	1.2	0.085	0.003	0.114	0.0034	4.902	0.15	0.31	0.005	0.239	1656	53	1863	53	1801	25	1741	23
FC1314_079	556	1303	452	200000	8.2	0.39	0.138	0.004	0.154	0.0054	8.58	0.31	0.402	0.009	0.361	2607	73	2389	61	2232	33	2178	42
FC1314_080	246.5	479	281.4	95000	5.24	0.15	0.093	0.002	0.116	0.0034	4.831	0.15	0.302	0.005	0.364	1803	42	1892	52	1788	26	1703	24
FC1314_081	74.5	1433	198	340000	43.3	4	0.041	0.004	0.123	0.0071	4.19	0.27	0.251	0.007	0.448	809	80	1994	100	1669	52	1446	34
FC1314_082	349	939	473	162000	6.38	0.16	0.081	0.003	0.113	0.0034	4.27	0.18	0.273	0.006	0.730	1576	57	1843	55	1684	34	1557	30
FC1314_083	532	886	700	157000	4.271	0.1	0.09	0.002	0.114	0.0033	4.94	0.16	0.315	0.004	0.445	1735	32	1854	53	1806	26	1765	20
FC1314_085	247	690	375.7	350000	6.83	0.32	0.068	0.002	0.114	0.0037	3.954	0.13	0.256	0.004	0.254	1336	39	1859	56	1624	26	1471	20
FC1314_086	427	1058	589	600000	5.16	0.29	0.081	0.005	0.12	0.0039	3.83	0.15	0.228	0.006	0.571	1576	98	1955	59	1597	32	1321	32
FC1314_087	559	959	523	7700000	5.95	0.22	0.107	0.003	0.197	0.0072	9.34	0.34	0.347	0.006	0.248	2061	62	2799	60	2370	34	1922	30
FC1314_088	236	1031	344	680000	9.9	0.34	0.093	0.003	0.12	0.0041	4.846	0.15	0.295	0.006	0.175	1790	56	1947	61	1732	25	1664	31
FC1314_089	54.4	1448	395	300000	44.4	2.8	0.016	0.002	0.11	0.0034	2.477	0.1	0.165	0.005	0.646	311	46	1738	56	1263	30	981	25
FC1314_090	476	1818	1375	440000	6.53	0.15	0.037	0.002	0.114	0.0032	2.732	0.085	0.175	0.003	0.442	731	31	1857	51	1336	23	1041	16
FC1314_091	32.4	2082	950	300000	33	4.3	0.014	0.002	0.112	0.0036	2.04	0.19	0.134	0.011	0.940	276	42	1819	58	1104	65	805	65

[1]Zircon U-Th-Pb concentrations referenced to either NIST 612 glass or 91500 zircon; concentration uncertainty approximately ±20%

[2]Isotope ratios not corrected for common Pb

[3]Dates calculated with decay constants of Jaffey et al. (1971) and $^{238}U/^{235}U$=137.818 (Hiess, 2012) using Iolite v. 3.5 (Paton et al., 2011) and U-Pb Geochron4 DRS (Paton et al., 2010)

Paton, C., Hellstrom, J., Paul, B.,Woodhead, J. and Hergt, J. 2011. "Iolite: Freeware for the visualization and processing of mass spectrometric data." Journal of Analytical Atomic Spectrometry. doi:10.1039/c1ja10172b.

Paton, C., Woodhead, J., Hellstrom, J., Hergt, J., Greig, A. & Maas, R (2010) Improved laser ablation U-Pb zircon geochronology through robust down-hole fractionation correction. G Cubed, 11, doi:10.1029/2009GC002618

Table 2. TIMS geochronology analyses

	Compositional Parameters								Radiogenic Isotope Ratios								Isotopic Ages					
Sample (# grains) (a)	U (ng) (b)	Th U (c)	Pb (pg) (b)	$^{206}Pb^*$ x10^{-13} mol (d)	mol % $^{206}Pb^*$ (d)	Pb^* Pb_c (d)	Pb_c (pg) (d)	^{206}Pb ^{204}Pb (e)	^{208}Pb ^{206}Pb (f)	^{207}Pb ^{206}Pb (f)	% err (g)	^{207}Pb ^{235}U (f)	% err (g)	^{206}Pb ^{238}U (f)	% err (g)	corr. coef.	^{207}Pb ^{206}Pb (h)	± (g)	^{207}Pb ^{235}U (h)	± (g)	^{206}Pb ^{238}U (h)	± (g)
(BB) FC15-005 Mnz 1	6.57	21.707	12941.1	79.839	97.0%	61.4	207.43	594	6.571	0.107518	0.318	4.317947	0.860	0.291269	0.726	0.933	1757.8	5.8	1696.8	7.1	1647.9	10.6
(BC) FC15-005 Mnz 2	7.88	28.265	19764.6	100.292	99.8%	1509.3	13.09	11488	8.372	0.107752	0.186	4.530881	0.947	0.304968	0.892	0.981	1761.8	3.4	1736.7	7.9	1715.9	13.4
(BI) FC15-005 Mnz 3	14.21	31.862	38883.5	174.595	99.8%	1162.5	33.42	7836	9.602	0.107715	0.191	4.372701	0.398	0.294422	0.233	0.950	1761.1	3.5	1707.2	3.3	1663.6	3.4
(BJ) FC15-005 Mnz 4	22.15	32.969	63337.1	277.794	99.3%	383.0	164.96	2538	9.837	0.107786	0.215	4.467102	0.528	0.300582	0.397	0.930	1762.3	3.9	1724.9	4.4	1694.2	5.9
(BM) FC15-005 Mnz 5	10.12	30.788	26685.5	123.040	99.4%	459.1	58.00	3192	9.308	0.107335	0.215	4.312749	0.571	0.291416	0.456	0.937	1754.7	3.9	1695.8	4.7	1648.6	6.6
(BV) FC15-005 zirc17 Pb	0.46	0.218	188.2	7.423	99.5%	60.5	3.06	3687	0.062	0.147128	0.145	7.838383	0.285	0.386393	0.172	0.916	2312.8	2.5	2212.6	2.6	2106.1	3.1
(Z30) FC15-005 zirc17 Pb	0.23	0.214	95.1	3.756	99.5%	58.9	1.59	3590	0.061	0.145596	0.170	7.754156	0.721	0.386265	0.679	0.972	2294.8	2.9	2202.9	6.5	2105.5	12.2
(Z31) FC15-005 zirc17 Pb	0.65	0.145	140.8	5.665	99.5%	65.8	2.11	4070	0.044	0.144011	0.126	4.160221	0.268	0.209517	0.156	0.962	2276.0	2.2	1666.2	2.2	1226.2	1.7
(Z31) FC15-005 zirc5 Pb	0.65	0.198	248.7	9.951	99.8%	171.7	1.44	10445	0.057	0.148334	0.107	7.527770	0.255	0.368064	0.151	0.992	2326.8	1.8	2176.3	2.3	2020.3	2.6
(Z4) FC15-005 zirc2 Pb	2.61	0.262	548.2	22.247	99.8%	123.7	4.40	7691	0.079	0.106717	0.136	3.011394	0.470	0.204659	0.415	0.961	1744.1	2.5	1410.5	3.6	1200.3	4.5
(141) FC15-005 zirc13	0.16	0.298	201.3	1.916	50.7%	0.3	152.95	38	0.088	0.136938	2.648	5.376336	2.752	0.284749	1.308	0.315	2188.8	46.1	1881.1	23.6	1615.2	18.7
(BA) FC15-005 zirc2 Pb	0.54	0.156	99.8	3.970	98.6%	20.0	4.76	1284	0.047	0.113827	0.161	2.771547	0.330	0.176594	0.202	0.928	1861.4	2.9	1347.9	2.5	1048.3	2.0
(BB) FC15-005 zirc14 Pb	0.69	0.299	189.8	7.645	99.8%	148.1	1.27	9081	0.088	0.107487	0.051	3.943334	0.245	0.266076	0.156	1.071	1757.2	0.9	1622.6	2.0	1520.9	2.1
(BJ) FC15-005 zirc15 Pb	1.15	0.319	338.0	13.494	99.7%	90.8	3.68	5569	0.094	0.107479	0.128	4.180314	0.275	0.282087	0.168	0.949	1757.1	2.3	1670.2	2.3	1601.9	2.4
(BM) FC15-005 zirc16 Pb	0.44	0.248	135.3	4.054	90.2%	2.7	36.21	189	0.074	0.111532	0.460	3.389503	0.601	0.220412	0.244	0.711	1824.5	8.3	1502.0	4.7	1284.1	2.8
(Z8) FC15-005 zirc3 Pb	1.48	0.122	404.3	16.414	99.8%	177.8	2.26	10968	0.036	0.152163	0.182	5.560893	0.747	0.265053	0.707	0.970	2370.4	3.1	1910.1	6.4	1515.6	9.5
(Z9) FC15-005 zirc4 Pb	3.98	0.325	730.0	28.908	99.5%	60.6	11.85	3732	0.099	0.105774	0.132	2.541579	0.358	0.174270	0.280	0.944	1727.8	2.4	1284.0	2.6	1035.6	2.7
(Z37) FC15-005 zirc8 Pb	4.17	0.304	941.7	37.859	99.8%	148.2	6.31	9129	0.091	0.106864	0.116	3.207896	0.912	0.217714	0.887	0.992	1746.6	2.1	1459.1	7.1	1269.8	10.2
(Z63) FC15-005 zirc11 Pb	0.75	0.314	123.3	4.898	99.5%	64.6	1.88	3953	0.096	0.105890	0.187	2.274369	0.382	0.155778	0.284	0.883	1729.8	3.4	1204.4	2.7	933.3	2.5
(Z66) FC15-005 zirc1 Pb	1.26	0.344	374.7	14.758	99.5%	63.6	5.80	3879	0.101	0.110684	0.166	4.280965	0.283	0.280515	0.150	0.884	1810.7	3.0	1689.7	2.3	1594.0	2.1
(Z73) FC15-005 zirc2 Pb	1.11	0.279	502.8	19.519	99.9%	242.5	2.07	14279	0.079	0.164746	0.133	9.584868	0.254	0.421959	0.137	0.945	2505.0	2.2	2395.7	2.3	2269.4	2.6
(Z79) FC15-005 zirc3 Pb	1.54	0.260	509.6	20.155	99.3%	44.7	11.15	2771	0.076	0.123485	0.138	5.350615	0.485	0.314259	0.429	0.962	2007.2	2.5	1877.0	4.2	1761.6	6.6
(Z86) FC15-005 zirc4 Pb	2.79	0.295	928.6	31.963	94.9%	5.6	140.10	367	0.087	0.109286	0.282	4.145106	0.407	0.275087	0.161	0.855	1787.5	5.1	1663.2	3.3	1566.6	2.2
(Z88) FC15-005 zirc5 Pb	2.67	0.330	1061.7	41.248	99.9%	336.3	3.15	19837	0.095	0.149526	0.125	7.650183	0.254	0.371067	0.142	0.957	2340.5	2.1	2190.8	2.3	2034.4	2.5
(Z89) FC15-005 zirc6 Pb	0.98	0.292	383.3	11.102	89.3%	2.5	109.07	174	0.086	0.111679	0.573	4.174731	0.713	0.271117	0.287	0.642	1826.9	10.4	1669.1	5.8	1546.5	3.9
(Z38) FC13-14 Mnz1	12.21	6.624	9754.3	150.715	99.7%	245.1	39.64	5709	2.001	0.108672	0.260	4.435615	0.573	0.296029	0.443	0.900	1777.3	4.8	1719.0	4.7	1671.6	6.5
(Z40) FC13-14 Mnz3	2.65	9.349	2655.7	32.596	99.8%	576.8	4.60	10658	2.813	0.107407	0.361	4.363167	1.221	0.294625	1.146	0.955	1755.9	6.6	1705.4	10.1	1664.6	16.8
(Z41) FC13-14 Mnz4	9.11	3.979	5626.9	119.344	99.9%	1053.9	5.33	33574	1.166	0.108632	0.201	4.705519	0.473	0.314158	0.346	0.926	1776.6	3.7	1768.2	4.0	1761.1	5.3
(Z42) FC13-14 Mnz5	44.95	4.621	29666.2	577.546	99.9%	692.7	42.77	20231	1.368	0.108604	0.165	4.612570	1.905	0.308031	1.880	0.996	1776.1	3.0	1751.5	15.9	1731.0	28.5
(Z32) FC13-14 zirc5	6.22	0.112	1925.2	80.766	99.9%	386.8	4.96	24422	0.035	0.118805	0.206	5.099234	0.435	0.311293	0.289	0.916	1938.3	3.7	1836.0	3.7	1747.1	4.4
(Z33) FC13-14 zirc6	0.22	0.224	67.5	2.724	99.5%	60.4	1.10	3760	0.069	0.112230	0.209	4.518774	0.605	0.292019	0.500	0.946	1835.8	3.8	1734.4	5.0	1651.6	7.3
(Z34) FC13-14 zirc7	0.87	0.064	245.6	10.426	99.8%	172.0	1.42	11103	0.020	0.115681	0.176	4.557930	0.375	0.285763	0.205	0.940	1890.5	3.2	1741.6	3.1	1620.3	2.9
(Z35) FC13-14 zirc8	0.53	0.262	135.4	5.367	99.4%	52.2	2.55	3188	0.088	0.112303	0.190	3.780802	1.890	0.244169	1.861	0.940	1837.0	3.4	1588.7	15.2	1408.3	23.5
(Z36) FC13-14 zirc9	1.87	0.325	566.6	22.424	99.9%	436.0	1.30	26118	0.104	0.118383	0.186	4.686842	2.385	0.287137	2.364	0.997	1932.0	3.3	1764.9	20.0	1627.2	34.0
(Z37) FC13-014 Zirc10	0.65	0.379	162.3	6.158	99.6%	79.1	2.03	4593	0.139	0.123232	0.210	3.873761	3.114	0.227986	3.096	0.940	2003.5	3.7	1608.2	25.1	1323.9	37.1

(a) Z1, Z2 ect. Are internal laboratory labels for fractions composed of single zircon grains or two-grain aliquots; all fractions annealed and chemically abraded after Mattinson (2005)

(b) U and total Pb content of zircon remnants after chemical abrasion.

(c) Model Th/U ratio calculated from radiogenic $^{208}Pb/^{206}Pb$ ratio and $^{207}Pb/^{235}U$ age.

(d) Pb* and Pbc represent radiogenic and common Pb, respectively; mol% $^{206}Pb^*$ with respect to radiogenic, blank and initial common Pb.

(e) Measured ratio corrected for spike and fractionation only.

Daily Pb analyses corrected for 0.22%/AMU mass bias based on repeat analysis of NBS-981. Faraday U analyses corrected for mass bias based on measured $^{233}U/^{235}U$ ratio.

(f) Corrected for fractionation, spike, and common Pb; up to 1 pg of common Pb was assumed to be procedural blank; $^{206}Pb/^{204}Pb = 18.66 \pm 0.60\%$; $^{207}Pb/^{204}Pb = 15.54 \pm 0.25\%$; $^{208}Pb/^{204}Pb = 37.62 \pm 0.55\%$ (all uncertainties 1-sigma). Excess over blank was assigned to initial common Pb.

(g) Errors are 2-sigma, propagated using the algorithms of Schmitz and Schoene (2007) and Crowley et al. (2007).

(h) Calculate ages are based on the decay constants of Jaffey et al. (1971).

Table 3. Whole-rock major and trace element analyses for mafic dikes

Sample	BG16-001	BG16-002	BG16-003	BG16-004	BG16-005	BG16-006	BG16-007	BG16-008	BG16-010	BG16-011	BG16-012	BG16-014
Group	A	C	A	C	C	A	A	B	B	B	A	A
Unit	Xam	Xam	Xam	Xam	Xam	Xam	Xam	Xam	Xam	Xam	Xam	Xam
SiO2	50.79	51.04	49.98	50.44	48.19	49.26	50.74	50.63	51.51	49.83	51.41	49.68
TiO2	1.052	1.365	1.178	0.943	1.802	1.505	1.059	0.844	1.131	1.022	1.377	1.282
Al2O3	13.79	14.98	13.21	13.77	14.57	13.37	12.99	15.37	14.38	17.23	13.7	13.17
FeOt	12.840146	10.176738	13.0471	12.5972	12.32726	14.324816	14.063874	9.870806	12.678182	10.239724	13.802932	14.000888
MnO	0.225	0.199	0.239	0.213	0.246	0.247	0.236	0.175	0.209	0.175	0.245	0.233
MgO	6.23	6.4	6.11	6.97	6.94	6.1	6.19	7.05	5.94	5.15	5.47	6.07
CaO	10.48	10.37	10.06	9.91	10.04	10.88	10.85	11.68	10.57	9.71	9.51	9.28
Na2O	2.21	2.7	2.15	1.97	2.34	2.14	2.02	2.2	2.19	2.3	2.41	2.73
K2O	0.63	0.82	0.43	0.77	0.71	0.18	0.22	0.67	0.54	1.46	0.47	0.82
P2O5	0.1	0.15	0.08	0.08	0.2	0.09	0.1	0.08	0.1	0.1	0.1	0.1
LOI	0.88	1.2	0.87	0.92	1.07	0.32	0.04	0.98	-0.02	1.72	0.66	1.1
Total	100.7	100.5	98.8	99.99	99.81	100	100.1	100.6	100.7	100.1	100.7	100
Sc	47	32	47	38	34	47	50	38	41	32	45	47
Be	< 1	< 1	< 1	< 1	< 1	< 1	< 1	< 1	< 1	< 1	< 1	< 1
V	336	277	336	285	350	383	408	241	280	221	367	359
Cr	80	240	80	130	240	90	100	270	70	140	50	70
Co	50	41	52	47	50	50	49	45	54	42	49	52
Ni	60	90	60	70	100	60	50	100	80	100	40	60
Cu	100	60	100	90	80	120	70	110	160	60	90	120
Zn	100	110	110	100	140	100	110	80	110	100	110	110
Ga	18	20	18	15	21	19	19	17	19	19	20	18
Ge	1.7	1.4	1.6	1.4	1.5	1.8	1.6	1.6	1.7	1.3	1.6	1.3
As	< 5	< 5	< 5	< 5	< 5	< 5	< 5	< 5	< 5	< 5	< 5	< 5
Rb	12	17	10	19	15	2	3	18	18	55	14	30
Sr	111	169	96	64	103	61	78	132	120	245	133	98
Y	25.7	33.5	27.1	20.8	38.6	30	27.1	21.9	29.2	23.1	27.7	28.6
Zr	55	104	56	52	116	63	52	70	82	74	71	63
Nb	2.6	6.3	2.6	3.2	6.6	2.3	1.9	5	5.7	5	2.8	2.3
Mo	< 2	< 2	< 2	2	< 2	< 2	< 2	< 2	< 2	< 2	< 2	< 2
Ag	< 0.5	< 0.5	< 0.5	< 0.5	< 0.5	< 0.5	< 0.5	< 0.5	< 0.5	< 0.5	< 0.5	< 0.5
In	0.1	0.1	0.1	< 0.1	0.1	0.1	0.1	< 0.1	0.1	0.1	0.1	0.1
Sn	1	1	1	1	1	1	1	1	1	1	1	1
Sb	< 0.2	< 0.2	< 0.2	< 0.2	< 0.2	< 0.2	< 0.2	< 0.2	0.2	< 0.2	< 0.2	< 0.2
Cs	0.2	0.3	0.1	0.3	0.4	0.3	0.2	0.5	0.9	0.5	0.2	0.3
Ba	133	90	97	91	81	105	59	218	159	208	225	151
La	5.4	10.4	4.8	4.4	11.5	5.1	5.6	10.1	11.1	10.8	7.62	5.53
Ce	12.5	24.4	11.8	10.2	27.4	14.1	13.6	21.5	23	21.6	17.1	13.2
Pr	1.74	3.2	1.68	1.51	3.92	2.13	2	2.56	2.82	2.73	2.31	1.88
Nd	8.41	15.6	8.43	7.59	17.9	11.5	8.88	11.1	12.5	11.8	10.8	9.4
Sm	2.85	4.27	2.69	2.36	4.73	3.54	3.12	2.89	3.71	3.18	3.26	3.13
Eu	0.989	1.26	0.832	0.743	1.6	1.23	0.955	0.868	1.14	1.1	1.24	1.25
Gd	3.81	5.3	3.75	2.88	5.72	4.23	3.54	3.4	4.37	3.57	4.22	4.18
Tb	0.7	0.9	0.67	0.54	1	0.78	0.67	0.57	0.77	0.6	0.77	0.79
Dy	4.3	5.49	4.42	3.71	6.3	5.1	4.38	3.59	4.73	3.7	5.01	5.01
Ho	0.9	1.14	0.93	0.73	1.33	1.04	0.92	0.73	0.97	0.77	0.99	0.98
Er	2.59	3.34	2.85	2.13	3.95	3.07	2.81	2.09	2.81	2.29	2.82	2.96
Tm	0.372	0.491	0.394	0.313	0.58	0.453	0.407	0.299	0.433	0.335	0.421	0.445
Yb	2.47	3.27	2.52	2.09	3.7	2.97	2.7	1.97	2.83	2.26	2.72	2.87
Lu	0.388	0.496	0.407	0.331	0.573	0.45	0.419	0.313	0.451	0.357	0.432	0.421
Hf	1.6	3.2	1.8	1.6	3.6	2	1.8	1.9	2.5	2.1	2.3	1.9
Ta	0.13	0.47	0.14	0.31	0.36	0.15	0.16	0.39	0.35	0.32	0.16	0.16
W	0.8	< 0.5	< 0.5	1	< 0.5	< 0.5	< 0.5	0.5	0.8	0.6	< 0.5	< 0.5
Tl	0.11	0.09	< 0.05	0.09	0.11	< 0.05	< 0.05	0.06	0.05	0.19	0.08	0.18
Pb	< 5	< 5	< 5	< 5	< 5	< 5	< 5	< 5	< 5	5	< 5	< 5
Bi	0.2	0.1	< 0.1	0.1	< 0.1	< 0.1	< 0.1	0.1	< 0.1	< 0.1	< 0.1	< 0.1
Th	0.93	1.53	0.86	0.48	1.21	0.46	1.19	2.19	2.39	2.03	1.97	1
U	0.25	0.77	0.22	0.37	0.31	0.17	0.2	0.88	0.7	0.66	0.46	0.38

(continued)

Table 3. Whole-rock major and trace element analyses for mafic dikes (continued)

Sample	BG17-003	BG17-010	BG17-011	BG17-012	BG17-013	BG17-014	BG17-016	BG17-017	BG17-020	BG17-021	BG17-022
Group	A	D	A	D	A	D	B	B	A	A	A
Unit	Xam	Yd	Xam	Yd	Xam	Yd	Xam	Xam	Xam	Xam	Xam
SiO2	49.67	49.8	49.66	49.95	51.06	49.83	50.78	51.55	50.79	50.59	50.67
TiO2	1.351	1.049	1.015	1.239	1.365	1.21	1.109	0.996	1.02	0.839	0.952
Al2O3	13.28	14.57	13.95	13.85	13.13	13.99	13.97	14.12	13.68	13.84	13.67
FeOt	13.514996	10.239724	12.588202	11.60742	14.48678	11.544434	12.624194	12.19229	13.36203	12.498222	13.18207
MnO	0.237	0.184	0.217	0.199	0.229	0.198	0.21	0.204	0.223	0.219	0.228
MgO	6.07	7.47	6.58	7.18	5.48	7.11	6.29	6.32	6.12	6.98	5.99
CaO	11.54	12.39	11.09	11.49	9.51	11.66	10.28	10.64	10.55	11.06	10.3
Na2O	2.19	2.08	2.09	2.24	2.26	2.08	2.08	2.08	2.14	1.93	2.21
K2O	0.21	0.15	0.28	0.28	0.31	0.22	0.55	0.58	0.3	0.25	0.42
P2O5	0.13	0.09	0.06	0.11	0.11	0.09	0.1	0.1	0.08	0.07	0.09
LOI	0.42	1.23	1.56	1.18	1.02	1.18	0.68	0.53	0.52	0.55	0.82
Total	100.1	100.4	100.5	100.6	100.6	100.4	100.1	100.7	100.3	100.2	100
Sc	47	46	44	45	47	45	40	41	47	47	45
Be	< 1	< 1	< 1	< 1	< 1	< 1	< 1	< 1	< 1	< 1	< 1
V	306	283	305	310	373	311	280	272	318	296	319
Cr	90	220	60	200	70	190	110	120	60	80	60
Co	48	45	51	46	50	49	51	53	57	54	51
Ni	70	90	50	90	60	80	90	90	70	70	60
Cu	130	190	120	120	100	130	120	120	140	130	130
Zn	110	70	90	100	100	90	100	110	110	90	110
Ga	20	17	18	18	20	17	18	18	19	17	18
Ge	1.7	1.5	1.4	1.9	1.8	2	1.3	1.5	1.6	1.6	1.7
As	< 5	< 5	< 5	< 5	< 5	< 5	< 5	< 5	< 5	< 5	< 5
Rb	3	2	8	3	6	2	17	24	7	8	10
Sr	94	135	156	137	65	137	125	148	110	92	84
Y	32	21.1	20.5	23.3	29.8	22.6	27.4	26	25.4	20.7	24.2
Zr	75	52	49	63	66	61	80	75	52	41	47
Nb	2.5	4.1	1.4	5	2.8	4.7	5.4	4.7	1.2	0.8	1.2
Mo	< 2	< 2	< 2	< 2	< 2	< 2	< 2	< 2	< 2	< 2	< 2
Ag	< 0.5	< 0.5	< 0.5	< 0.5	< 0.5	< 0.5	< 0.5	< 0.5	< 0.5	< 0.5	< 0.5
In	0.1	0.1	0.1	0.1	0.1	0.1	0.1	0.1	0.1	0.1	0.1
Sn	1	1	< 1	1	1	1	1	1	< 1	< 1	1
Sb	< 0.2	< 0.2	< 0.2	< 0.2	< 0.2	< 0.2	< 0.2	0.2	< 0.2	< 0.2	< 0.2
Cs	0.1	0.1	0.2	0.2	0.1	0.1	0.7	1.6	0.2	0.5	0.1
Ba	49	50	613	122	47	70	286	262	134	114	128
La	5.17	5.75	5.27	6.82	4.8	6.32	10.9	10.3	5.11	3.55	3.39
Ce	13.7	13.5	11.7	16.3	11	15.5	23.3	21.1	11.5	8.1	8.31
Pr	2.08	1.93	1.56	2.13	1.54	2.14	2.92	2.63	1.48	1.12	1.27
Nd	10.6	8.58	7.88	10.9	7.53	9.44	13.1	11.6	7.42	5.4	5.7
Sm	3.62	2.54	2.26	2.84	3.04	2.78	3.14	3.36	2.75	2.13	1.96
Eu	1.52	0.875	0.9	1.14	0.988	1.07	1	1.04	1.02	0.769	0.858
Gd	4.96	3.48	3.22	3.55	3.98	3.6	4.1	3.59	3.61	3.06	3.18
Tb	0.91	0.58	0.56	0.61	0.76	0.63	0.72	0.68	0.64	0.55	0.6
Dy	5.47	3.65	3.45	3.9	5.04	4.04	4.61	4.4	4.19	3.43	3.93
Ho	1.11	0.74	0.71	0.81	1.05	0.83	0.95	0.92	0.83	0.74	0.85
Er	3.5	2.18	2.08	2.4	3.13	2.33	2.79	2.7	2.37	2.36	2.38
Tm	0.525	0.312	0.308	0.337	0.47	0.35	0.415	0.398	0.361	0.323	0.351
Yb	3.39	2.08	1.98	2.19	3.05	2.27	2.77	2.6	2.48	2.28	2.4
Lu	0.505	0.299	0.306	0.323	0.459	0.33	0.438	0.403	0.397	0.335	0.365
Hf	2.3	1.6	1.5	2	2.1	2	2.6	2.2	1.6	1.2	1.4
Ta	0.18	0.25	0.09	0.34	0.2	0.32	0.35	0.32	0.09	0.08	0.1
W	< 0.5	< 0.5	< 0.5	< 0.5	< 0.5	< 0.5	0.5	< 0.5	< 0.5	< 0.5	0.5
Tl	< 0.05	< 0.05	< 0.05	< 0.05	< 0.05	< 0.05	0.05	0.17	< 0.05	< 0.05	< 0.05
Pb	< 5	< 5	< 5	< 5	< 5	< 5	< 5	< 5	< 5	< 5	< 5
Bi	< 0.1	< 0.1	< 0.1	< 0.1	< 0.1	< 0.1	< 0.1	< 0.1	< 0.1	< 0.1	< 0.1
Th	0.68	0.74	1.1	0.91	1.05	0.84	2.72	2.13	0.97	0.61	1.01
U	0.22	0.23	0.2	0.3	0.42	0.32	0.77	0.6	0.21	0.16	0.48

(continued)

Table 3. Whole-rock major and trace element analyses for mafic dikes (continued)

Sample	BG17-023	BG17-024	BG17-025	BG17-026	BG17-029	BG17-033	BG17-034	BG17-035	BG17-037	BVM18-012	BCR-2
Group	A	A	A	B	C	B	D	A	C	C	
Unit	Xam	Xam	Xam	Xam	Xam	Xam	Yd	Xam	Xam	Xam	
SiO2	49.81	50.65	51.59	50.95	49.75	50.56	50.06	51.23	49.86	49.91	54.44
TiO2	0.784	1.092	1.308	0.837	0.693	0.855	1.99	1.416	2.135	1.159	2.282
Al2O3	13.6	13.57	13.57	14.45	16.08	14.62	13.37	13.46	13.73	14.39	13.23
FeOt	11.706398	13.40702	13.99189	10.266718	9.510886	10.185736	13.173072	14.48678	11.085536	11.004554	12.19229
MnO	0.217	0.229	0.232	0.188	0.217	0.181	0.228	0.254	0.229	0.189	0.195
MgO	7.01	5.91	5.46	6.77	7.78	6.68	5.99	5.05	7.01	7.3	3.5
CaO	10.97	10.13	9.9	11.33	10.47	11.07	10.45	8.98	7.68	12.11	7.18
Na2O	2	2.05	2.11	2.07	2.41	1.91	2.25	2.22	2.36	2.04	3.17
K2O	0.38	0.34	0.38	0.58	1.13	0.76	0.32	0.43	1.84	0.2	1.79
P2O5	0.06	0.11	0.1	0.09	0.05	0.11	0.2	0.1	0.21	0.08	0.35
LOI	1.19	1.08	0.36	0.85	1.47	1.09	0.83	0.91	2.73	0.53	0.02
Total	99.02	100.1	100.6	99.54	100.6	99.16	100.3	100.2	100.1	100.2	99.71
Sc	46	45	46	37	40	37	44	43	45	45	32
Be	< 1	< 1	< 1	< 1	3	< 1	< 1	< 1	2	< 1	2
V	285	333	359	236	232	233	390	363	410	309	410
Cr	90	90	80	240	230	250	120	40	110	200	< 20
Co	51	51	47	46	35	44	47	50	48	52	37
Ni	70	60	60	90	90	100	80	40	80	90	40
Cu	50	120	100	80	40	100	160	110	110	160	20
Zn	90	120	110	90	90	90	130	120	90	90	130
Ga	16	18	19	17	19	17	20	21	19	17	23
Ge	1.7	1.3	1.3	1.7	1.9	1.2	1.9	1.8	1.5	1.7	1.6
As	< 5	< 5	< 5	< 5	< 5	< 5	< 5	< 5	< 5	< 5	< 5
Rb	14	6	10	12	29	22	8	9	35	6	47
Sr	108	75	85	129	143	128	178	118	199	140	335
Y	18.7	24.7	29.7	22.3	13.6	23	31.8	29.6	32.8	20.9	35.1
Zr	40	53	69	72	36	74	113	77	117	53	158
Nb	1	1.4	2.3	4.8	2.7	5.2	12.6	2.8	13.3	4	11.4
Mo	< 2	< 2	< 2	< 2	< 2	< 2	< 2	< 2	< 2	< 2	> 100
Ag	< 0.5	< 0.5	< 0.5	< 0.5	< 0.5	< 0.5	< 0.5	< 0.5	< 0.5	< 0.5	< 0.5
In	0.1	0.1	0.1	< 0.1	0.1	0.1	0.1	0.1	0.1	< 0.1	0.1
Sn	< 1	1	1	1	2	1	1	1	1	1	2
Sb	< 0.2	< 0.2	< 0.2	< 0.2	< 0.2	< 0.2	< 0.2	< 0.2	< 0.2	< 0.2	0.4
Cs	0.9	0.2	0.2	0.3	0.3	0.4	0.2	0.1	0.6	0.2	1.1
Ba	91	69	100	188	116	173	98	98	247	70	692
La	2.74	4.8	6.11	10.3	4.93	11.3	12.7	6.79	14.1	5.51	25.2
Ce	6.77	11.8	14.5	21.5	10.9	23	30.3	14.9	32.8	13.6	52.7
Pr	1.05	1.6	1.98	2.62	1.52	2.79	4	2.11	4.38	1.87	6.72
Nd	5.05	8.92	9.54	10.7	6.79	12.1	19.4	11.2	20.3	8.98	27.3
Sm	2.03	2.45	3.19	2.92	1.8	2.74	5.15	2.86	5.48	2.59	7.07
Eu	0.644	1.09	1.05	0.923	0.646	1.04	1.69	1.26	1.82	0.931	1.97
Gd	2.51	3.55	4.07	3.3	2.61	3.27	5.79	4.38	5.82	3.16	6.29
Tb	0.46	0.66	0.75	0.57	0.41	0.59	0.93	0.76	0.95	0.57	1.03
Dy	3.07	4.36	4.87	3.69	2.46	3.74	5.82	4.95	6.11	3.81	6.42
Ho	0.62	0.86	0.99	0.76	0.48	0.8	1.16	1.05	1.13	0.77	1.22
Er	1.75	2.49	2.91	2.25	1.32	2.32	3.21	3.04	3.31	2.01	3.46
Tm	0.26	0.379	0.429	0.331	0.186	0.338	0.474	0.441	0.464	0.302	0.506
Yb	1.76	2.58	3.06	2.15	1.19	2.17	3.16	2.72	3.15	2.1	3.19
Lu	0.275	0.379	0.473	0.334	0.182	0.341	0.466	0.429	0.465	0.332	0.459
Hf	1.1	1.5	2.4	2.1	1.1	2.1	3.6	2.2	3.5	1.6	4.6
Ta	0.07	0.09	0.19	0.37	0.33	0.35	0.84	0.2	0.89	0.29	0.75
W	< 0.5	0.5	< 0.5	0.6	0.6	< 0.5	0.7	< 0.5	< 0.5	< 0.5	0.5
Tl	0.05	< 0.05	< 0.05	< 0.05	0.13	0.11	< 0.05	< 0.05	0.09	< 0.05	0.17
Pb	< 5	< 5	< 5	< 5	< 5	< 5	< 5	< 5	< 5	< 5	< 5
Bi	< 0.1	0.1	< 0.1	0.1	0.4	< 0.1	0.1	< 0.1	< 0.1	< 0.1	< 0.1
Th	0.4	0.91	1.38	2.07	0.56	2.35	1.58	1.77	1.62	0.77	5.94
U	0.11	0.35	0.46	0.63	0.81	0.71	0.44	0.45	0.42	0.19	1.77